

UNCLASSIFIED

SECURITY CLASSIFICATION OF THIS PAGE

REPORT DOCUMENTATION PAGE

Form Approved
OMB No. 0704-0188

1a. REPORT SECURITY CLASSIFICATION UNCLASSIFIED			1b. RESTRICTIVE MARKINGS		
2a. SECURITY CLASSIFICATION AUTHORITY			3. DISTRIBUTION/AVAILABILITY OF REPORT		
2b. DECLASSIFICATION/DOWNGRADING SCHEDULE			Unlimited		
4. PERFORMING ORGANIZATION REPORT NUMBER(S) FJSRL-TR-89-0008			5. MONITORING ORGANIZATION REPORT NUMBER(S)		
6a. NAME OF PERFORMING ORGANIZATION Frank J. Seiler Research Lab		6b. OFFICE SYMBOL (if applicable) FJSRL/NH	7a. NAME OF MONITORING ORGANIZATION		
6c. ADDRESS (City, State, and ZIP Code) USAF Academy CO 80840-6528			7b. ADDRESS (City, State, and ZIP Code)		
8a. NAME OF FUNDING/SPONSORING ORGANIZATION AFIT/FJSRL		8b. OFFICE SYMBOL (if applicable)	9. PROCUREMENT INSTRUMENT IDENTIFICATION NUMBER		
8c. ADDRESS (City, State, and ZIP Code) AFIT Wright-Patterson AFB OH 45433			10. SOURCE OF FUNDING NUMBERS		
PROGRAM ELEMENT NO. 61102F	PROJECT NO. 2301	TASK NO. F1	WORK UNIT ACCESSION NO. 74		
11. TITLE (Include Security Classification) Magnetically Insulated Electron Flows in Pulsed Power Systems (U)					
12. PERSONAL AUTHOR(S) Robert I. Lawconnell					
13a. TYPE OF REPORT Final		13b. TIME COVERED FROM Jan 87 TO Jan 88		14. DATE OF REPORT (Year, Month, Day) Aug 89	
15. PAGE COUNT 175					
16. SUPPLEMENTARY NOTATION May 1988 PhD Dissertation from University of New Mexico					
17. COSATI CODES			18. SUBJECT TERMS (Continue on reverse if necessary and identify by block number)		
FIELD	GROUP	SUB-GROUP	Magnetic insulation, Pulsed power, Plasma erosion		
20	09		Opening switch, Transmission line, Insulation threshold		
09	01				
19. ABSTRACT (Continue on reverse if necessary and identify by block number)					
<p>Magnetic insulation is crucial in the operation of large pulsed power systems. This phenomena is explored in the following work. Particular attention is paid to describing magnetic insulation in realistic pulsed power systems. A theoretical model is developed that allows one to produce self consistent magnetically insulated laminar flows in perturbed cylindrical systems given only the electron density profile. The theory is checked and justified by detailed comparisons with results from a 2-dimensional electromagnetic code -- MASK.</p> <p>The procedure followed in the theoretical development is to use the relativistic Vlasov equation, Ampere's law and Gauss' law, to obtain a relation between the density profile and the velocity profile for insulated flows. Given the density profile and the corresponding derived velocity profile, a self consistent flow solution is obtained by means of Maxwell's equations. It is checked by taking a special case - corresponding to no perturbations - which</p> <p>(CONTINUED ON REVERSE)</p>					
20. DISTRIBUTION/AVAILABILITY OF ABSTRACT <input type="checkbox"/> UNCLASSIFIED/UNLIMITED <input checked="" type="checkbox"/> SAME AS RPT. <input type="checkbox"/> DTIC USERS			21. ABSTRACT SECURITY CLASSIFICATION UNCLASSIFIED		
22a. NAME OF RESPONSIBLE INDIVIDUAL Captain R.I. Lawconnell			22b. TELEPHONE (Include Area Code) (719) 472-3502		22c. OFFICE SYMBOL FJSRL/NH

UNCLASSIFIED

BLOCK 19 (ABSTRACT) CONTINUED:

results in the well known Brillouin flow theory. -

In addition, a detailed numerical study is undertaken in which the magnetic insulation threshold for various pulsed power systems is determined. Particular emphasis is placed on determining the magnetic insulation threshold of a pulsed power system employing a plasma erosion opening switch.

The procedure employed in the computational study is to vary critical aspects of the pulsed power system and then note whether magnetic insulation breaks down. The point at which magnetic insulation breaks down - as a function of geometry, load impedance, and applied voltage - is the magnetic insulation threshold for the system. The computational technique used is a 2-dimensional electromagnetic particle in cell code. The results of the study are consistent with basic magnetic insulation theories in the limited regimes in which they apply.

Results from the work include magnetic insulation threshold graphs for a variety of systems. These graphs give clear new insights into the relationships between the applied voltages, perturbation and load impedances, and magnetic insulation. In addition, the new magnetic insulation theory allows one to theoretically predict flow solutions downstream of a perturbation. Additional research opportunities are suggested in the conclusions.

UNCLASSIFIED

MAGNETICALLY INSULATED ELECTRON FLOWS IN PULSED
POWER SYSTEMS

by

ROBERT IVEY LAWCONNELL

Accession For	
NTIS GRA&I	<input checked="" type="checkbox"/>
DTIC TAB	<input type="checkbox"/>
Unannounced	<input type="checkbox"/>
Justification	
By	
Distribution/	
Availability Codes	
Dist	Avail and/or Special
A-1	

DISSERTATION

Submitted in Partial Fulfillment of the
Requirements for the Degree of
Doctor of Philosophy in Physics

The University of New Mexico
Albuquerque, New Mexico



✓

VI Blank

ACKNOWLEDGEMENTS

First and foremost, I would like to acknowledge the support of the Air Force Institute of Technology which kept bread on the table while I pursued this work. In addition, I would like to thank the personnel at the Naval Research Laboratory for their friendship, expert guidance, and support. I would specifically like to thank Dr. Paul Ottinger for suggesting this line of work and for his help in completing it. I would also like to thank Dr. Jesse Neri for his encouragement, guidance, and friendship. Finally, I would like to thank the chairman of my committee, Dr. Jack K. McIver, who kept up with my research even though I was half way across the country. Additional thanks go to Jack for his guidance, encouragement, and faith in me.

MAGNETICALLY INSULATED ELECTRON FLOWS IN PULSED POWER SYSTEMS

Robert Ivey Lawconnell

B. S. Physics, Brigham Young University, 1980

M. S. Physics, University of New Mexico, 1984

Ph. D. Physics, University of New Mexico, 1988

Magnetic insulation is crucial in the operation of large pulsed power systems. This phenomena is explored in the following work. Particular attention is paid to describing magnetic insulation in realistic pulsed power systems. A theoretical model is developed that allows one to produce self consistent magnetically insulated laminar flows in perturbed cylindrical systems given only the electron density profile. The theory is checked and justified by detailed comparisons with results from a 2-dimensional electromagnetic code — MASK.

The procedure followed in the theoretical development is to use the relativistic Vlasov equation, Ampere's law and Gauss' law, to obtain a relation between the density profile and the velocity profile for insulated flows. Given the density profile and the corresponding derived velocity profile, a self consistent flow solution is obtained by means of Maxwell's equations. It is checked by taking a

special case — corresponding to no perturbations — which results in the well known Brillouin flow theory.

In addition, a detailed numerical study is undertaken in which the magnetic insulation threshold for various pulsed power systems is determined. Particular emphasis is placed on determining the magnetic insulation threshold of a pulsed power system employing a plasma erosion opening switch.

The procedure employed in the computational study is to vary critical aspects of the pulsed power system and then note whether magnetic insulation breaks down. The point at which magnetic insulation breaks down — as a function of geometry, load impedance, and applied voltage — is the magnetic insulation threshold for the system. The computational technique used is a 2-dimensional electromagnetic particle in cell code. The results of the study are consistent with basic magnetic insulation theories in the limited regimes in which they apply.

Results from the work include magnetic insulation threshold graphs for a variety of systems. These graphs give clear new insights into the relationships between the applied voltages, perturbation and load impedances, and magnetic insulation. In addition, the new magnetic insulation theory allows one to theoretically predict flow solutions downstream of a perturbation. Additional research opportunities are suggested in the conclusions.

TABLE OF CONTENTS

CHAPTER	PAGE
1. INTRODUCTION.....	1
1.1 Concepts of Magnetic Insulation.....	1
1.2 Historical Summary and Background.....	6
1.3 Outline and Accomplishments.....	10
1.4 Basic Physics.....	11
1.5 Computational Tools.....	13
2. BASICS OF CYLINDRICAL MAGNETICALLY INSULATED TRANSMISSION LINE THEORY.....	21
2.1 Extend Cartesian Theory to Cylindrical Coordinates.....	21
2.2 Pressure Balance Check.....	26
2.3 Laminar Nature of Electron Flows.....	28
2.4 Brillouin Flow Theory Derivation.....	33
3. GENERAL THEORY OF LAMINAR FLOWS.....	38
3.1 Relation Between the Density and Velocity Profiles.....	39
3.2 Laminar Flow Equations.....	41
3.3 Two Derivations.....	43
3.3.1 Brillouin Flow.....	44
3.3.2 Constant Density Flow.....	55
3.4 Comparison of Constant Density and Brillouin Theory Predictions to MASK Simulations....	59
4. PLASMA EROSION OPENING SWITCH.....	65
4.1 Historical Summary and Background Physics..	67

CHAPTER	PAGE
4.2 Magnetic Insulation Phase Electron Flow....	72
4.2.1 Beam Launching.....	75
4.2.2 Laminar Flows.....	86
4.2.3 Non-Laminar Flows.....	96
5. MAGNETIC INSULATION THRESHOLDS.....	102
5.1 Slightly Perturbed Flow.....	105
5.2 Disrupted Flows.....	110
5.3 Fits to Magnetic Insulation Data.....	111
5.4 Model Gamble II Experiment.....	118
6. CONCLUSIONS.....	122
APPENDICIES	
APPENDIX A: ALTERNATIVE CYLINDRICAL TRANSMISSION	
LINE THEORY DERIVATION.....	125
APPENDIX B: RELATION BETWEEN THE DENSITY AND	
VELOCITY PROFILES.....	128
APPENDIX C: MAGNETIC INSULATION THRESHOLD DATA.....	135
REFERENCES.....	145

LIST OF ILLUSTRATIONS

FIGURE		PAGE
1	Electron Orbits in Magnetically Insulated Flow	2
2	Types of Magnetically Insulated Flows.....	4
3	MASK Meshes.....	17
4	Transmission Line Elements.....	20
5	MITL for Maxwell-Stress-Tensor Analysis.....	27
6	MASK Semi-Laminar Flows.....	32
7	Density Profiles for the Constant Density and Brillouin Flow Solutions.....	50
8	Potential Profiles for the Constant Density and Brillouin Flow Solutions.....	51
9	Field Profiles for the Constant Density and Brillouin Flow Solutions.....	52
10	Azial Velocity and Laminar Flow Check for the Constant Density and Brillouin Flow Solutions...	53
11	Laminar Flow Check and Total Energy vs Canonical Momentum Profiles.....	54
12	Theory vs MASK Simulations for the Case of Insignificant Space Charge Flow.....	60
13	Theory vs MASK Simulations for the Case of a Fairly Significant Space Charge Flow.....	62
14	Theory vs MASK Simulations for the Case of a Large Space Charge Flow.....	63
15	The Four Phases of a PEOS Opening..	66
16	Insulation Wave in a Load-Limited Line.....	74

FIGURE	PAGE
17	Example of Beam Launching.....76
18	Geometry for Theoretical Analysis of Beam Launching.....78
19	Magnetic Field within the Launched Beam.....82
20	Electric Field (\hat{r}) within the Launched Beam.....83
21	Electric Field (\hat{z}) within the Launched Beam.....84
22	Charge Density and Electron Orbits for a Launched Beam.....85
23	Laminar Electron Orbits for a Launched Beam.....87
24	Electric Field (\hat{r}) Histogram for a Laminar Flow.....89
25	Magnetic Field ($\hat{\theta}$) Histogram for a Laminar Flow.....90
26	Momentum (\hat{z}) Particle Plot for a Laminar Flow....91
27	Non-Laminar Electron Orbits for a Launched Beam.....97
28	Electric Field (\hat{r}) Histogram for a Non-Laminar Flow.....98
29	Magnetic Field ($\hat{\theta}$) Histogram for a Non-Laminar Flow.....99
30	Momentum (\hat{z}) Particle Plot for a Non-Laminar Flow.....100
31	Charge Density and Electron Orbits for a Launched Tightly Trapped Beam.....101
32	Current Loss Due to Magnetic Insulation

FIGURE	PAGE
	Deterioration.....103
33	Magnetic Insulation Threshold for Brillouin Flows.....104
34	Normalized Load Impedance vs Diode Gap Spacing..107
35	Magnetic Insulation Threshold Data for Systems Without Perturbing Structures.....109
36	Normalized Load Impedance vs Diode Gap Spacing with a Perturbing Structure.....112
37	Magnetic Insulation Threshold Data for Systems with Perturbing Structures.....113
38	Fit to Data Corresponding to Figure 35.....115
39	Fit of Computational Data (PEOS, Figure 37) Compared to NRL's Previous Estimate (CRIT) of the Magnetic Insulation Threshold.....116
40	Comparison of This Works (ICNEW) and NRL's Estimate (ICOLD) of the Critical Current Required for Magnetic Insulation.....117
41	Experimental Setup for PEOS Shot 3426.....119
42	Comparison of Theory to Experiment for Shot 3426.....121

LIST OF TABLES

TABLE		PAGE
1	Comparison of Anode Electric Fields from MASK and the Laminar Theory.....	30
B1	Verification of Equation (B26).....	134
C1	Simulation Data for the Determination of the Magnetic Insulation Threshold ($r_a=.05$, $r_c=.025$).....	136
C2	Simulation Data for the Determination of the Magnetic Insulation Threshold ($r_a=.05$, $r_c=.005$).....	137
C3	Simulation Data for the Determination of the Magnetic Insulation Threshold ($r_a=.035$, $r_c=.025$).....	138
C4	Simulation Data for the Determination of the Magnetic Insulation Threshold for Systems with a Non-Ion Emitting Structure ($r_c=.025$, $r_a=.05$, $r_p=.035$, $D=.192$, $D_p=.06$, $\Delta z=.03$).....	139
C5	Simulation Data for the Determination of the Magnetic Insulation Threshold for Systems with a Non-Ion Emitting Structure ($r_c=.025$, $r_a=.05$, $r_p=.035$, $D_p=.105$, $D=.192$, $\Delta z=.03$).....	140
C6	Simulation Data for the Determination of the Magnetic Insulation Threshold for Systems with a Non-Ion Emitting Structure ($r_c=.025$, $r_a=.05$)..	141

TABLE	PAGE
C7	Magnetic Insulation Threshold Data for an Ion Emitting PEOS Like Structure ($r_c=.025$, $r_a=.05$, $r_p=.035$, $D_p=.06$, $D=.192$, $\Delta z=.03$).....142
C8	Magnetic Insulation Threshold Data for an Ion Emitting PEOS Like Structure ($r_c=.025$, $r_a=.05$, $r_p=.035$, $D_p=.09$, $D=.192$, $\Delta z=.03$).....142
C9	Magnetic Insulation Threshold Data for an Ion Emitting PEOS Like Structure ($r_c=.025$, $r_a=.05$, $r_p=.04$, $D_p=.09$, $D=.192$, $\Delta z=.03$).....143

CHAPTER 1

INTRODUCTION

1.1 Concepts of Magnetic Insulation

Magnetic insulation is crucial in the operation of large pulsed power systems. This applies especially to systems with electric fields greater than approximately 20 to 50 MV/m [1]; because, explosive electron emission occurs from surfaces subjected to such fields. These electrons will short out the system at a rate consistent with the speed of light without magnetic insulation. Therefore, insuring magnetic insulation in large pulsed power systems is a necessity of those in the field and a topic of this work.

The essence of magnetic insulation is to externally apply or self-consistently generate magnetic fields that act perpendicular to the electric fields found in the system in order to confine the electrons. An example of magnetic insulation for a self-consistently generated magnetic field in a coaxial geometry is shown in figure 1. The current flowing in the system (I_a , I_e , I_c) generates a $-B_\theta$ field. The electric field is in the minus \hat{r} direction. As a result, the electrons explosively emitted from the cathode are pulled by the imposed electric field towards the anode. However, the magnetic field redirects the electrons back towards the cathode by means of $\vec{v} \times \vec{B}$ forces. Therefore, the electrons $\vec{E} \times \vec{B}$ drift in the $+\hat{z}$ direction while being

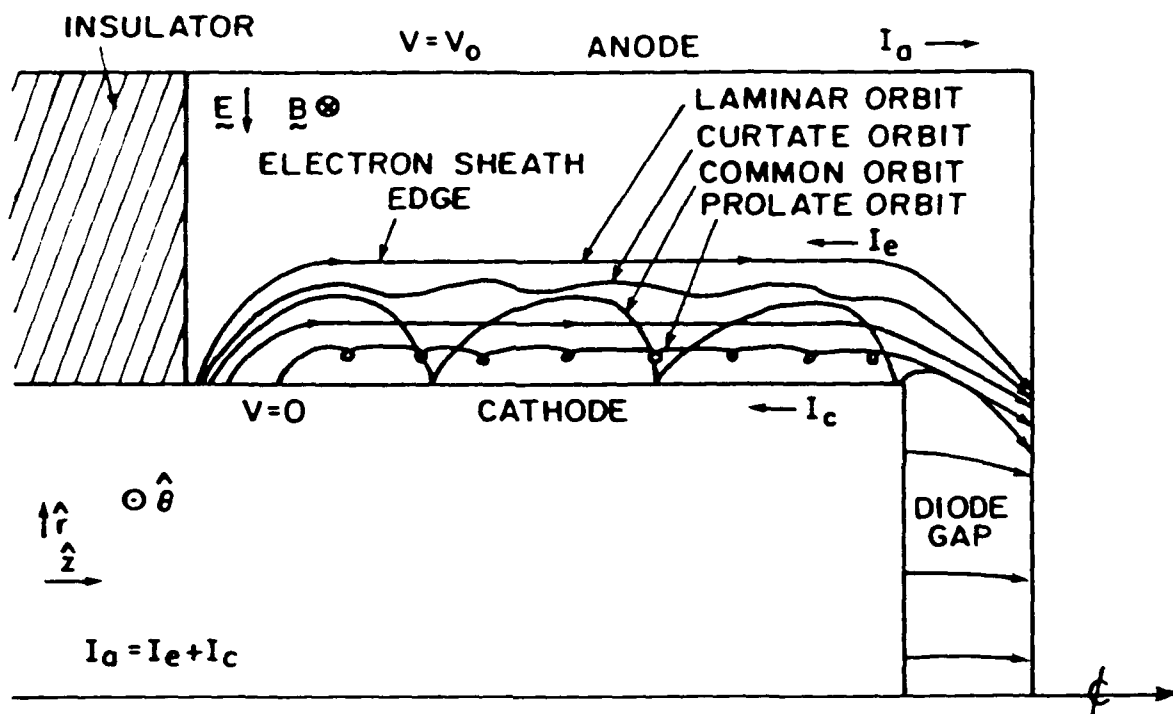


Figure 1. Electron Orbits in Magnetically Insulated Flow.

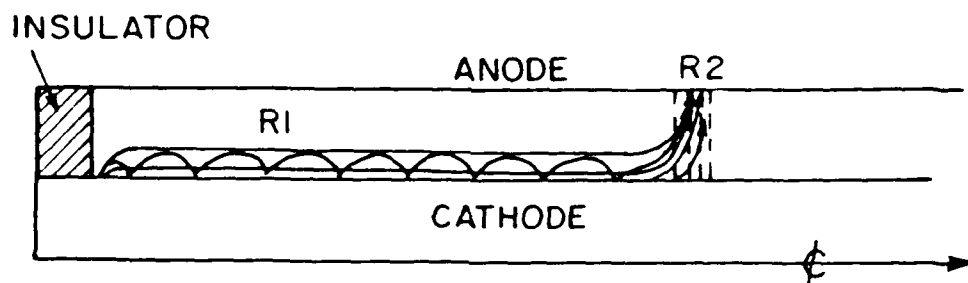
The primary electron orbits are shown along with the directions of the anode (I_a), cathode (I_c) and space charge (I_e) currents in a cylindrical geometry.

magnetically insulated away from the anode.

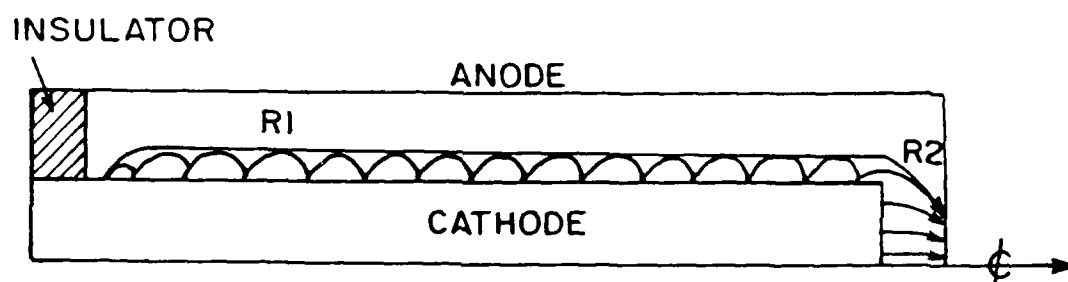
In figure 1, various electron orbit types are shown [2]. There are common, laminar, curtate and prolate orbits represented. If the electrons are emitted from the cathode into a region in which the fields are uniform in z and the electrons initially have zero velocity, common orbits result. However, if the electrons are born in regions of non-uniform fields, prolate, curtate and laminar orbits can be produced. In many pulsed power systems, prolate, curtate and laminar orbits dominate because of inherent field non-uniformities due to unavoidable perturbations in the magnetically insulated flows.

So there is no confusion, it is important to point out that there are three different types of magnetically insulated (cutoff) flows referred to in the literature [3]: 1) self-limited, 2) load-limited, and 3) constant-flux-limited flows. An example of self-limited magnetic insulation is given in figure 2a. This figure shows a power pulse propagating down a long coaxial transmission line. The current passing from the anode to the cathode at the pulse front (R2) allows for the insulation of the line at R1.

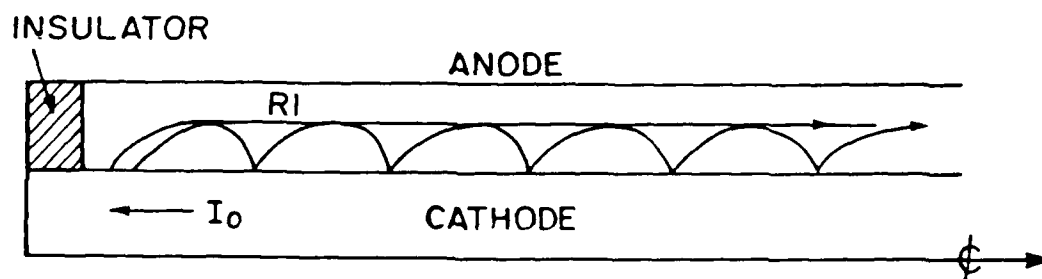
An example of load-limited magnetic insulation is shown in figure 2b. The current passing through the system is limited to that which passes through the load which is responsible for the insulation of region R1. It is interesting to note that the current passing through the



- a. Self-limited magnetically insulated flow. The current flow from the anode to the cathode at the pulse front (R2) allows for insulation in R1.



- b. Load-limited magnetically insulated flow. The current flow across R2 (load or diode gap) results in the insulation of R1.



- c. Constant-flux-limited magnetically insulated flow. A current from outside the system (I_0) is forced through the cathode and produces a magnetic field of constant flux that insulates the flow in R1.

Figure 2. Types of Magnetically Insulated Flows.

load (R_2) of figure 2b is always greater than or equal to the current lost across the pulse head (R_2) as shown in figure 2a (for insulated flows). This means that the electron flows in load-limited lines are at least as tightly trapped as electron flows in self-limited flow lines. It is also interesting to note that if the load impedance of figure 2b is increased to the point that current begins to be excluded from the diode region (load, R_2), the insulation in R_1 returns to the self-limited type.

Finally, one sees an example of a constant-flux magnetically insulated flow in figure 2c. In this case, a current is forced through the cathode from an outside power source. This current (I_0) produces a magnetic field that remains constant and is in the minus $\hat{\theta}$ direction. If a sufficiently large voltage is impressed on the line to cause emission of electrons, the imposed magnetic field will cause an $\vec{E} \times \vec{B}$ drift and magnetic insulation. However, in such systems, the currents due to the applied voltage are usually negligible--unlike the previous two cases. The power levels are low and the systems are almost always non-relativistic. This is why an insulating field must be supplied by an outside source.

In this work, the large pulsed power systems of interest [4] have relativistic electron flows and significant self-generated magnetic fields. Also, most of these systems attempt to insure that all generated currents pass through the load. For this reason, the following

research dwells primarily on load-limited magnetic insulation. To give a little more perspective and to emphasize the importance of this work a historical summary, outline of research, the basic physics and the computational tools involved are presented.

1.2 Historical Summary and Background

The theory of magnetic insulation begins with Hull's first cartesian, non-relativistic single particle treatment of magnetron cutoff [5]. Relativistic, self-consistent, cartesian treatments begin around 1973 when Lovelace and Ott found a condition governing constant-flux magnetic insulation of a diode [6]. Also, at about this same time, Ron, Mondelli, and Rostoker(RMR) developed the "quasi-laminar flow theory" employing common orbits (see figure 1) in cartesian coordinates [7]. In the work of RMR, it is assumed that the total energy and canonical momentum across the electron sheath are equal to the total energy ($W=0$) and momentum ($P_z=0$) at the cathode. With this assumption, they find the electric and magnetic fields across the sheath, which are expressed nicely in terms of elliptic functions. A laminar flow theory for magnetically insulated transmission lines (MITL) was presented by Creedon in 1975 for cartesian, cylindrical and conical geometries [8]. This theory also assumes the total energy and canonical momentum across the flow are equal to zero. It is commonly referred to as the Brillouin flow theory. Wang, in 1977, using a simple transformation showed how the equations

governing Brillouin flows could be transformed into Laplace's equation [9]. This allows one to obtain Brillouin type flow solutions with arbitrary cathode/anode cross sections. In 1979, Mendel proposed a theory in cartesian coordinates that allows for arbitrary canonical momentum and total energy profiles across the electron sheath [10] for flows with a variety of electron orbits.

Many other papers have been written in the more mathematically tractable cartesian coordinates [11-15,24]; unfortunately, a majority of experiments and applications involving magnetic insulation utilize cylindrical electrode geometries [16-23]. For this reason, it is important that the theory done in cartesian coordinates be extended to cylindrical coordinates if possible. In addition, it is desirable to carry out new theoretical developments in cylindrical coordinates. Creedon and Wang were able to extend the laminar Brillouin flow theory to cylindrical coordinates. Swegle attempted to extend RMR's work to cylindrical coordinates, but found that an equilibrium "quasi-laminar flow solution" did not exist [25]. In this work, the theoretical developments are done primarily in cylindrical coordinates.

Not surprisingly, the theoretical efforts mentioned above accompany very active experimental pulsed power programs around the world. One pulsed power effort of particular interest being actively pursued by the US [4], USSR [26], etc. is light ion beam inertial confinement

fusion(ICF). This program requires ion beam pulses with energy densities of 10^{14} Watts/cm² with rise times of 15 nanoseconds and durations greater than or equal to 20 nanoseconds. Power levels of this magnitude incident on a 1 cm³ deuterium-tritium pellet can compress and heat the target to 10^8 degrees Kelvin and thermonuclear ignition. However, the magnetically insulated transmission lines(MITL) that transport this power to a focusing region typically have electric fields well above the 20 to 50 MV/m required for explosive emission of electrons. If it were not for the exploitation of magnetic insulation, explosive electron emission would cause the entire system to short out.

In addition, to produce ion beams with the required 15 nanosecond rise times and durations greater than 20 nanoseconds at the necessary power levels requires sophisticated switching techniques. One technique that has been used successfully and is undergoing extensive research at Sandia National Laboratories, the Naval Research Laboratories, and other laboratories and universities around the world is the plasma erosion opening switch (PEOS).

A PEOS can conduct mega-Ampere levels [27] of current for tens of nanoseconds before switching the current to a load in less than ten nanoseconds. A PEOS operates as follows. First the PEOS plasma is injected through an exterior anode onto an interior cathode. Since a plasma acts as a conductor any current forced down the anode will short to the cathode and back to the power source -- forming

an inductive storage loop. When a large pulsed power source is connected to such a system, current flows down the anode to the PEOS where it shorts to the cathode. However, when the current flowing through the plasma becomes so large that the free charges in the plasma cannot carry the current the plasma begins to erode away from the cathode. As the plasma erodes away from the cathode, the impedance between the plasma bottom and cathode becomes greater than that across a downstream load. As a result, the generated current is switched to the load (see figure 15 and Chapter 4 for more information on the various phases of a PEOS opening). Now, a PEOS's successful operation depends critically on magnetic insulation. In fact, a PEOS would not open or if it did open, it would not remain open long if magnetic insulation broke down.

Unfortunately, there are many regimes in which magnetic insulation breaks down even for simple unperturbed MITLs. These regimes are complex functions of the applied voltages, line and load impedances, and the anode and vacuum currents. In addition, a variable impedance structure like a PEOS severely disrupts the magnetically insulated electron flow and often results in significant current loss. This is because an appreciable fraction of the current and power transported by the transmission lines in the regimes of interest is carried by the magnetically insulated electrons.

In order to avoid regimes in which magnetic insulation breaks down and to more clearly understand magnetically

insulated electron flows, a detailed theoretical and numerical investigation has been carried out in this work. Some parts of Mendel's theory [10] have been extended to cylindrical coordinates. In addition, a new laminar flow theory in cylindrical coordinates is presented that allows for non-zero canonical momentum and total energy profiles across the flow. The new theory includes the previous state of the art (the Brillouin flow theory) — which predicts magnetically insulated electron flows with zero canonical momentum and total energy throughout the flow — as a special case. A large number of computer simulations have been done that clearly illustrate how magnetic insulation is tied to the applied voltages, line and load impedances, and structure impedances (i.e. a PEOS) of the system.

1.3 Outline and Accomplishments

The following is a summary of what this dissertation contributes to the field. Chapters 1 and 2 illustrate the need for and the basic theory governing magnetic insulation in cylindrical pulsed power systems. Some of Mendel's work is extended to cylindrical coordinates. In comparing predictions from the resulting equations to MASK (see section 2.3), it is found that the magnetically insulated flow is laminar in nature, but has a non-Brillouin flow structure.

This motivates the derivation, in Chapter 3, of a general laminar flow theory (in cylindrical coordinates) of which the Brillouin flow theory is a special case. The new

theory is used to predict magnetically insulated electron flow properties for non-Brillouin laminar flows. It is justified by detailed comparisons with MASK runs.

In chapter 4, the electron flow downstream of an opening PEOS (or PEOS like structure) is analyzed. It is noted that a PEOS launches a magnetically insulated electron flow by means of an $\vec{E} \times \vec{B}$ drift. In addition, a set of equations is generated via the laminar flow theory developed in Chapter 3 that gives the fields and properties of the launched flow.

The criteria governing load-limited magnetic insulation are given in Chapter 5. These are presented in a graphical form for perturbed and unperturbed cylindrical pulsed power transmission lines. The threshold for the magnetic insulation of a system with a PEOS is given. It is confirmed by favorable comparisons of the theoretical predictions to an experiment done at NRL [31].

1.4 Basic Physics

The electron flows in large pulsed power systems are often relativistic and collisionless. This is in fact true of the electron flows downstream of the PEOSs and in the MITLs being considered herein. Therefore, the relativistic Vlasov equation is used as a starting point for theoretical development. It is given by equation (1) in MKS units. In fact, all equations and physical relations given in this text are expressed in the MKS system of units. The relativistic Vlasov equation for electrons is:

$$\left[\frac{\partial}{\partial t} + \vec{v} \cdot \frac{\partial}{\partial \vec{x}} - e \left[\vec{E} + \vec{v} \times \vec{B} \right] \cdot \frac{\partial}{\partial \vec{p}} \right] f(\vec{x}, \vec{p}, t) = 0 . \quad (1)$$

The relativistic electron momentum is

$$\vec{p} = \gamma m \vec{v} , \quad (2)$$

and the relativistic weighting factor is

$$\gamma = \frac{1}{(1 - \vec{v} \cdot \vec{v} / c^2)^{1/2}} . \quad (3)$$

Here \vec{v} is the directional velocity of the electron, $m \cong 9.1095 \times 10^{-31}$ kilograms (electron mass), $e \cong 1.6022 \times 10^{-19}$ coulombs (electron charge), $f(\vec{x}, \vec{p}, t)$ is the electron distribution function, \vec{E} is the electric field and \vec{B} is the magnetic induction.

The \vec{E} and \vec{B} fields are self consistently determined via Maxwell's equations:

$$\vec{\nabla} \cdot \vec{B} = 0 , \quad (4)$$

$$\vec{\nabla} \times \vec{B} = -e\mu_0 \int d^3p \vec{v} f + \frac{1}{c} \frac{\partial}{\partial t} \vec{E} . \quad (5)$$

$$\vec{\nabla} \cdot \vec{E} = -\frac{e}{\epsilon_0} \int d^3p f , \quad (6)$$

$$\vec{\nabla} \times \vec{E} = -\frac{\partial \vec{B}}{\partial t} . \quad (7)$$

The studies to be undertaken are often in equilibrium or quasi-equilibrium which allows one to drop the derivatives with respect to time in equations (1), (5), and (7). In addition, the electron density is of particular interest in much of this work. It is related to the electron distribution function $f(\vec{x}, \vec{v}, t)$ by:

$$\rho(\vec{x}, t) = -e \int d^3p f(\vec{x}, \vec{v}, t) . \quad (8)$$

The physics embodied in the relativistic Lagrangian will be a basis for much of the following. The relativistic

Lagrangian is :

$$L = -mc^2/\gamma + e\varphi(\vec{x},t) - e\vec{v} \cdot \vec{A}(\vec{x},t) , \quad (9)$$

where $\varphi(\vec{x},t)$ is the electrostatic potential and $\vec{A}(\vec{x},t)$ is the vector potential.

1.5 Computational Tools

The primary computational tools to be used are the 2-dimensional electromagnetic particle in cell (PIC) code MASK [28] and the transmission line code BERTHA [29]. Since MASK is the basis of this work's computational study, it is introduced first. MASK is referred to as an electromagnetic code because it solves the fully time dependent Maxwell's equations (equations (4) - (7)) allowing one to study electromagnetic waves with it. This is to be contrasted with electrostatic or magnetostatic codes which do not include the time derivatives seen in equations (5) and (7) and which therefore can not be used to study systems in which electromagnetic waves are important.

MASK solves Maxwell's equations in two dimensions and in cylindrical coordinates by dividing the region to be modeled (i.e. a cathode/anode gap) into a computational mesh. Maxwell's equations are finite differenced on this mesh with the electric and magnetic fields defined at each mesh point. The source of these fields are charged particles existing in and injected into the region of interest, along with the specified boundary field constraints.

Typically, each charged particle (macro particle)

represents 10^8 to 10^{11} electrons or ions. These macro-particles move through the cells of the computational mesh in accordance with the fields defined at the corresponding mesh points. The fields are used to advance the particle position within a computational cell (where the phrase particle in cell code originates) and vice versa by means of an integration technique called the leap-frog method.

The two first-order differential equations to be separately solved when using the leap frog method are [30]:

$$m \frac{d\vec{v}}{dt} = \vec{F} \quad , \quad (10)$$

and

$$\frac{d\vec{x}}{dt} = \vec{v} \quad . \quad (11)$$

Initially one must be given the particle positions and velocities along with the boundary conditions. Using a weighting scheme the particle positions and velocities are converted into charge and current densities. These, taken together with the boundary conditions, are used in conjunction with the finite differenced Maxwell's equations to update the field quantities. After the fields are obtained they are used to define the force on a given particle (the Lorentz force):

$$\vec{F}(\vec{x}, t) = -e(\vec{E} + \vec{v} \times \vec{B}) \quad . \quad (12)$$

This force is a function of the mesh cell (position) in question and time. It is used to obtain an average velocity for the particle over the time step (see equation (10)), which in turn is used to update the particle position (see

equation (11)). Given the new particle positions and velocities, charge densities and current densities are obtained which are then substituted into Maxwell's equations to obtain the time advanced fields. One should note that the charge densities used in this process are corrected for particle weighting errors by solving an electrostatic version of Poisson's equation. In addition, the charge density on the structure boundaries is modified to insure the structure potential remains as specified.

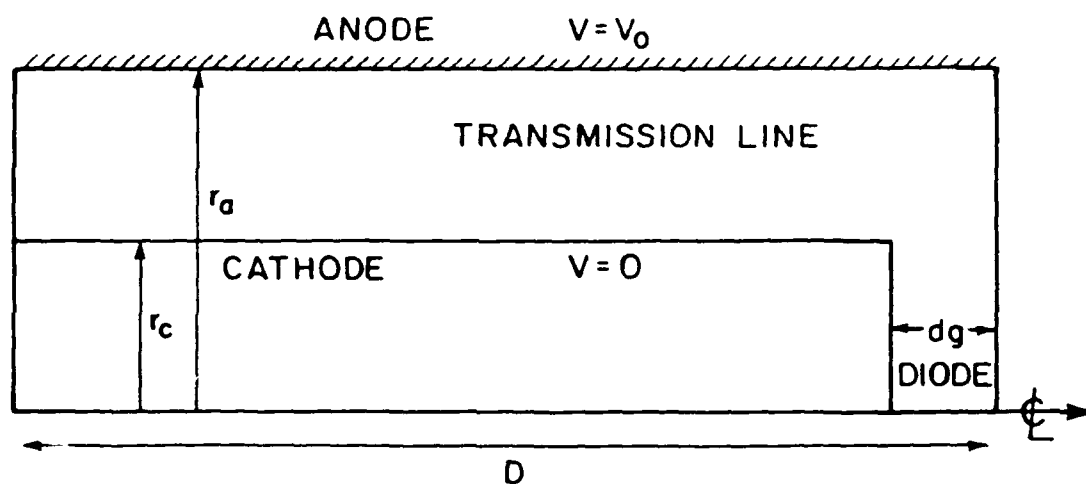
This is because fourier transforms (FFT) are being used in the Poisson solves. Since this is so, the structures within the mesh must be defined in terms of the surface charges that result in the required potential on that surface. This surface charge density must change with the changing plasma to maintain a constant potential on the structure surface.

The required surface charges are obtained by means of the capacitive matrix method (30). This method requires the precalculation of a capacity matrix C . This matrix relates the plasma induced electrode charge to the potential of the electrode. The procedure one follows is to first solve Poisson's equation with no charges on the electrode points. One then records the difference between the desired value and the potential actually found. If one then multiplies this error by C the desired charge at each mesh point along the electrode is given.

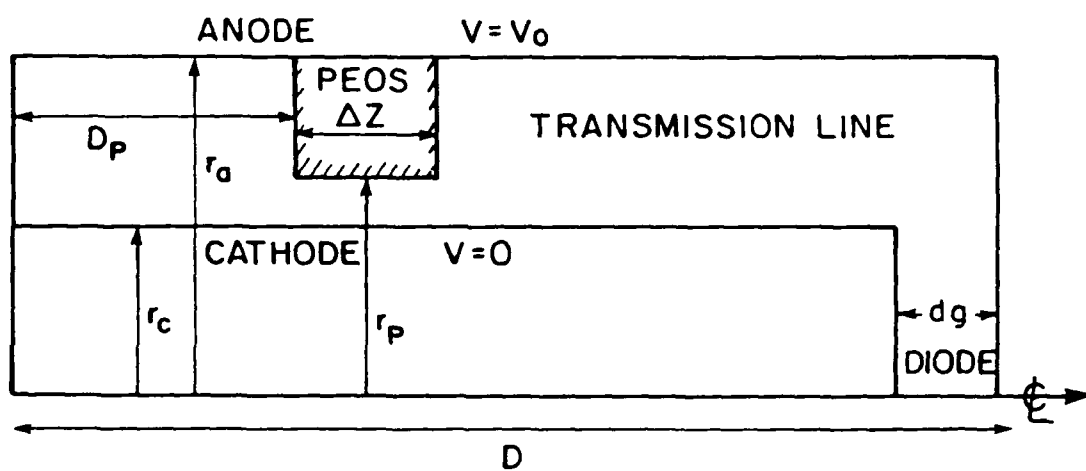
In the following, MASK results are presented for

cylindrically symmetric systems run with and without charged structures. Two sample MASK meshes are given in figure 3. Mesh 3a corresponds to the MASK runs for MITLs without any perturbations. Mesh 3b corresponds to runs for MITLs with a structure. The cross hatched areas are space charge limited (SCL) ion emitting regions (when ions are desired). The cathode is a space charge limited emitter of electrons. A space charge limited emitting surface refers to a surface covered by a thin plasma sheath. This is typical of many of the metallic surfaces encountered in the pulsed power transmission lines encountered in this study. Any electric field normal to such a plasma covered surface will cause charges to flow out of the surface plasma in such a way as to zero out the normal component of the field at the surface. The amount of charge required to zero the normal component of the electric field is easily determined using Gauss's law. MASK injects this amount of charge self consistently at the emitting surface every cycle.

Now in figures 3a and 3b, V_0 is the anode voltage; r_a is the anode radius; r_c is the cathode radius; r_p is the radial distance to the bottom edge of the structure; D_p is the distance from the left edge of the mesh to the left edge of the structure; Δz is the width of the perturbation, d_g is the diode gap spacing and D is the axial length of the system. The above parameters are varied in a series of over 100 calculations and discussed in chapter 5. The calculations are used to determine the magnetic insulation



a. The mesh set-up for simple MITL MASK simulations.



b. The mesh set-up for PEOS MASK simulations.

Figure 3. MASK meshes.

threshold as a function of applied voltage, geometry, and load impedance. They are also used to determine flow properties downstream of a PEOS.

This is done by allowing the structure depicted in figure 3b to emit ions. This ion emitting structure simulates a PEOS at some instant in time. In other words, as the switch plasma erodes away from the cathode it can be approximated by a conducting block that emits ions (SCL). In this way, one can determine the flow properties and magnetic insulation threshold for a system with a PEOS without the expense of modeling the PEOS plasma itself.

As a check on the magnetic insulation threshold determined by MASK for a system with a PEOS, a transmission line code called BERTHA utilizes the obtained threshold to simulate a Gamble II experiment [31]. The simulation results are found to correspond closely to the experimental results which partially justifies the calculational study.

BERTHA (following taken from reference (29)) follows forward and backward moving current and voltage waves and then superimposes these waves to find the physically measured voltages and currents at any point in a circuit. The current and voltage at a given point and at a given time are given by:

$$I = \frac{V_1 - V_2}{z_o} \quad (13)$$

and

$$V = V_1 + V_2 \quad (14)$$

where z_o is the line impedance and V_1 and V_2 are the

voltages of the forward going and backwards going waves respectively. From this, it is clear that the forward going power flow is given by:

$$P = IV = (V_1^2 - V_2^2)/z_0 \quad (15)$$

When the voltage waves are incident on an impedance discontinuity, as between the MITL and load the incident wave is partially reflected and partially transmitted (see figure 4). The reflection and transmission coefficients are given by:

$$r = \frac{z_L - z_0}{z_L + z_0} \quad (16)$$

and

$$t = \frac{2z_L}{z_L + z_0} \quad (17)$$

where z_L is the load impedance. Any number of reactive or non-reactive circuit components may be included in a given problem. For more details on this, see reference [29].

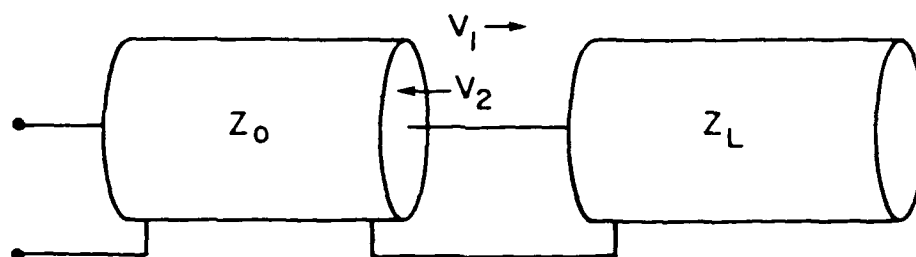


Figure 4. Transmission Line Elements.

Z_0 is the line impedance and Z_L is the load impedance.

CHAPTER 2

BASICS OF CYLINDRICAL MAGNETICALLY INSULATED TRANSMISSION LINE THEORY

Because a majority of experiments involving magnetic insulation utilize coaxial cylindrical geometries, and because of the lack of theoretical development in cylindrical coordinates, magnetic insulation in cylindrical coordinates is considered here. Parts of Mendel's cartesian theory [10] are extended to cylindrical coordinates and checked using a pressure balance analysis. In comparisons of the theoretical results to MASK calculations and in examination of particle orbits it is determined that the electron orbits in many MITLs are laminar in nature. As a result, the only laminar electron flow theory available in cylindrical coordinates — the Brillouin flow theory — is presented (no one has yet been able to produce a self-consistent non-laminar flow theory in cylindrical coordinates). Unfortunately, the laminar electron flows it predicts do not correspond to those obtained in a variety of MASK computer experiments. This motivates the development of a general theory for laminar flows in cylindrical coordinates which is presented in Chapter 3.

2.1 Extend Cartesian Theory to Cylindrical Coordinates

The nature of the problem is shown in figure 1. A voltage difference (in MV regime) is set across a coaxial transmission line and after a few nanoseconds an equilibrium

magnetically insulated state is established. The electrons that are emitted from the cathode in a space charge limited fashion enter a variety of orbits — common, curtate, prolate, laminar, etc. — depending on non-uniformities in the fields.

Since the net flow of current inside the transmission line is in the $-\hat{z}$ direction (figure 1), and there is azimuthal symmetry the magnetic field between the anode and cathode will be an r dependent field in the $\hat{\theta}$ direction: $\vec{B} = B(r)\hat{\theta}$. In addition, neglecting end effects, the gradient of the applied potential yields an r -dependent electric field: $\vec{E} = E(r)\hat{r}$. Because an equilibrium state is being considered all time dependent terms are dropped at the start of the theoretical development.

Now, applying Gauss's law (from equation (6)) in conjunction with the relativistic Vlasov equation (equation (1)) implies:

$$\vec{\nabla} \cdot \vec{E} = \nabla_r^2 \varphi(r) = -\rho(r)/\epsilon_0 = \frac{e}{\epsilon_0} \int dp_z \int dp_r f(p_r, p_z) \quad . \quad (18)$$

where $\nabla_r^2 = 1/r(\frac{\partial}{\partial r}(r\frac{\partial}{\partial r}))$, $\varphi(r)$ is the potential as a function of r across the transmission line, $\rho(r)$ is the electron charge density, ϵ_0 is the permittivity of free space, e is the electron charge, p_z and p_r are the z and r components of momentum respectively, and $f(p_r, p_z)$ is the p_r, p_z space electron density.

It is also true that if $\vec{B} = B(r)\hat{\theta}$ then:

$$(\vec{\nabla} \times \vec{A})_{\theta} = \left(\frac{\partial A_r}{\partial z} - \frac{\partial A_z}{\partial r} \right) \hat{\theta} \quad (19)$$

Since there is no electron flow loss in the radial direction and the electron orbits exist uniformly throughout the electron sheath, there is no net radial electron flow as a function of r . This is because for every electron moving towards the cathode there is one moving towards the anode in every macroscopic control volume. As a result $A_r = 0$.

Therefore,

$$B(r) \hat{\theta} = - \left(\frac{\partial A_z}{\partial r} \right) \hat{\theta} \quad (20)$$

This means Ampere's law (equation (5)) becomes

$$\vec{\nabla} \times \vec{B} = \nabla_r^2 A_z \hat{z} = \mu_0 \vec{J} \quad (21)$$

Rewriting (equation (21)) in terms of the distribution function $f(p_r, p_z)$ gives:

$$\nabla_r^2 A(r) = \mu_0 e \int dp_z \int dp_r \frac{p_z}{r} f(p_r, p_z) \quad (22)$$

It is convenient to write equations (18) and (22) in terms of the canonical momentum and total energy. The appropriate Jacobian of the transformation is given by:

$$\det \left(\frac{\partial q_i}{\partial x_j} \right) = \begin{vmatrix} \frac{\partial p_r}{\partial p_{cz}} & \frac{\partial p_r}{\partial w} \\ \frac{\partial p_z}{\partial p_{cz}} & \frac{\partial p_z}{\partial w} \end{vmatrix} \quad (23)$$

where p_{cz} is the z -component of canonical momentum and w is the total energy of a flow electron. The components of the Jacobian can be found using the relativistic Lagrangian subject to the constraints on the fields mentioned previously:

$$L = -mc^2(1 - (\dot{r}^2 + \dot{z}^2)/c^2)^{1/2} + e\varphi(r) - e\dot{A}_z(r) . \quad (24)$$

The z -component of canonical momentum and momentum are respectively:

$$p_{cz} = \frac{\partial L}{\partial \dot{z}} = m\dot{z} - eA_z(r) , \quad (25)$$

and

$$p_z = m\dot{z} = p_{cz} + eA_z(r) . \quad (26)$$

The r -component of canonical momentum and momentum are given by:

$$p_{cr} = \frac{\partial L}{\partial \dot{r}} = m\dot{r} = p_r . \quad (27)$$

The total energy is easily shown to be:

$$w = (\gamma - 1)mc^2 - e\varphi(r) . \quad (28)$$

For convenience these relations are written in dimensionless form in terms of:

$$W = w/mc^2 , \quad (29)$$

$$\phi = 1 + e\varphi/mc^2 , \quad (30)$$

$$\alpha = eA_z/mc , \quad (31)$$

$$P_x = p_x/mc , \quad (32)$$

where the subscripted x of equation (32) refers to x^{th} component of momentum.

In this new notation, equations (25)-(28) become:

$$P_{cz} = P_z - \alpha , \quad (33)$$

$$P_{cr} = P_r = ((W + \phi)^2 - 1 - (P_{cz} + \alpha)^2)^{1/2} , \quad (34)$$

$$W = \gamma - \phi . \quad (35)$$

This means the Jacobian is (from equation (23)):

$$\det\left(\frac{\partial q_i}{\partial x_j}\right) = - \frac{W + \phi}{((W + \phi)^2 - 1 - (P_{cz} + \alpha)^2)^{1/2}} . \quad (36)$$

Equations (18) and (22) can now simply be written non-dimensionlessly in terms of the total energy and canonical momentum:

$$\nabla_r^2 \phi = \iint \frac{\Lambda(r, P_{cz}, W)(\phi+W)dP_{cz}dW}{((\phi+W)^2 - 1 - (P_{cz} + \alpha)^2)^{1/2}} \quad (37)$$

$$\nabla_r^2 \alpha = \iint \frac{\Lambda(r, P_{cz}, W)(P_{cz} + \alpha)dP_{cz}dW}{((\phi+W)^2 - 1 - (P_{cz} + \alpha)^2)^{1/2}} \quad (38)$$

All that remains is to define $\Lambda(r, P_{cz}, W)$:

$$\Lambda(r, P_{cz}, W) \equiv \frac{1}{r} \frac{2e\mu}{mc} o |j(P_{cz}, W)| \equiv \frac{1}{r} F(P_{cz}, W) \quad (39)$$

This expression follows from arguments found in Appendix A (which is a derivation of equations (37) and (38) from a slightly different point of view).

In order to avoid rewriting the large integral arguments of (37) and (38) the following definition is given:

$$G(\phi, \alpha) \equiv \iint F(P_{cz}, W)((\phi+W)^2 - 1 - (P_{cz} + \alpha)^2)^{1/2} dP_{cz} dW \quad (40)$$

This allows one to write (37) and (38) as:

$$\nabla_r^2 \phi = \frac{1}{r} \frac{\partial G(\phi, \alpha)}{\partial \phi} \quad (41)$$

and

$$\nabla_r^2 \alpha = -\frac{1}{r} \frac{\partial G(\phi, \alpha)}{\partial \alpha} \quad (42)$$

Now, multiplying equation (41) by $\frac{d\phi}{dr}$ and equation (42) by $-\frac{d\alpha}{dr}$ and adding (with $\frac{d}{dr} \equiv ')$ gives:

$$[r(\phi'^2 - \alpha'^2)]' + (\phi'^2 - \alpha'^2) = 2G' \quad (43)$$

Another useful equation in the following work is obtained by multiplying equation (43) by r and regrouping:

$$[r^2(\phi'^2 - \alpha'^2)]' = 2((rG)' - G) \quad (44)$$

Since most of the theory in this dissertation is related to these equations it is crucial that they be true. In the next section, a pressure balance study is performed that justifies equations (43) and (44). Further justification is given in section 2.4 where the well known Brillouin flow results are obtained by taking a limiting case of equation (43).

2.2 Pressure Balance Check

In this section, equation (43) is used to obtain the electric field and magnetic induction at the sheath edge. This is compared to the expressions obtained for the fields using the Maxwell-Stress Tensor. The fields are obtained from the stress tensor by noting that the electron cloud flows down the axis (\hat{z}) in equilibrium. Since the electron sheath neither moves toward the anode nor the cathode the sum of forces must be zero (see figure 5):

$$\begin{aligned}\vec{F} &= \frac{d}{dt}(P_{\text{mechanical}} + P_{\text{field}}) = 0 \\ &= \int_{\text{vol}} \vec{\nabla} \cdot \vec{T} d^3x = \int \hat{n} \cdot \vec{T} ds\end{aligned}\quad (45)$$

$$\begin{aligned}\text{Now, } \vec{T} &= \frac{1}{4\pi} (\vec{E}\vec{E} + \vec{B}\vec{B} - \frac{1}{2} \vec{I}(E^2 + B^2)) \\ &= \text{Maxwell-Stress Tensor}\end{aligned}\quad (46)$$

where P refers to the momentum. If one substitutes the fields $\vec{E} = E(r)\hat{r}$ and $\vec{B} = B(r)\hat{\theta}$ into equation (46) and then substitutes the result into equation (45) the following is found:

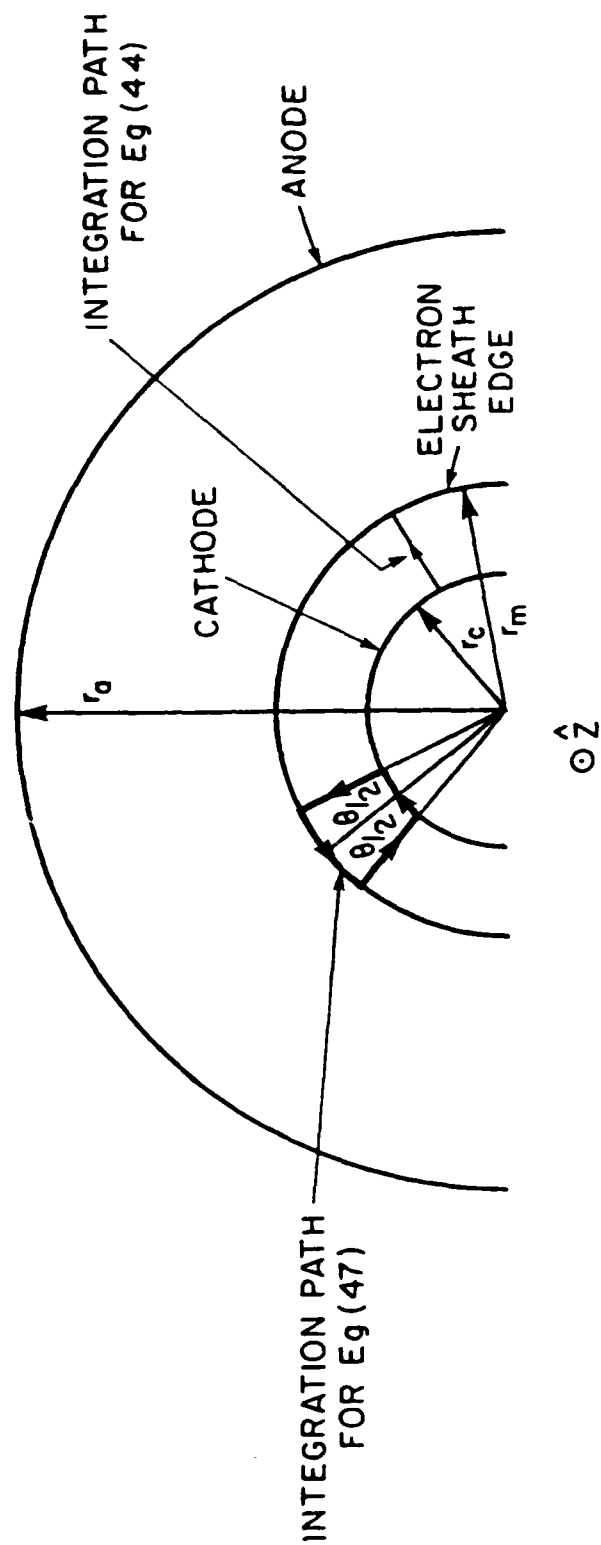


Figure 5. MITL for Maxwell-Stress Tensor Analysis.

$$\vec{F} = \frac{1}{8\pi} \left[\int_{-\theta/2}^{\theta/2} \left[(E(r_m)^2 - B(r_m)^2) r_m - (E(r_c)^2 - B(r_c)^2) r_c \right] \hat{r} d\theta \right. \\ \left. + \int_{r_c}^{r_m} \left[(B(r)^2 - E(r)^2) \hat{\theta} \Big|_{\theta/2} - (B(r)^2 - E(r)^2) \hat{\theta} \Big|_{-\theta/2} \right] dr \right] , \quad (47)$$

where $\hat{r} = -\hat{i}\sin\theta + \hat{j}\cos\theta$ and $\hat{\theta} = -\hat{i}\cos\theta - \hat{j}\sin\theta$. After, integrating (47), rearranging terms and assuming space charge limited emission ($E(r_c) = 0$) one obtains:

$$E(r_m)^2 = c^2(B(r_m)^2 - \frac{r}{r_m} B(r_c)^2) + \\ c^2/r_m \int_{r_c}^{r_m} (B(r)^2 - \frac{E(r)^2}{c^2}) dr \quad . \quad (48)$$

Now, if one integrates equation (43) over the entire sheath, equation (48) is again obtained. This indicates equations (43) and (44) are indeed true statements.

It is interesting to note that the integral term on the right hand side of equation (48) is composed of terms due to electromagnetic stresses in the flow (attributable to non-laminar orbits and the cylindrical geometry). This term is non-existent in cartesian coordinates. The expression on the left hand side in equation (48) and the first term on the right are pure pressure terms.

2.3 Laminar Nature of Electron Flows

In this section, equation (44) is integrated and the magnitudes of the stress tensor terms (P_m of equation (49)) are found to be relatively small. In addition, particle orbits for representative MASK MITL calculations are examined. The stress tensor check and the simulations

indicate very laminar electron orbits. This is exploited in chapter 3.

First, integrating equation (44) from the cathode (r_c) to the sheath edge (r_m) yields (see figure 5):

$$r_m^2(\phi_m'^2 - \alpha_m'^2) - r_c^2(\phi_c'^2 - \alpha_c'^2) = \int_{r_c}^{r_m} G dr = P_m \quad (49)$$

where the subscripts m and c refer to the sheath edge and cathode radii respectively. Writing equation (49) in dimensional form and noting that $B_m = \frac{\mu_0 I_a}{2\pi r_m}$ and $B_c = \frac{\mu_0 I_c}{2\pi r_c}$ (by Ampere's law where I_c is the cathode current and I_a is the anode current) implies:

$$\vec{E}_m = - \frac{c\mu_0}{2\pi r_m} (I_a^2 - I_c^2)^{1/2} \left[1 - \frac{4\pi c P_m}{\mu_0 (I_a^2 - I_c^2)} \right]^{1/2} \hat{r} \quad (50)$$

where \vec{E}_m is the electric field at the sheath edge (r_m). It is also true that (from Gauss's law):

$$\vec{E}_m = \frac{I_a - I_c}{2\pi\epsilon_0 r_m \bar{v}_d} \hat{r} \quad (51)$$

where \bar{v}_d is the average drift velocity of the electron flow.

From (50) and (51) one sees that:

$$\bar{v}_d = c \left[\frac{I_a - I_c}{I_a + I_c} \right]^{1/2} \left[1 - \frac{4\pi c P_m}{\mu_0 (I_a^2 - I_c^2)} \right]^{-1/2} \quad (52)$$

It is also obvious that the electric field at the anode is given by:

$$E_a = \frac{r_m E_m}{r_a} \quad (53)$$

In table 1, the electric field at the anode (E_a) for various MASK simulations corresponding to figure 3a and Appendix C1 and C2 are given. In addition, the electric

field occurring at the anode for the corresponding theoretical laminar flow (using MASK generated anode (I_a) and cathode (I_c) currents) is presented for comparison. The laminar flow electric field at the anode can be obtained from equations (50) and (53) if one realizes P_m of (50) equals zero for laminar flows because the radial component of momentum equals zero for ($P_r = 0$) all laminar flow electrons. From equation (34) and (40) this implies $G(\phi, \alpha) = 0$, and from (49) that $P_m = 0$.

The percentage difference between the MASK and laminar electric fields at the anode are given in Table 1. It is clear, from the table, that the electric fields are close (within plus or minus 5 percent except for simulations M407-M412) to what they would be for laminar flows. In figures 6a and 6b one can examine the electron orbits for a couple of these problems and see their laminar nature.

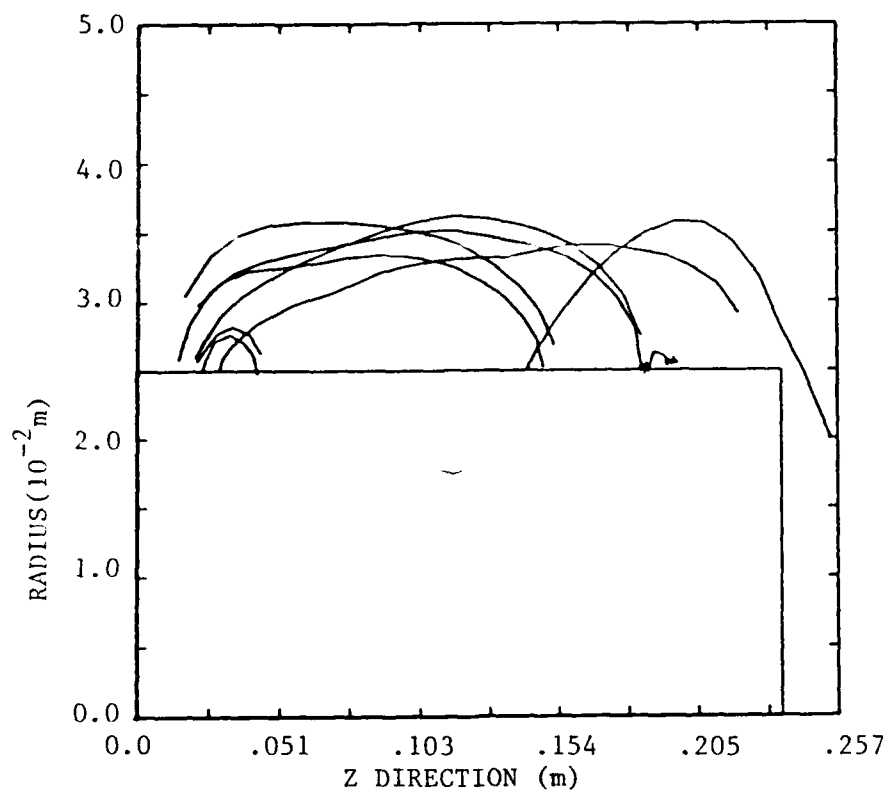
Simulation	I_a	I_c	E_a	Laminar E_a	% Diff
M407-M412	-1.56×10^5	-1.46×10^5	-6.1×10^7	-6.6×10^7	7.5
M417, M419	-7.86×10^4	-3.44×10^4	-8.3×10^7	-8.5×10^7	2.2
M418, M420	-8.46×10^4	-6.5×10^4	-6.8×10^7	-6.5×10^7	-4.8
M414	-9.85×10^4	-8.4×10^4	-6.3×10^7	-6.2×10^7	-1.6
M424	-7.96×10^4	-3.5×10^4	-8.5×10^7	-8.6×10^7	1.0
M458	-1.77×10^4	-1.6×10^4	-9.4×10^6	-9.3×10^6	-1.4

Table 1. Comparison of anode electric fields from MASK and laminar theory (I_a and I_c have the same sign because they are defined in terms of a system current loop).

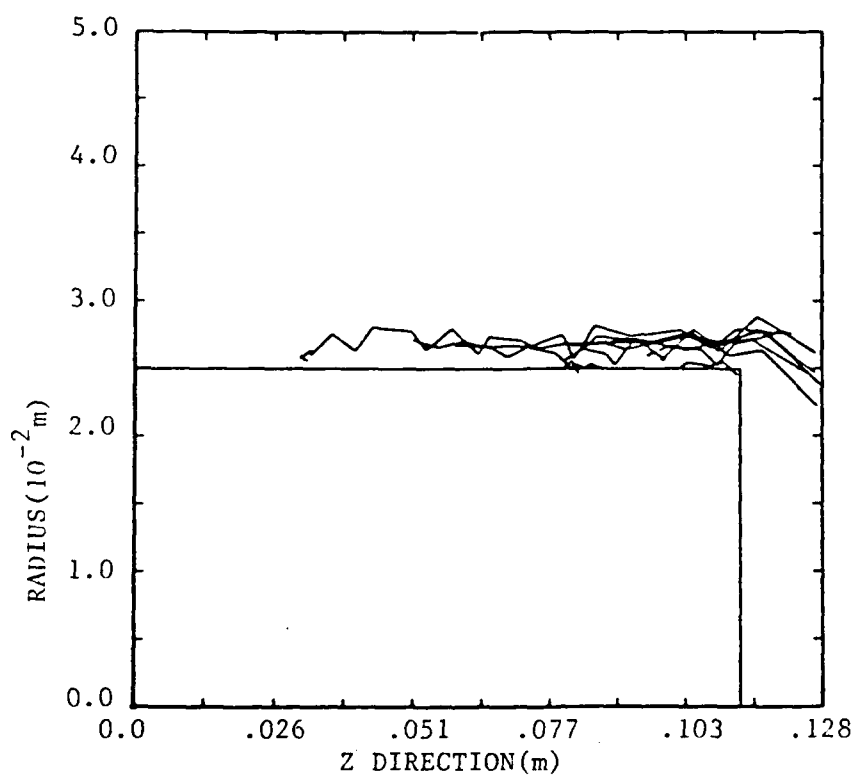
For figure 6a (simulation M424, see Appendix C1), it is clear that many of the emitted electrons are traveling .15 to .2 meters before returning to the cathode. For common orbits (see figure 1), the electrons will travel approximately 2 Larmour radii in the \hat{z} direction before returning to the cathode. For this problem, the average Larmour radius is approximately $r_l = .0035$ m. This means the electrons are traveling approximately 60 Larmour radii in the \hat{z} direction before returning to the cathode. The orbits are very laminar as a result. Perturbations and gradients in the electric and magnetic fields are responsible for this state of affairs.

For figure 6b (simulation M414), the electron orbits are confined more closely to the cathode. This increases the likelihood of an electron returning to the cathode. Nevertheless, the orbits shown in 6b are curtate and prolate. They are periodic, with a period in z of approximately .01 m. The average Larmour radius is approximately .001 m; so, the electrons travel 10 Larmour radii in z per gyration. Their total displacement in r per gyration is approximately 1.5 Larmour radii. Therefore, the orbits are also very laminar in nature.

The laminar nature of the electron flow observed with MASK in cylindrical coordinates is consistent with MAGIC (a 2-dimensional electromagnetic PIC code) simulations done in cartesian coordinates at Sandia. In the Sandia simulations,



a. Semi-laminar loosely trapped flow (Simulation M424).



b. Semi-laminar tightly trapped flow (Simulation M414).

Figure 6. MASK Semi-Laminar Flows.

it was found that MITL flows in cartesian coordinates are laminar in nature but non-Brillouin [32]. By non-Brillouin it is meant that the canonical momentum and total energy are non-zero across the electron sheath. The assumption of a canonical momentum and total energy equal to zero across the sheath is fundamental to the Brillouin flow theory. In this work, the non-Brillouin nature of the flow is ascertained in cylindrical coordinates by examining a laminar flow and comparing it to the Brillouin solution. All the simulations presented in Table 1 are non-Brillouin laminar flows. This is shown in detail for cases M458, M420 and M424 by comparing their magnetic field profiles to a Brillouin flow solution in section 3.4.

2.4 Brillouin Flow Theory Derivation

In this section the Brillouin flow theory is derived as a special case of equations (40) and (43). This derivation is done to familiarize the reader with the state of the art in cylindrical MITL flow solutions which will become a special case of the more general theoretical developments to be presented in Chapter 3.

For this derivation, it is assumed that the radial component of velocity (\dot{r}) for electrons in the flow field is zero (as it must be for laminar flows). It is also assumed that the total energy and canonical momentum across the flow are equal to zero. This is a characteristic of Brillouin flows and comes from assuming the electrons have zero energy and momentum at the cathode, and energy and momentum

conservation. It is also assumed that the fields are uniform in the \hat{z} direction. The last assumption is typically not satisfied in experiments because of end effects, transitions, instabilities, cavity modes, and all other perturbing effects. The non-uniform fields are responsible for non-Brillouin flows. However, in the following, one is considering a non-perturbed laminar electron flow.

Now, if one sets the total energy and canonical momentum equal to zero in equation (40) one obtains:

$$G(\phi, \alpha) \equiv u = (\phi^2 - 1 - \alpha^2)^{1/2} \quad (54)$$

and

$$u' = \frac{\phi\phi' - \alpha\alpha'}{u} \quad (55)$$

This implies equation (43) becomes:

$$(\phi'^2 - \alpha'^2) + [r(\phi'^2 - \alpha'^2)]' = 2u' \quad (56)$$

It is important to note that

$$\dot{r} = \frac{c}{\gamma} (\phi^2 - 1 - \alpha^2)^{1/2} = \frac{cu}{\phi} = 0 \quad (57)$$

This implies $u = 0$, which forces the derivative of u with respect to r to also be equal to zero: $u' = 0$.

With u equal to zero, equation (54) becomes:

$$\phi^2 - \alpha^2 = 1 \quad (58)$$

In addition, with $f(r) = (\phi'^2 - \alpha'^2)$, the integration of equation (56) gives:

$$f(r) = (\text{const}/r)^2 \quad (59)$$

Relation (58) leads one to try a solution in which

$\phi = \cosh S(r)$, and $\alpha = \sinh S(r)$. This coupled with (59) implies $S'(r)^2 = (\text{const}/r)^2$ or that:

$$\frac{dS(r)}{dr} = \frac{\text{const1}}{r} \text{ which implies } S(r) = \text{const2} \ln r . \quad (60)$$

To simplify matters, space charge limited emission is assumed so that the electric field at the cathode is zero. Also, the electrostatic potential and vector potential are conveniently set to zero at the cathode. The magnetic field at the cathode is given by Ampere's law ($B_c = \mu_o I_c / 2\pi r_c$). The total current flowing in the system is governed by the potential at the sheath edge and at the anode in conjunction with the system geometry. In a somewhat lengthy derivation [8], Creedon relates these quantities for a Brillouin flow. He finds the anode current to be (this relation is obtained independently of Creedon in Chapter 3):

$$I_a = \frac{2\pi mc^2}{\mu_o ce} \frac{\gamma_m}{\ln(r_a/r_c)} \left[\ln(\gamma_m + (\gamma_m^2 - 1)^{1/2}) + \frac{\gamma_a - \gamma_m}{(\gamma_m^2 - 1)^{1/2}} \right] . \quad (61)$$

He also shows that the potential at the sheath edge for a Brillouin flow is related to the anode and cathode currents by (this is also independently obtained in Chapter 3):

$$\gamma_m = I_a / I_c . \quad (62)$$

where γ_m is the relativistic factor at the sheath edge and γ_a is the relativistic factor at the anode. γ is related to the potentials by $\gamma = \frac{1 + eV}{mc^2}$. Where V is the electrostatic potential in question. Equation (62) coupled with equation (61) places a restriction on the allowed ratios of anode currents to cathode currents in the Brillouin flow theory. The theory will not satisfy Ampere's law if equations (61) and (62) are not simultaneously satisfied. An example of

the Brillouin flow theory not satisfying Ampere's law is shown in Chapter 3.

From equations (29)-(32), (59)-(62) and the fact that $\phi = \cosh S(r)$ and $\alpha = \sinh S(r)$ one obtains the following self-consistent MITL flow solution:

$$\varphi(r) = \frac{m_o c^2}{e} (\cosh(A \ln(r/r_c)) - 1) \quad , \quad (63)$$

$$\vec{A}(r) = \frac{m_o c}{e} \sinh(A \ln(r/r_c)) \hat{z} \quad , \quad (64)$$

$$\vec{E}(r) = -\frac{m_o c^2}{e} \frac{A}{r} \sinh(A \ln(r/r_c)) \hat{r} \quad , \quad (65)$$

$$\vec{B}(r) = -\frac{m_o c A}{e r} \cosh(A \ln(r/r_c)) \hat{\theta} \quad , \quad (66)$$

$$\vec{v}(r) = c \tanh(A \ln(r/r_c)) \hat{z} \quad , \quad (67)$$

$$\rho(r) = -\frac{m_o c^2 \epsilon_o A^2}{e r^2} \cosh(A \ln(r/r_c)) \quad , \quad (68)$$

$$r_m = r_c \exp\left(\frac{\cosh^{-1} \gamma_m}{A}\right) \quad , \quad (69)$$

$$A = \frac{1}{\ln(r_a/r_c)} \left[\cosh^{-1} \gamma_m + \frac{\gamma_o - \gamma_m}{(\gamma_m^2 - 1)^{1/2}} \right] \quad , \quad (70)$$

where φ is the electrostatic potential, \vec{A} is the vector potential, \vec{E} is the electric field, \vec{B} is the magnetic induction, \vec{v} is the particle velocity, ρ is the electron charge density, and r_m is the electron sheath edge radius.

These relations were first presented by Wang and DiCapua in 1980 [33] based on Creedon's findings given in equations (61) and (62). Till now, this set of equations was the only self consistent cylindrical MITL flow solution.

Unfortunately, the Brillouin flow solution does not correspond to numerical simulations done around the country — which show laminar but non-Brillouin flows. The discrepancy is due to the fact that the more realistic 2-dimensional simulations allow for perturbations in the system not taken into account in the Brillouin flow theory. This deficiency is eliminated by theoretical developments presented in the next chapter.

CHAPTER 3

GENERAL THEORY OF LAMINAR FLOWS

Until now, the only relativistic self-consistent MITL flow solution in cylindrical coordinates was given by the Brillouin flow theory which applies specifically to laminar electron flows with zero canonical momentum and total energy across the sheath. This corresponds to an ideal system with no perturbations. Unfortunately, all experimental systems have perturbations and end effects.

In this chapter, a general theory for laminar MITL flows is presented in which perturbed flows can be modeled. The Brillouin flow theory is found to be one of an infinite number of possible laminar MITL flow solutions predicted by the more general theory. From the general theory, it is discovered that the specification of a density profile determines unique values of the total energy and momentum across the flow. With this in mind a density profile is generated based on equations (40) and (43). The profile is then used to generate the complete Brillouin flow solution via the general theory of laminar flows. The canonical momentum and total energy are found to be zero (figure 11b) as expected. This comprises an independent derivation of the Brillouin flow theory and a check of the general theory of laminar flows.

The general theory is then used to simulate several MASK calculations for short MITL's in which the density profile across the flow is approximately constant and

therefore non-Brillouin. These are considered because of the ease of generating a self-consistent theoretical set of equations for a constant density profile. It should be emphasized at this point however, that any density profile could be substituted into the key equations((75)-(84)) to obtain a self-consistent laminar MITL flow solution. It should also be emphasized that the specification of a density profile is equivalent to specifying the canonical momentum and total energy across the flow, or specifying the velocity profile, or the magnetic field profile, etc. In other words, given one type of detailed information about the flow the general theory allows one to obtain all other pertinent flow quantities. Since it is especially convenient to do this using the density profile, the following work is presented as if one had knowledge of the density profile across the flow.

Nevertheless, if one had detailed knowledge of the magnetic fields or current across the sheath (from experiments), the following equations are still useful. After coding them on the computer, the density profile could be altered iteratively until the magnetic field or current profile of interest across the sheath is duplicated. One would then have a complete flow solution given a minimum of information.

3.1 Relation Between the Density and Velocity Profiles

The general theory is obtained via a surprising relation between the density and velocity profile for

relativistic MITL flows. A specification of the density profile implies a particular velocity profile and vice versa.

This interesting result is derived in Appendix B in which the following procedure is carried out: First, equation (43) is integrated from the cathode to some arbitrary r within the sheath. The integrated result is rearranged so that the electric field ($\vec{E}(r)$) is set on the left hand side of the equation. Using Ampere's law, the magnetic field quantities on the right hand side of the equation are written in terms of the anode and cathode currents. Then, equation (44) is integrated from the cathode to r to obtain another expression for \vec{E} . The resulting equations are evaluated at the sheath edge (r_m) and equated. After differentiation and algebraic manipulation a relation between the density and velocity is obtained. This relation is (given in Appendix B):

$$f(r) = \frac{1}{1-k} \frac{g(r)}{g(r)^2} \quad (71)$$

$$\text{where } l \equiv \frac{2I_c}{I_a + I_c} \quad (72)$$

$$k \equiv \frac{I_a - I_c}{I_a + I_c} \quad (73)$$

and

$$g(r) = \frac{1}{f(r)} \frac{1}{I_a - I_c} \int_{r_c}^r \rho(r) v(r) 2\pi r dr \quad (74)$$

Now $f(r)$ is defined in terms of the density as:

$$f(r) = \frac{\int_{r_c}^r \rho(r) r dr}{\int_{r_c}^{r_m} \rho(r) r dr} \quad (75)$$

where $f(r)$ is a normalized weighted average of the electron charge. It equals zero at the cathode and smoothly increases until reaching the value of one at the sheath edge (not to be confused with the distribution function $f(P_{cz}, W)$ in the Vlasov equation).

Simple calculus and algebraic manipulation of equations (71)-(75) results in a more clearly defined relation between the velocity and density profiles (this is done in Appendix B):

$$\vec{v}(r) = \frac{I_c}{2\pi \int_{r_c}^r \rho(r) r dr} \left[\left[1 + \frac{(I_a^2 - I_c^2) f^2(r)}{I_c^2} \right]^{1/2} - \left[1 + \frac{(I_a^2 - I_c^2) f^2(r)}{I_c^2} \right]^{-1/2} \right] \hat{z} \quad (76)$$

where I_a is the anode current, I_c is the cathode current, $\rho(r)$ is the density profile and $f(r)$ is the normalized weighted density profile.

3.2 Laminar Flow Equations

Given a density profile and the corresponding velocity profile (equation (76)), the self-consistent MITL flow solution is easily obtained via Maxwell's equations (subject

to the restrictions of section 2.1). The resulting equations are collected below in a convenient form. Given the charge density ($\rho(r)$) and the velocity (from equation (76)) the current density is :

$$\vec{j} = \rho(r)\vec{v}(r) \quad . \quad (77)$$

The electric field is

$$\vec{E}(r) = \frac{\int_{r_c}^r \rho(r) r dr}{\epsilon_0 r} \hat{r} \quad , \quad (78)$$

where $\vec{E}(r_c) = 0$, because the cathode is a space charge limited emitter of electrons. The corresponding electrostatic potential is

$$\varphi(r) = -\int_{r_c}^r E(r) dr \quad , \quad (79)$$

where $\varphi(r_c)$ is chosen to be zero. The magnetic induction is simply written as

$$\vec{B}(r) = \frac{\mu_0}{r} \left[\int_{r_c}^r j(r) r dr + \frac{I_c}{2\pi} \right] \hat{\theta} \quad . \quad (80)$$

The vector potential is

$$\vec{A}(r) = -\int_{r_c}^r B(r) dr \hat{z} \quad . \quad (81)$$

where $\vec{A}(r_c) = 0$ is chosen to equal zero at the cathode.

Now, from equations (26) and (35) the canonical momentum and total energy across the flow are given by:

$$P_{cz}(r) = mrv(r) - eA(r) \quad ,$$

$$= \frac{m v(r)}{(1 - v^2(r)/c^2)^{1/2}} - eA(r) \quad (82)$$

The total energy is

$$W(r) = -mc^2 \left[1 - \frac{1}{(1 - v^2(r)/c^2)^{1/2}} \right] - e\phi(r) \quad (83)$$

Also for laminar flows,

$$\vec{E}(r) = -\vec{v}(r) \times \vec{B}(r) \quad (84)$$

Equations (76), (78), and (81) must satisfy equation (84). For this reason equation (84) is used to check the validity of laminar flow solutions produced by the general theory. An example of this kind is shown in figure 10b.

If the sheath edge radius (r_m) in equation (75) is unknown it is easily found given I_a , I_c , the applied voltage across the gap (V_a) and equations (76)-(79). This is done for the constant density flow derived in section 3.3.2. From an experimental point of view, it is much more desirable to have the MITL flow as a function of I_a , I_c and V_a rather than I_a , I_c and r_m . This is because the applied voltage across the diode is usually known; the outer sheath edge radius of the electron flow is not.

In the foregoing, it was stated that given only a density profile, a self-consistent MITL flow solution is obtained. This is indeed true; however, if one desires the particulars of a solution for a given voltage, line impedance, and load impedance (or equivalently voltage, line impedance, and anode and cathode currents) the latter must be supplied. Equations (71)-(84) were presented with this in mind.

3.3 Two Derivations

In order to demonstrate the general theory of laminar flows, a couple of interesting MITL flows are derived. First, the Brillouin flow theory is derived independent of Creedon's total current relation (equation (61)). The two independently derived theories are plotted against each other and are found to match.

Then, the general theory is used to generate a self-consistent MITL flow solution for flows with constant density profiles. This is done because in simulations of short MIT's, quasi-constant density profiles were observed. The theory is then compared to the simulations and found to accurately predict quantities of interest.

3.3.1 Brillouin Flow

In this section an independent derivation of the Brillouin flow theory is presented. Starting from equations (40) and (43), one quickly obtains equations (58)-(60), and the relations $\phi = \cosh S(r)$ and $\alpha = \sinh S(r)$ as shown in section 2.4. From these and Maxwell's equations it is easy to show that the Brillouin density profile will have the following form:

$$\rho(r) = - \frac{mc^2 \epsilon_0}{e} \frac{A_n^2}{r^2} \cosh(A_n \ln(r/r_c)) \quad (85)$$

This is equivalent to equation (68) except that the critical constant " A_n " (equation (70)), previously obtained from Creedon's analysis, is indeterminate. Since Creedon's results are not needed and in fact are derivable from the

general theory, the following constitutes an independent derivation of the Brillouin flow theory.

From equation (85), equation (75) becomes:

$$f(r) = \frac{\sinh(A_n \ln(r/r_c))}{\sinh(A_n \ln(r_m/r_c))} \quad (86)$$

This means the velocity (equation (76)) becomes:

$$\vec{v}(r) = \frac{e|I_c|}{2\pi m c^2 \epsilon_0 A_n \sinh(A_n \ln(r/r_c))} \left[(1+m_1 \sinh^2(A_n \ln \frac{r}{r_c}))^{1/2} - (1+m_1 \sinh^2(A_n \ln \frac{r}{r_c}))^{-1/2} \right] \hat{z} \quad (87)$$

$$\text{where } m_1 = \frac{I_a^2 - I_c^2}{I_c^2 \sinh^2(A_n \ln(r_m/r_c))} \quad (88)$$

Now, m_1 must equal 1. This can be seen by first noting that the density, electric field, and potential do not depend on m_1 . So, from the potential (equation (91)) evaluated at the sheath edge and the realization that $\gamma_m = I_a/I_c$ (from equation (124)) at the sheath edge it is possible to obtain A_n . One can then solve equation (88) for A_n . By comparing the resulting equations it is evident that m_1 equals one. This implies equations (77) and (87) become (when $r_c \leq r \leq r_m$):

$$\vec{v}(r) = \frac{e|I_c|}{2\pi m_0 c^2 \epsilon_0 A_n} \tanh(A_n \ln(r/r_c)) \hat{z} \quad (89)$$

$$\vec{j}(r) = -\frac{A_n |I_c|}{2\pi r^2} \sinh(A_n \ln(r/r_c)) \hat{z} \quad (90)$$

From (78) thru (81) in the region $r_c \leq r \leq r_m$ after algebra

one obtains:

$$\varphi(r) = \frac{m_0 c^2}{e} (\cosh(A_n \ln(r/r_c)) - 1) \quad , \quad (91)$$

$$\vec{E}(r) = - \frac{m_0 c^2}{e} \frac{A_n}{r} \sinh(A_n \ln(r/r_c)) \hat{r} \quad , \quad (92)$$

$$\vec{A}(r) = \frac{\mu_0 |I_c|}{2\pi A_n} \sinh(A_n \ln(r/r_c)) \hat{z} \quad , \quad (93)$$

and

$$\vec{B}(r) = - \frac{\mu_0 |I_c|}{2\pi r} \cosh(A_n \ln(r/r_c)) \hat{\theta} \quad . \quad (94)$$

In the region $r_m \leq r \leq r_a$ the following relations apply:

$$\varphi(r) = \frac{m_0 c^2}{e} \left[A_n \ln(r/r_m) \left[\frac{I_a^2 - I_c^2}{I_c^2} \right]^{1/2} + \frac{I_a - I_c}{I_c} \right] \quad , \quad (95)$$

$$\vec{E}(r) = - \frac{m_0 c^2}{e r} A_n \sinh(A_n \ln(r_m/r_c)) \quad , \quad (96)$$

$$\vec{A}(r) = \frac{\mu_0}{2\pi} \left(|I_a| \ln(r/r_m) + \frac{|I_c|}{A_n} \sinh(A_n \ln(r_m/r_c)) \right) \quad , \quad (97)$$

$$\vec{B}(r) = - \frac{\mu_0}{2\pi r} |I_a| \hat{\theta} \quad , \quad (98)$$

and

$$\rho(r) = \vec{v}(r) = \vec{j}(r) = 0 \quad , \quad (99)$$

where from (88) and (94) the constant A_n is

$$A_n = \frac{1}{\ln(r_m/r_c)} \sinh^{-1} \left[\frac{I_a^2 - I_c^2}{I_c^2} \right]^{1/2} \quad .$$

$$= \frac{\cosh^{-1}(I_a/I_c)}{\ln(r_m/r_c)} \quad (100)$$

To determine the position of the electron sheath edge (r_m), equation (100) is substituted into (95) and evaluated at the anode where $\varphi(r_a) =$ the applied voltage (V_a). The following is obtained:

$$r_m = (r_a r_c^\eta)^{\frac{1}{1+\eta}} \quad (101)$$

where

$$\eta = \frac{1}{\cosh^{-1}(I_a/I_c)} \left[\frac{e |I_c| V_a}{m_0 c^2 (I_a^2 - I_c^2)^{1/2}} - \left[\frac{I_a - I_c}{I_a + I_c} \right]^{1/2} \right] \quad (102)$$

In addition, for $\vec{E} = -\vec{v} \times \vec{B}$ to hold (equation (84)):

$$I_c = - \frac{2\pi m_0 c^2}{\ln(r_m/r_c)} \left[\frac{\epsilon_0}{\mu_0} \right]^{1/2} \cosh^{-1}(I_a/I_c) \quad (103)$$

If one carefully compares the equations in this section to those in section 2.4, it can be seen that the formulation and source of the constants is different but the functional forms are the same. If one compares the flow quantities predicted by these two independent formulations it becomes apparent that they are predicting the same flow quantities given the same inputs. This is done for the potentials,

fields, density, momentum and energy profiles in figures 7 thru 11. In the figures, BRI TH corresponds to Creedon's solution and BRIN TH corresponds to this work's independent derivation. Also in figures 7 thru 11 are the constant density (RHO TH) solution (derived in 3.3.2) results in which the anode and cathode currents along with the total charge, are the same as the Brillouin flow case. It is clear from the figures that the two independent Brillouin flow solutions overlay each other. The contrast between the constant density flow solution and the Brillouin flow is apparent in these figures.

The Brillouin and constant density flow solutions shown in figures 7 thru 11 are characterized by the following:

$$I_a = - 7.18 \times 10^4 \text{ Amperes}$$

$$I_c = - 4.116 \times 10^4 \text{ Amperes}$$

$$r_a = .05 \text{ Meters}$$

$$r_c = .025 \text{ Meters}$$

The Brillouin flow cases have a potential difference of $V_a = 2 \times 10^6$ volts between the anode and cathode (figure 8a).

However, the constant density solution allows a lower potential for the same currents (figure 8a) in this case.

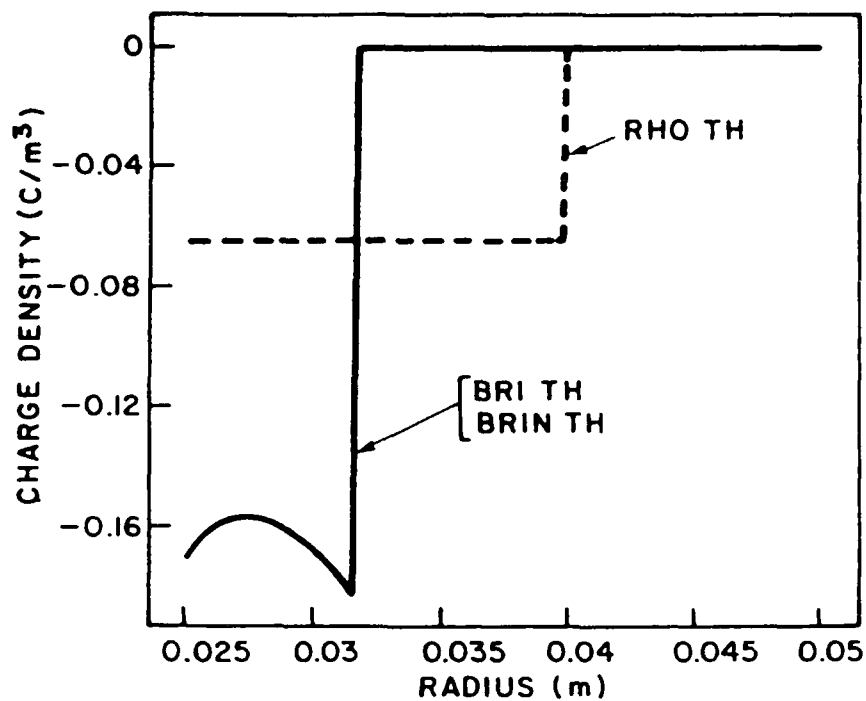
Eventhough the constant density and Brillouin flow solutions have differing potentials applied across their respective anode/cathode gaps, the anode electric fields $E(r_a)$ are the same:

$$\vec{E}(r_a) = - \frac{c\mu_0(I_a^2 - I_c^2)^{1/2}}{2\pi r_a} \hat{r} \quad (104)$$

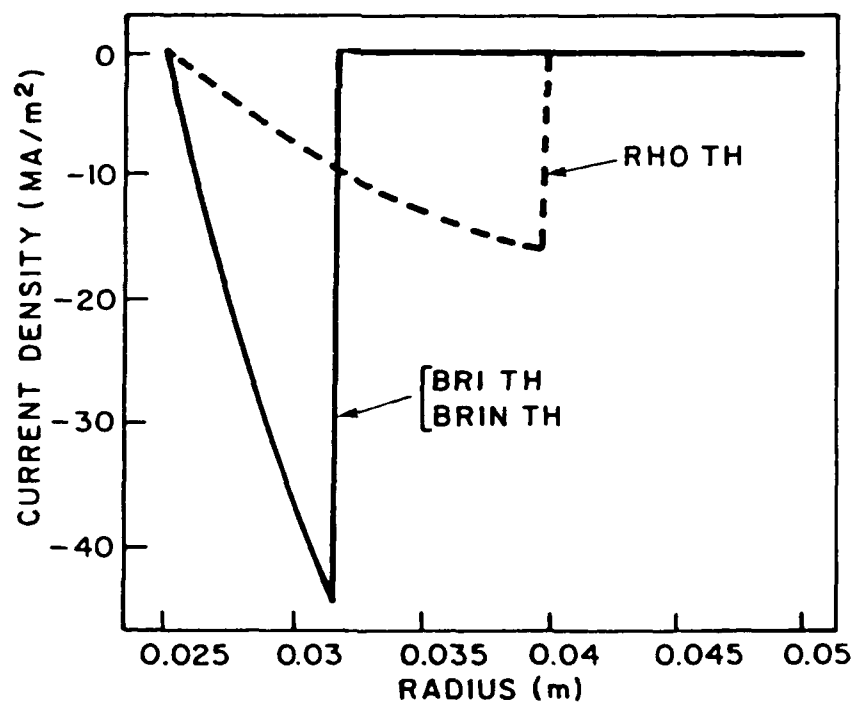
This relation is in accordance with the laminar ($P_m = 0$) form of equation (50). Since the electric fields are the same at the anode and the fields of the Brillouin solution are larger close to the cathode (figure 9a), the potential for the constant density flow is lower (figure 8a) than the Brillouin flow for this case.

Before proceeding to the next section, it is worth discussing figures 10b, 11a and 11b. Figure 10b gives \vec{E} for a Brillouin flow field and then compares it to $-\vec{v} \times \vec{B}$. These overlap up to the sheath edge where \vec{v} goes to zero. This verifies that the flow is laminar. This test was performed and passed on all the laminar flow solutions.

Figure 11a gives $\gamma^2 - p_{cz}^2$ curves for the constant density and Brillouin flow cases. $\gamma^2 - p_{cz}^2$ must equal 1, as long as one is within the electron sheath and is considering a laminar flow. This relation is seen to be satisfied in figure 11a. Figure 11b graphs the total energy vs the canonical momentum for the constant density and Brillouin flows. The constant density flows have a profile in the fourth quadrant. The two Brillouin flows have canonical momentums and energies equal to zero across the flow. The reason the canonical momentum and total energy are not exactly zero for the Brillouin flow solution obtained in this section is because insufficient iterations (three iterations) were taken in evaluating equations (101)-(103). The more iterations taken the closer the canonical momentum and total energy are to zero.



a. Charge density profile.



b. Current density profile.

Figure 7. Density Profiles for the Constant Density and Brillouin Flow Solutions.

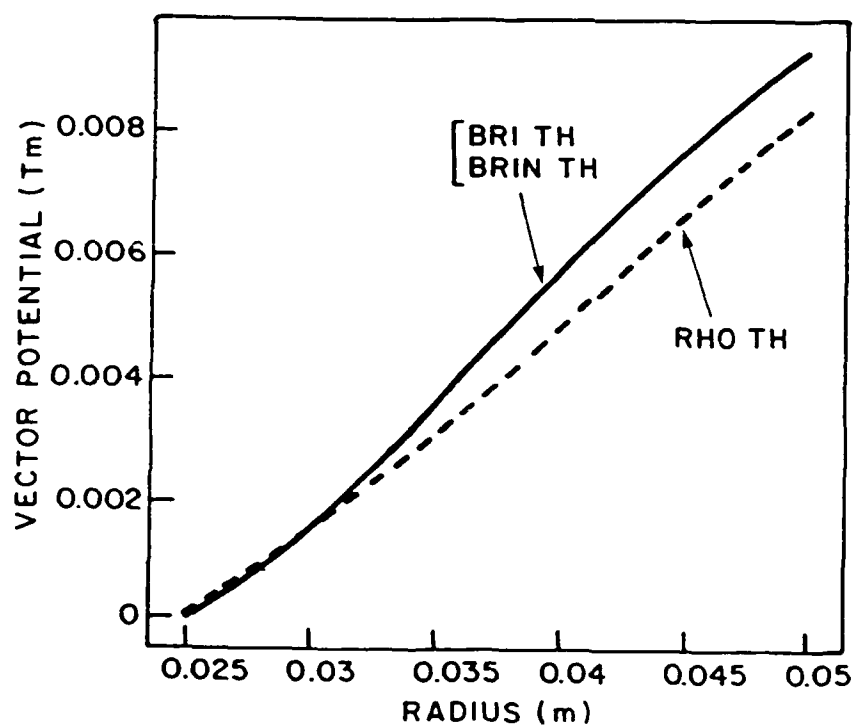
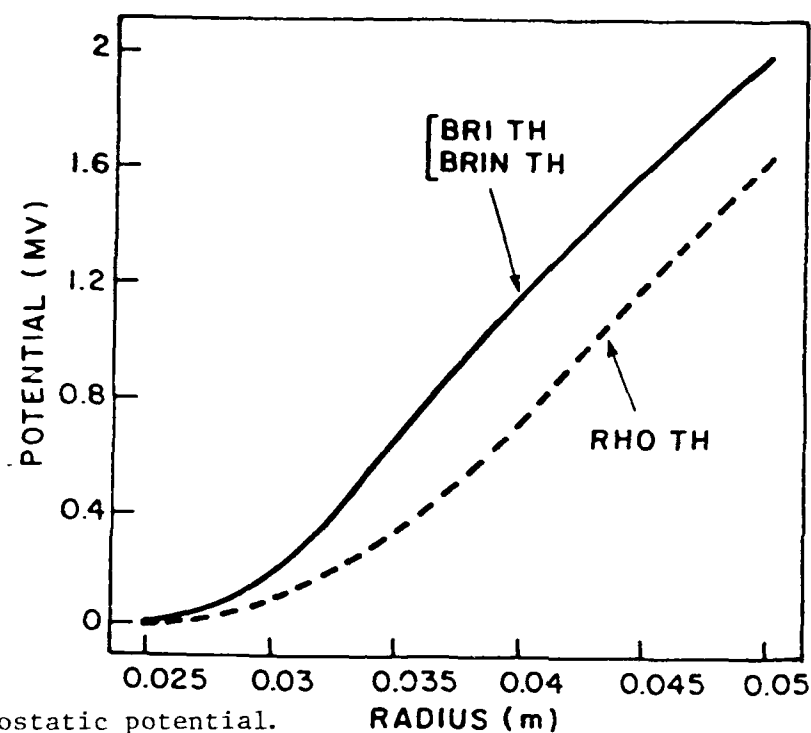
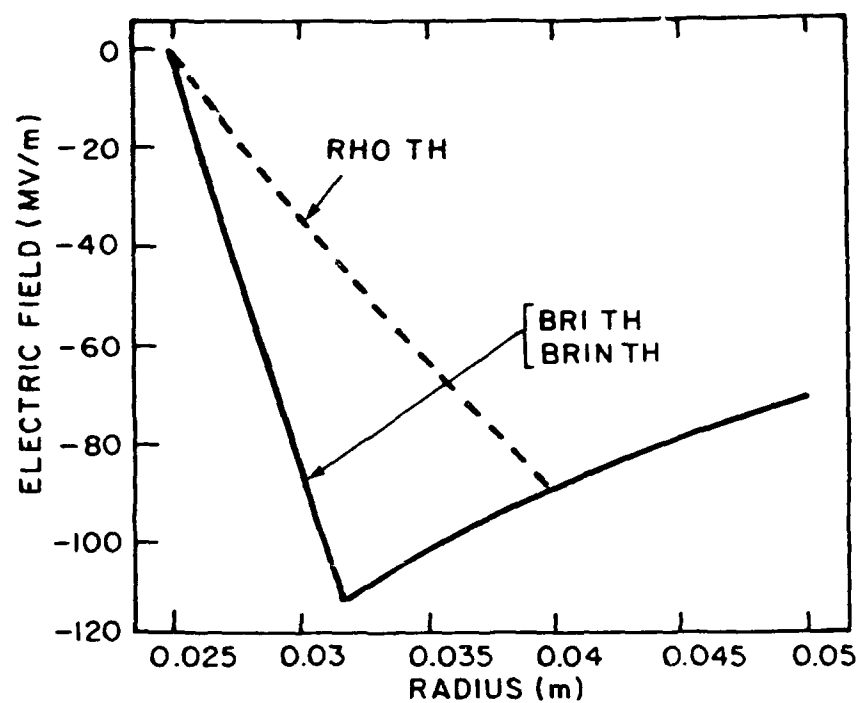
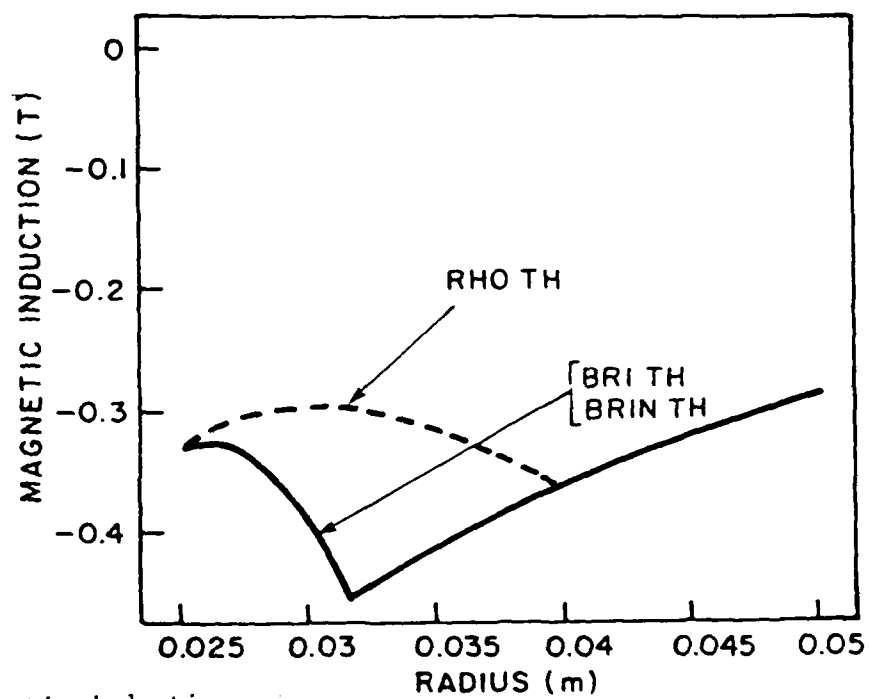


Figure 8. Potential Profiles for the Constant Density and Brillouin Flow Solutions.

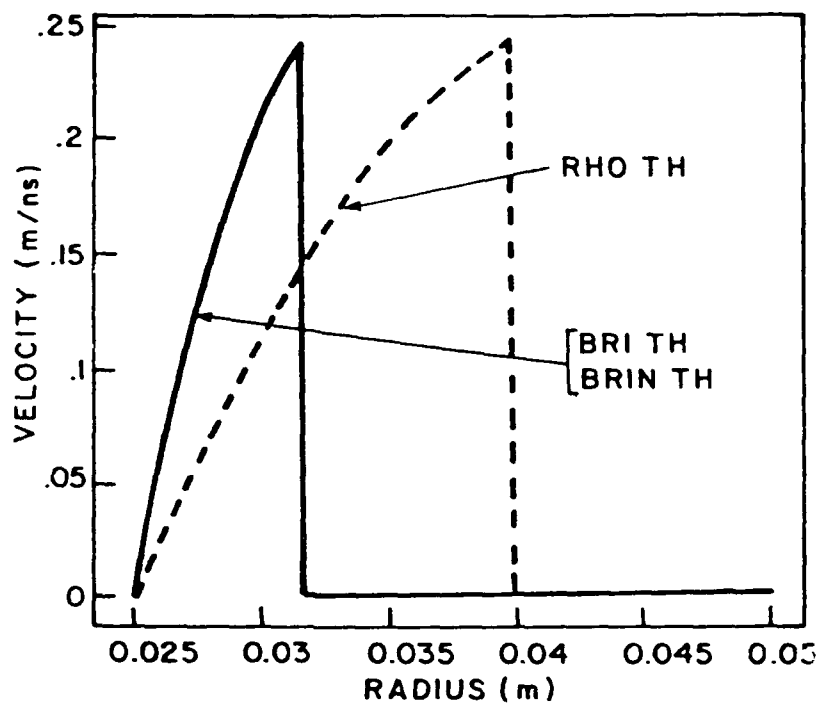


a. Electric field.

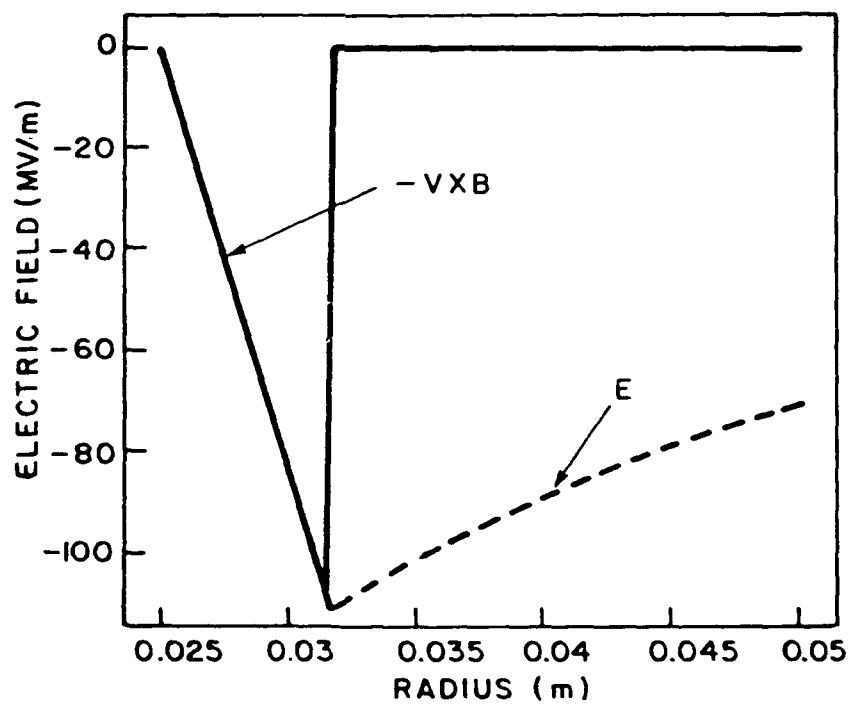


b. Magnetic induction.

Figure 9. Field Profiles for the Constant Density and Brillouin Flow Solutions.

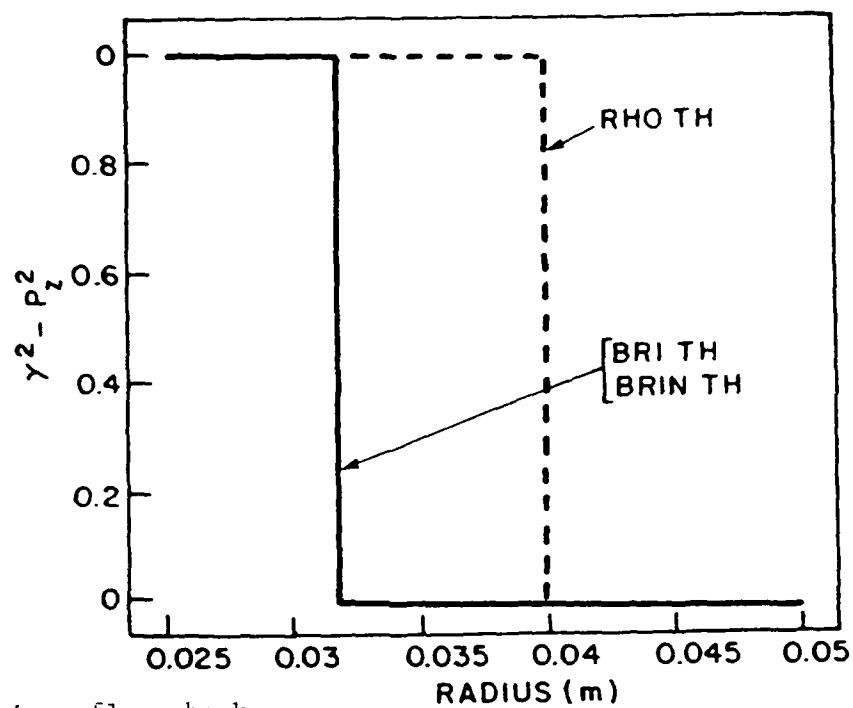


a. Azial velocity.

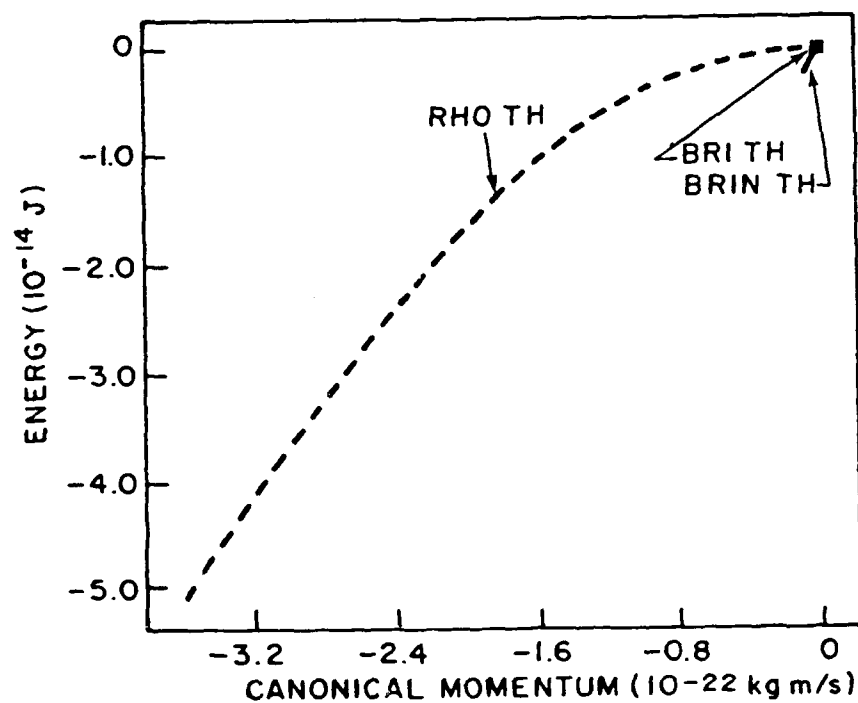


b. Laminar flow check.

Figure 10. Azial Velocity and Laminar Flow Check for the Constant Density and Brillouin Flow Solutions.



a. Laminar flow check.



b. Total energy vs canonical momentum.

Figure 11. Laminar Flow Check and Total Energy Vs Canonical Momentum Profiles.

3.3.2 Constant Density Flow

In various MASK calculations of short MITLs, it has been noted that the density as a function of radius is relatively constant out to the sheath edge, where it drops to zero. For this reason (and the fact that the integrals are simpler to evaluate), a self-consistent MITL flow for a constant density profile is given below. Substituting a constant density profile into relations (75)-(84) and evaluating between the limits $r_c \leq r \leq r_m$ results in:

$$f(r) = \frac{r^2 - r_c^2}{r_m^2 - r_c^2} \quad , \quad (105)$$

$$\vec{v}(r) = \frac{-I_c}{\pi \rho (r^2 - r_c^2)} \left[\left[1 + \left(\frac{I_a^2 - I_c^2}{I_c^2} \right) f^2(r) \right]^{1/2} - \left[1 + \left(\frac{I_a^2 - I_c^2}{I_c^2} \right) f^2(r) \right]^{-1/2} \right] \hat{z} \quad , \quad (106)$$

$$\vec{j}(r) = -|\rho| \vec{v}(r) \quad , \quad (107)$$

$$\varphi(r) = \frac{|\rho|}{4\epsilon_0} (r^2 - r_c^2 - 2r_c^2 \ln(r/r_c)) \quad , \quad (108)$$

$$\vec{E}(r) = \frac{-|\rho| (r^2 - r_c^2)}{2\epsilon_0 r} \hat{r} \quad , \quad (109)$$

$$\vec{A}(r) = -\frac{\mu_0 I_c}{2\pi} K(r) \hat{z} \quad , \quad (110)$$

and

$$\vec{B}(r) = \frac{\mu_0 I_c}{2\pi r} \left[\left[\frac{I_a^2 - I_c^2}{I_c^2} \right] \left[\frac{r^2 - r_c^2}{r_m^2 - r_c^2} \right]^2 + 1 \right]^{1/2} \hat{\theta} \quad (111)$$

where

$$K(r) = \frac{1}{2} \left[(ax^2 + bx + c_1)^{1/2} + \frac{b}{2a^{1/2}} \ln(2a^{1/2}(ax^2 + bx + c_1)^{1/2} + 2ax + b) - c_1^{1/2} \ln \left[\frac{2c_1^{1/2}(ax^2 + bx + c_1)^{1/2} + bx + 2c_1}{x} \right] \right] \frac{2r^2}{2r_c^2} \quad (112)$$

$$a = c_3/4, \quad b = -c_3 r_c, \quad c_1 = c_3 r_c^4 + 1 \quad (113)$$

$$c_3 = \frac{I_a^2 - I_c^2}{I_c^2} \frac{1}{(r_m^2 - r_c^2)^2} \quad (114)$$

Evaluating these same quantities from the sheath edge to the anode ($r_m \leq r \leq r_a$) results in:

$$\varphi(r) = \frac{|\rho|}{4\epsilon_0} \left[\left[r_m^2 - r_c^2 \right] \left[2\ln(r/r_m) + 1 \right] - 2r_c^2 \ln(r_m/r_c) \right] \quad (115)$$

$$\vec{E}(r) = - \frac{|\rho|}{2\epsilon_0 r} (r_m^2 - r_c^2) \hat{r} \quad (116)$$

$$\vec{A}(r) = \left[- \frac{\mu_0 I_c}{2\pi} \ln(r/r_m) + c_4 \right] \quad (117)$$

$$\vec{B}(r) = \frac{\mu_0 I_a}{2\pi r} \hat{\theta} \quad (118)$$

and

$$\vec{v}(r) = \rho(r) = \vec{j}(r) = 0 \quad (119)$$

$$\text{where } c_4 = - \frac{\mu_o I_c}{2\pi} K(r) \Big|_{2r_c^2}^{2r_m^2} . \quad (120)$$

Thus far, all that is known about the density profile is that it is constant out to the sheath edge where it drops to zero. The magnitude of the electron density and the sheath edge radius can be self-consistently determined from the theory.

The magnitude of the electron density can be obtained from equations (104) and (116). It is given by:

$$|\rho| = \frac{(I_a^2 - I_c^2)^{1/2}}{c\pi(r_m^2 - r_c^2)} . \quad (121)$$

The sheath edge radius (r_m) is obtained by evaluating (115) at the anode where the anode voltage (V_a) is given. The resulting expression is:

$$\left[\frac{r_m}{r_c} \right] \left[\frac{1}{1 - (r_c/r_m)^2} \right] = \frac{r_a}{r_c} \exp \left[.5 - \frac{2\pi\epsilon_o c V_a}{(I_a^2 - I_c^2)^{1/2}} \right] . \quad (122)$$

So, r_m is obtained iteratively given the anode and cathode currents, along with the anode and cathode radii, and the voltage difference across the diode. Once r_m is known all other quantities defined in equations (105)-(121) are given. In typical experiments r_a , r_c , I_a , and V_a are known. I_c is a little harder to obtain, but can be found using a magnetic

probe next to the cathode[34].

It is also interesting to note that $\gamma_m = I_a/I_c$ at the sheath edge. This can be seen by evaluating (106) at the sheath edge:

$$v(r_m) = \frac{c}{I_a} (I_a^2 - I_c^2)^{1/2} \quad (123)$$

Equation (123) gives the velocity of the electrons at the sheath edge, so the relativistic factor at r_m is

$$\gamma_m = \frac{1}{(1 - v^2(r_m)/c^2)^{1/2}} = \frac{I_a}{I_c} \quad (124)$$

Equation (124) also holds for the Brillouin laminar flow solution (see equation (62)). What this means is that even though the electron sheaths have differing electron density profiles and sheath edge radii(r_m), the electron velocity at the sheath edge is the same given the same ratio of I_a/I_c .

Since $\gamma_m = I_a/I_c$ at the sheath edge for two very different density profiles, perhaps $\gamma_m = I_a/I_c$ at the sheath edge for all laminar flow solutions. This is in fact true and is easily proved using the general theory of laminar flows. First one needs to note that $f(r_m) = 1$ at the sheath edge (see equation (75)). In examining equation (76) one needs to realize that the integral $2\pi \int_{r_c}^{r_m} \rho(r) r dr$ is simply the total charge (q) in the sheath per unit length in z . From equation (50) with $P_m = 0$ and Gauss's law the total electron sheath space charge per unit length is given by:

$$q = \frac{(I_a^2 - I_c^2)^{1/2}}{c} \quad (125)$$

Substituting $f(r_m) = 1$ and equation (125) into equation (76) results in:

$$v(r_m) = \frac{c}{I_a} (I_a^2 - I_c^2)^{1/2} \quad (123)$$

which when substituted into the relativistic factor evaluated at the sheath edge results in:

$$\gamma_m = I_a / I_c \quad (124)$$

So, for all laminar flows $\gamma_m = I_a / I_c$ at the sheath edge!

3.4 Comparison of Constant Density and Brillouin Flow

Theory Predictions to MASK Simulations

In many short cylindrical MITL simulations, non-uniformities in the electric fields (usually E_z) result in laminar flows with density profiles that are nearly constant. In the following, such MASK simulations are compared against the constant density and Brillouin flow theories. The magnetic fields for three cases are presented: 1) strongly insulated — little space charge flow (figure 12), 2) fairly well insulated — more space charge flow (figure 13), and 3) insulation breaking down — greatest amount of space charge flow (figure 14).

In figure 12, the theoretical results essentially lie on top of the MASK results. The space charge current flow ($I_e = I_a - I_c$) is only 11% of the cathode current. The reason the Brillouin and constant density solutions match so closely is because there is very little space charge current flow. The magnetic field is primarily due to the cathode

MASK CALCULATION M458 vs THEORY

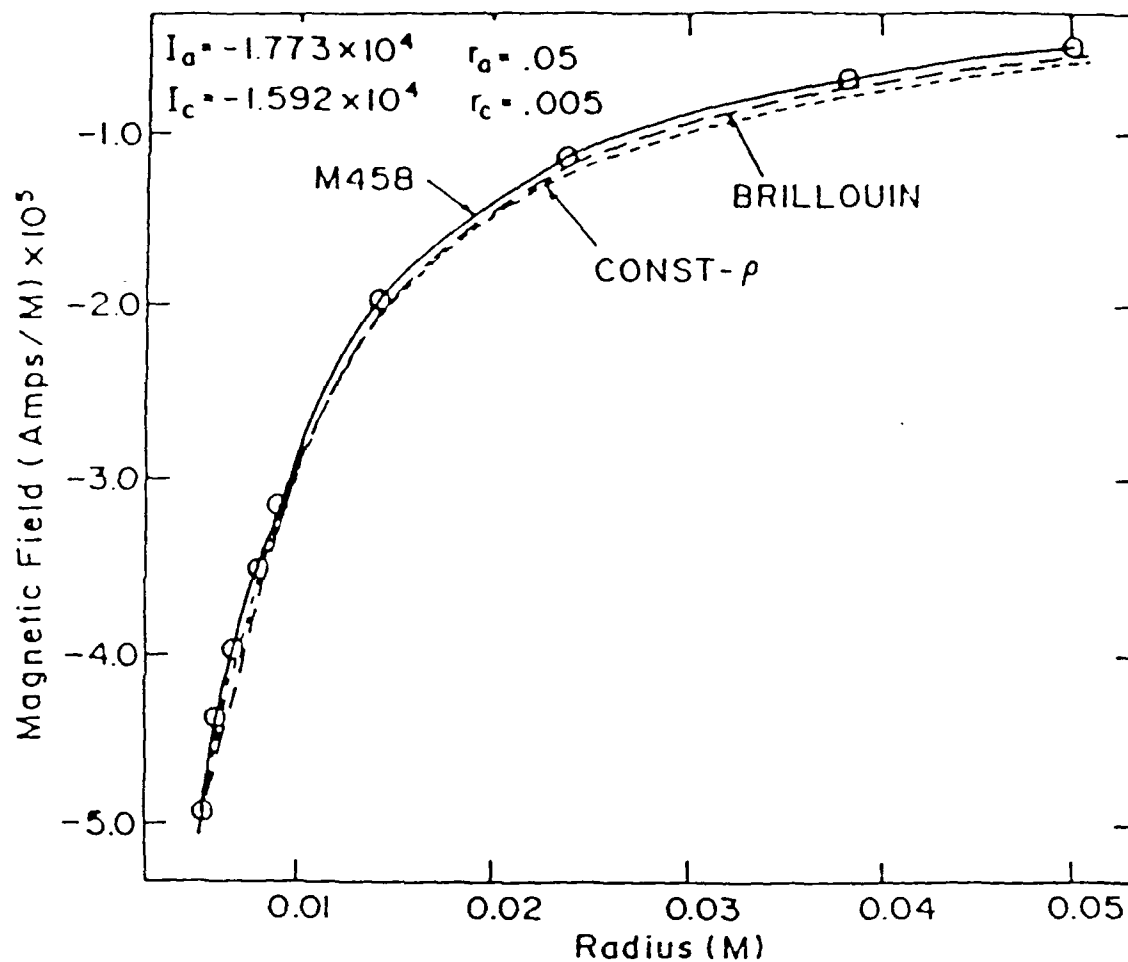


Figure 12. Theory Vs. MASK Simulation for the Case of Insignificant Space Charge Flow.

current. The space charge current distribution, although radically different between the two cases, is so narrow in \hat{r} that the total current (I_a) is included at a radius of .007 meters. By Ampere's law the magnetic fields must match from that point on. Therefore, the fields essentially lie on top of each other from .007 meters to the anode (at .05 meters) as expected.

However, in figure 13, it is clear that the constant density result is more accurately matching the simulation results than the Brillouin flow theory. It is also important to note that the Brillouin flow solution is not satisfying Ampere's law at the cathode or anode. The reason for this is that the Brillouin flow solution is valid for only certain anode and cathode currents given a voltage across the diode. These currents are given by equations (61) and (62) or (101)-(103), and (124). The values of the anode and cathode currents in figure 13 come from MASK and do not satisfy the Brillouin flow restrictions. A nice feature of the constant density theory is that it will produce a self consistent flow solution irregardless of the anode and cathode currents given.

Figure 14 presents the magnetic field for the case of a semi-trapped MITL flow. Once again, the constant density theory corresponds more closely to the MASK calculation than the Brillouin flow solution. The match between the constant density theory and MASK in figure 14 is not as good as it is in figure 13 because the density profile in 14 is less

MASK CALCULATION M420 vs THEORY

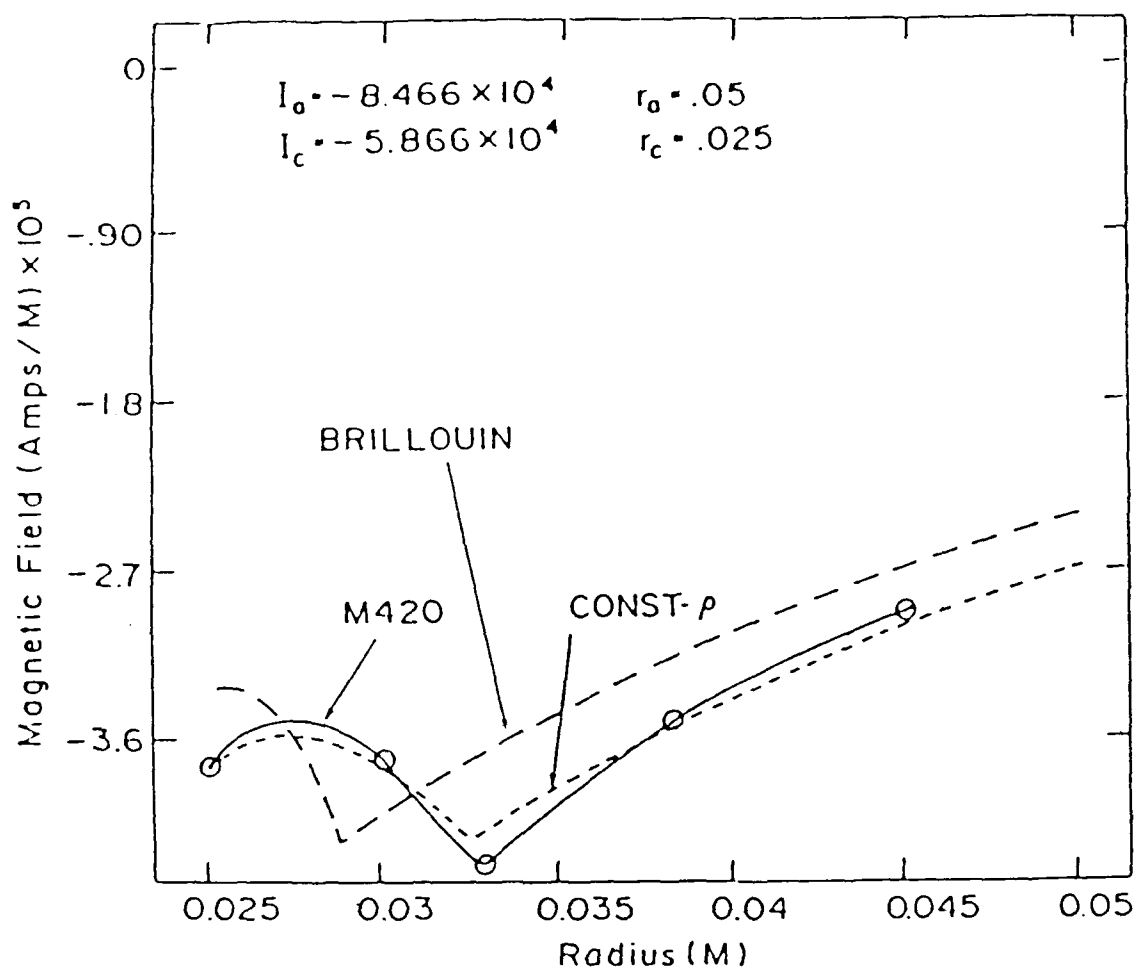


Figure 13. Theory Vs. MASK Simulation for the Case of a Fairly Significant Space Charge Flow.

MASK CALCULATION M424 vs THEORY

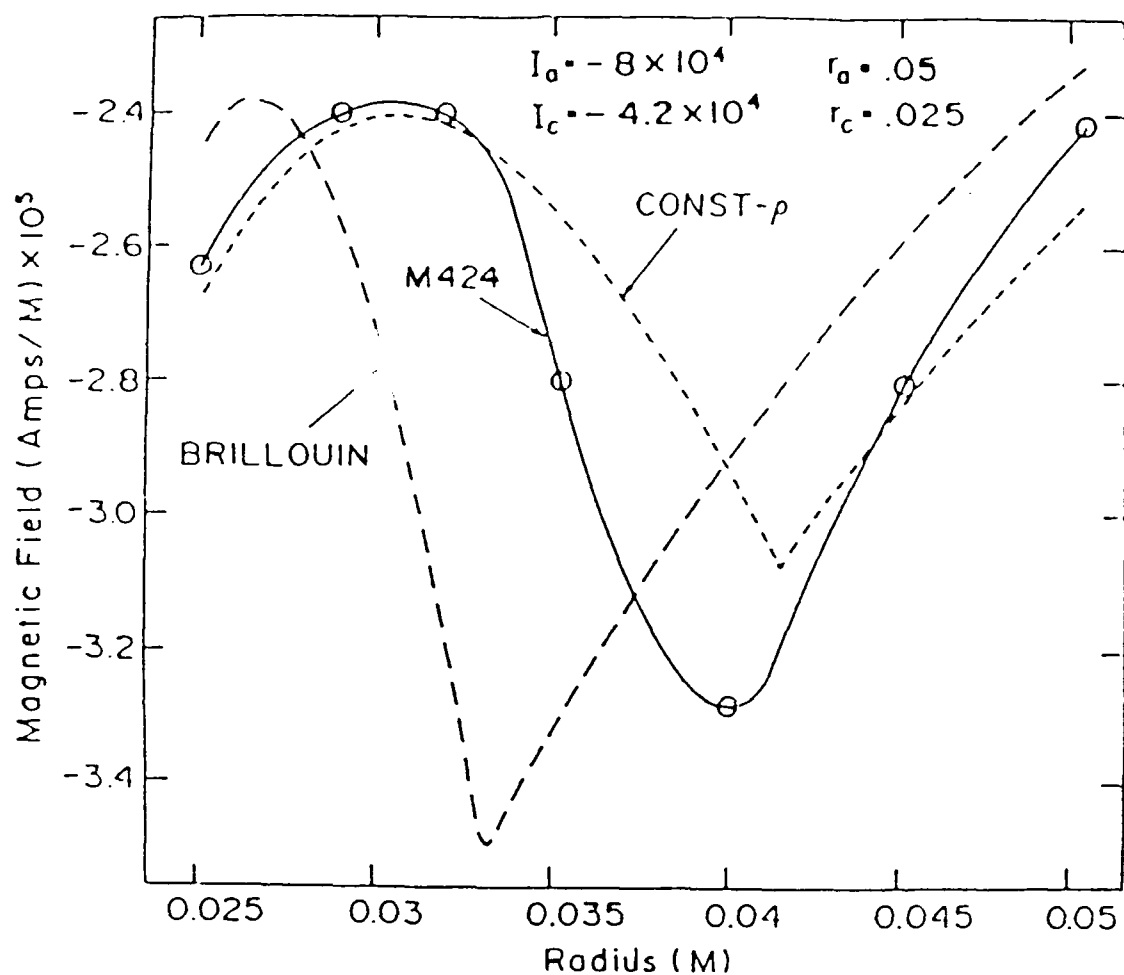


Figure 14. Theory Vs. MASK Simulation for the Case of a Large Space Charge Flow.

constant than in 13. One should also note that the Brillouin flow solution is once again not satisfying Ampere's law. If it were, it would match the constant density solution at the anode and the cathode. The reason they should match is because the same I_a and I_c were used in both models. The reason the constant density solution does not exactly match MASK at the anode and cathode in this case is because the MASK magnetic field profile seen here corresponds to one slice across the flow ($z=\text{constant}$). For the theoretical treatments the cathode and anode currents were obtained by averaging the values obtained from three slices.

This concludes the derivation and verification of the general theory of laminar flows. In the next chapter, the general theory will be used to derive an electron flow solution downstream of a PEOS. However, before this is done, the history and workings of a PEOS will be given.

CHAPTER 4

PLASMA EROSION OPENING SWITCH

The plasma erosion opening switch (PEOS) has been used as a fast output switch on pulsed power generators. It can conduct mega-Ampere levels of current for 10's of nanoseconds before switching the current to a load in less than 10 nanoseconds. The PEOS can be used on tera-Watt level systems for inductive storage, pulse compression, rise time sharpening, and power multiplication by pulse compression [27,31]. Indeed, it has many applications, one of which was mentioned in the introduction to this dissertation — inertial confinement fusion.

In cylindrical geometries, the switch typically conducts current through a plasma injected through a screen in the outer anode onto a central cathode (see figure 15). When the ion current through the switch exceeds the ion flow supplied by the injected plasma fill, the plasma erodes away from the cathode and the switch begins to open [56]. As it opens, there is initially a significantly higher impedance across the downstream power feed and load than across the switch. This mismatch causes electrons to continue streaming from the cathode to the eroding PEOS making them unavailable to power the load. As the switch continues to open (the injected plasma continues eroding away from the cathode) the impedance mismatch decreases and magnetic

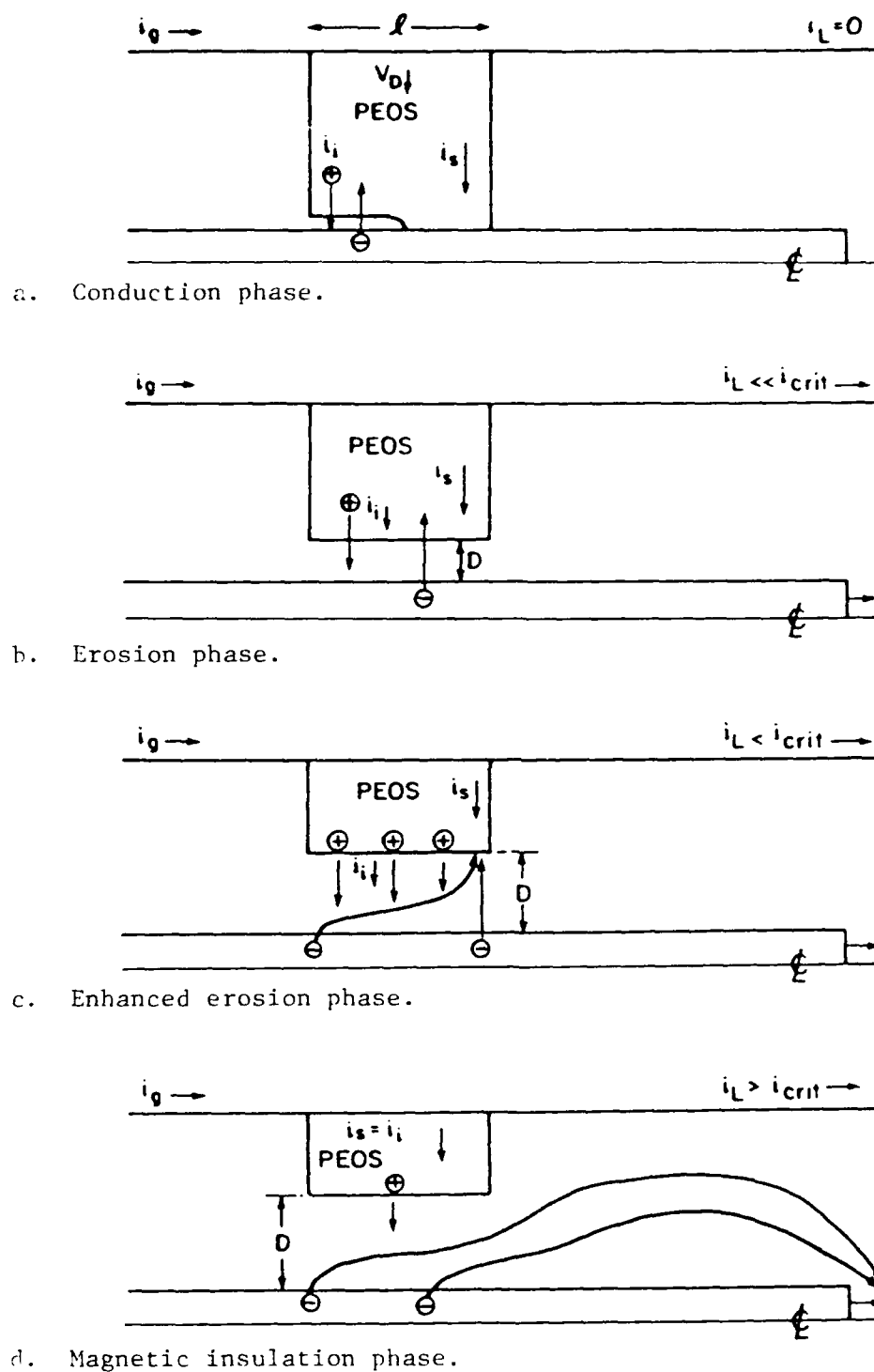


Figure 15. The Four Phases of a PEOS Opening.

insulation insures power is not lost across the switch itself.

However, between the switch and load, electrons sometimes continue to shunt power from the load as a complex function of the perturbing PEOS plasma, applied voltage, currents, and line and load impedances. This potential loss of magnetically insulated electron flow is a major concern, because it not only represents a power loss, but it can also cause the PEOS to not open completely (or close prematurely). Avoiding the regimes in which losses occur embodies Chapter 5 and modeling the electron flow in the loss free region embodies part of this chapter.

Chapter 4 begins with a historical summary of PEOS research. It also reviews the basic physics and phases of an opening PEOS. Then, the electron flow downstream of a PEOS during the opening phase is studied. In regimes of laminar like flows downstream of the PEOS, the general theory (developed in Chapter 3) is used to derive a laminar flow solution.

4.1 Historical Summary and Background Physics

This is a historical summary of PEOS research done in the United States [27]. Other nations such as the Soviet Union [26], Japan [35], West Germany [36], etc. are also involved and contributing in this area, but to a lesser extent at present. A PEOS was first used in 1977 by Mendel et. al. of Sandia for prepulse suppression on the Proto I Generator [37]. In 1981, Stringfield, et. al. [38] used a

PEOS in conjunction with experiments done on the Python Generator at Physics International Company. Also in 1981, the Naval Research Laboratory(NRL) became involved with the PEOS. Collaboratively with C. W. Mendel of Sandia, they were successful in suppressing the prepulse and preventing early gap closure on experiments performed on the Aurora Generator at Harry Diamond Laboratories [39]. The NRL group realized at this point that a PEOS could possibly be used in an inductive storage system to multiply the pulsed power by compressing the pulse in time.

This revolutionary new use of the PEOS was demonstrated by Meger, et. al. of NRL in 1983 [40]. Experiments were performed on Gamble I of NRL that showed inductive energy storage, pulse compression and power multiplication. Gamble I, running with a PEOS, had peak powers greater than the traditional maximum peak powers predicted using matched loads. This exciting result led to PEOSs being installed on the Super Mite Generator at Sandia [41] and on PBFAII. Also, high current experiments were performed on the Black Jack 5 Generator at Maxwell Laboratories [42]. All these efforts have confirmed the validity of this new use for the PEOS.

In addition, PEOS work is now being done by NRL in the area of long conduction times (.5 to 1. microsecond) [43]. In these efforts, the switch conducts current for times on the order of a microsecond before switching the current to a load in about 100 nanoseconds. It has also been noted that

in pinch-reflex ion diode experiments performed on Gamble II, ion beam brightness is substantially increased when run with a PEOS. This is attributed to faster ion turn-on [44]. There are many other PEOS applications. One reported on recently at the 1987 Plasma Science IEEE Meeting is the use of PEOSs for repetitively pulsed power applications [45]. In order to more clearly understand the possible applications and limitations of the PEOS, one needs to understand the basic physics and phases of opening.

The phases of PEOS opening are shown in figure 15. These phases and the physics involved are presented in the remainder of this section. In figure 15, one notes four phases of PEOS opening which in accordance to NRL are [46]: a) the conduction phase, b) the erosion phase, c) the enhanced erosion phase, and d) the magnetic insulation phase. A brief summary of each phase and the transition condition from phase to phase is given next.

During the conduction phase the resistance across the plasma switch is approximately zero. A thin sheath forms between the cathode and plasma. Ion current (i_i) from the plasma and electron current (i_{e1}) from the cathode cross the sheath in a bi-polar space charge limited fashion. This is given by:

$$i_i/i_{e1} = (zm_e/m_i)^{1/2} \quad (125)$$

where m_i is the ion mass and m_e is the electron mass. z is the ion charge state. The electrons that are emitted from the cathode (in a SCL fashion) are accelerated from the

cathode towards the bottom of the PEOS. These electrons enter the PEOS plasma with a large amount of kinetic energy. This kinetic energy is transformed into electromagnetic waves that cause a large number of anomalous collisions or mixing. The end result of such mixing could be anomalous magnetic diffusion and wide current channels. Also, the current would be predominately radial in nature. When anomalous collisions are not taken into account fluid code simulations in 1 and 2 dimensions [47], PIC code simulations [48, 49] and theoretical treatments [50] show non-radial narrow current channels. However, experiments done at NRL clearly show wide current channels and predominantly radial current paths [51]. When anomalous collisions are taken into account — with a collision frequency on the order of the plasma electron frequency — PIC [52] and fluid [53,54] code simulations match the experiments done at NRL. An instability responsible for such anomalous collisions has been suggested and analyzed by Kulsrud, Ottinger and Grossman [55].

In general $m_i \gg m_e$, so that the current crossing the switch ($i_s = i_{e1} - i_i$) is approximately equal to i_{e1} (by (125)). When i_s becomes so large that i_i is greater than that supplied by the injected plasma, the conduction phase ends and the erosion phase begins. This happens when [56]:

$$i_i \cong \left[\frac{m_e z}{m_p A} \right]^{1/2} i_s > 2\pi l r_c n_p e z v_d \quad , \quad (126)$$

where v_d is the plasma drift velocity, n_p is the plasma number density, l is the axial length of the plasma and A is

the atomic number.

When more ions are pulled off the bottom plasma surface than the plasma drift can resupply, the plasma erodes away from the cathode. This is shown in figure 15b. The growth of the gap (D) between the plasma and cathode (figure 15b) is given by [56]:

$$\frac{dD}{dt} = \frac{i_i - n_p z e v_d 2\pi r_c l}{n_p z e 2\pi r_c l} \quad (127)$$

As the gap grows, current begins flowing through the load. This leads to partial magnetic insulation of the space charge electron flow. The magnetically trapped electrons electrostatically attract ions enhancing the plasma erosion. This is called the enhanced erosion phase in which the increased ion current is given by [56,57]:

$$i_i = i_e (2zm_e/m_i)^{1/2} (\gamma+1) l/D \quad (128)$$

As more current passes through the load, the magnetic insulation is increased. When the current through the load is so large that no ions reach the anode, the magnetic insulation phase begins. The minimum required insulating current for this as proposed by Ottinger, et. al. is [56]:

$$i_{crit} = 1.6 \times 8500 \frac{(\gamma^2 - 1)^{1/2}}{\ln(r_p/r_c)} \quad (129)$$

This is the standard relation for the critical current multiplied by a factor of 1.6. The factor is obtained in

the analysis of a couple calculations done in the 2MV regime [58] in conjunction with the experimentally measured impedance behaviour of a pinch reflex diode by NRL. A more in depth numerical and theoretical analysis is performed in Chapter 5 to more accurately determine I_{crit} .

4.2 Magnetic Insulation Phase Electron Flow

When the current through the load exceeds the critical current (Chapter 5), the electron flow is insulated away from the anode and the magnetic insulation phase is underway. Even though the flow is insulated, it can be quite chaotic downstream of the PEOS. In such a situation there are various instabilities [11,22,32,59-63] that can complicate the understanding of the electron dynamics. However, in the MASK calculations done in this research they played a negligible role. This could be because the length of the MITL between the switch and load is so short that the instabilities do not have a chance to develop.

An interesting aspect of having a short MITL between the switch and load, is that the magnetic insulation of the system can be made to occur on a faster scale. This can be understood by considering an electromagnetic pulse propagating down an unperturbed MITL. At the pulse front, electrons flow directly from the cathode to the anode. Downstream of the pulse head, electrons are bent into orbits that are governed by the self-limited impedance of the line (figure 2a). This state continues until the pulse head strikes the load. If the impedance of the load verses the

impedance of the line as a function of voltage is less than the ratio given in figure 39, then an insulation wave will propagate from the load end of the system back down the line. This insulation wave causes an increased magnetic field that more tightly traps the electron space charge flow to the cathode (see figure 16). The longer the line or distance between the load and PEOS the longer it will take for this increased insulation of electron flow to take effect. If the load impedance changes as a function of time the effect on the PEOS will be retarded proportional to its distance from the load.

It is interesting to note that in PEOS experiments done at NRL, it has been found that minimizing the distance between the PEOS and load reduces current losses and results in more efficient switching [64]. This is probably attributable to reduced instabilities and quicker magnetic insulation in shorter systems.

Before one considers the instabilities of the insulated flow downstream of the PEOS, the fundamentals of the flow should be understood. In MASK simulations of a stationary PEOS, the fundamental properties of the flow have been examined. The PEOS perturbation launches the electron flow in a manner consistent with an $\vec{E} \times \vec{B}$ drift. The electron orbits are often laminar in nature. However, for well trapped magnetically insulated flows downstream of a PEOS, the laminar flow introduced by the perturbations can be overshadowed by the magnetic fields. When this happens, the

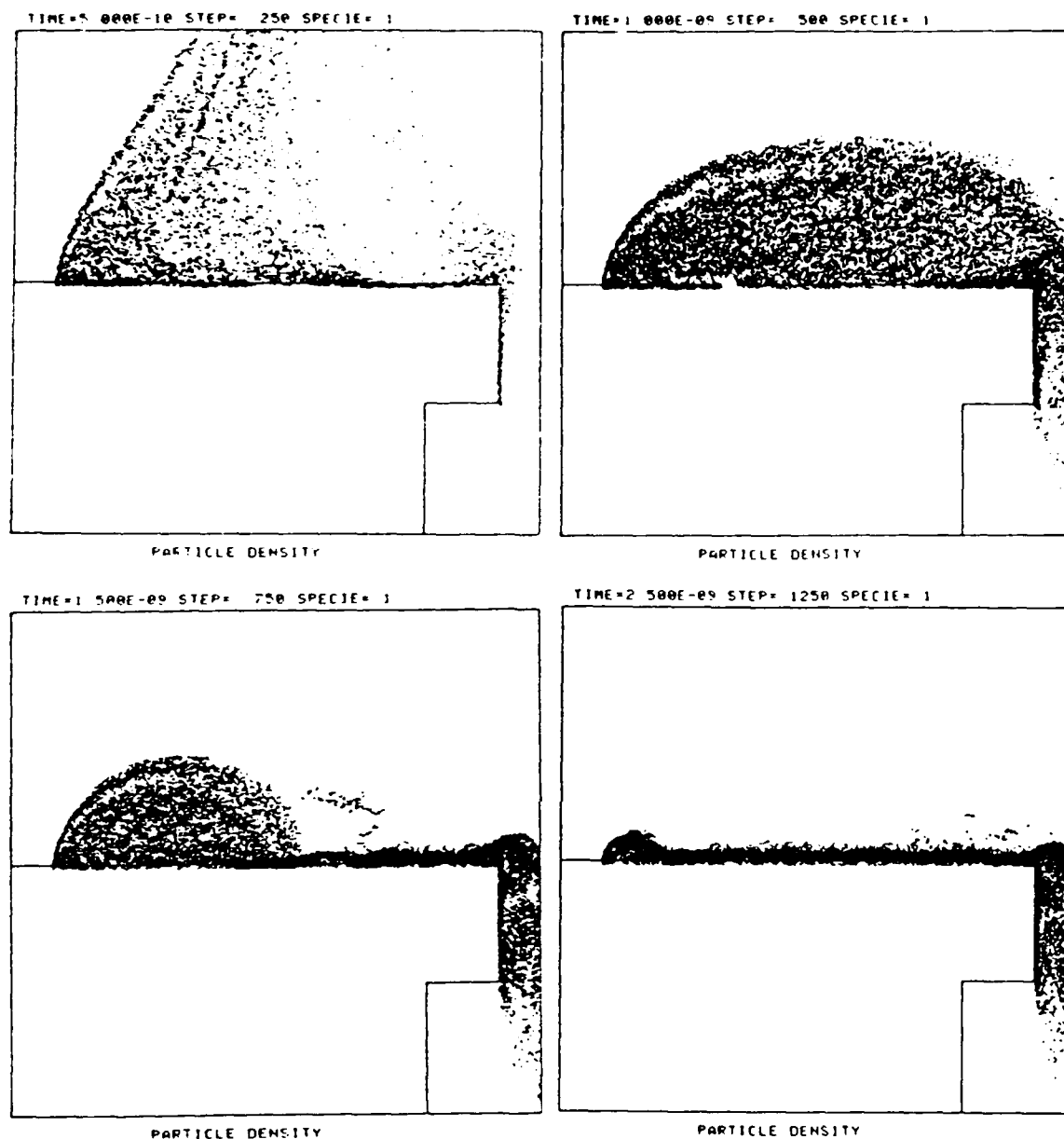


Figure 16. Insulation Wave in a Load-Limited Line.

The insulation wave propagates from the load end back up the line resulting in a more tightly trapped electron flow.

flow enters non-laminar electron orbits that are typically prolate or curtate. In this section, the launching mechanism and examples of laminar and non-laminar flows downstream of an abruptly varying structure (with and without ion emission) are presented.

4.2.1 Beam Launching

In MASK simulations, the PEOS often launches the electron flow (from the cathode and) into the cathode/anode gap. An example of this is shown in figure 17 which is a vector plot of the current densities for problem PN06 (Table C4 of Appendix C). In simulation PN06, the load is fairly large and results in a poorly trapped flow downstream of the PEOS.

In detailed analysis of various MASK simulations, it appears that the primary mechanism for launching the electrons is a component of the $\vec{E} \times \vec{B}$ drift in the positive radial direction. The $\vec{E} \times \vec{B}$ drift velocity is given by:

$$\vec{v}_e = \left(1 + \frac{r}{4} \nabla^2 \right) \frac{\vec{E} \times \vec{B}}{B^2} \quad (130)$$

Since $\vec{B} = -B(r)\hat{\theta}$, \vec{E} must have a significant component in \hat{z} for beam launching. Upstream of the structure (PEOS) there is a $-\hat{z}$ component of \vec{E} which suppresses launching; however, downstream of the PEOS \vec{E} has a $+\hat{z}$ component. One should also note that in going from a region of no space charge flow (i.e. an insulator) to one with space charge flow (see figure 1) there will also be a $+\hat{z}$ component of \vec{E} that will cause partial or complete beam launching. Complete beam launching refers to launched electron flows that completely

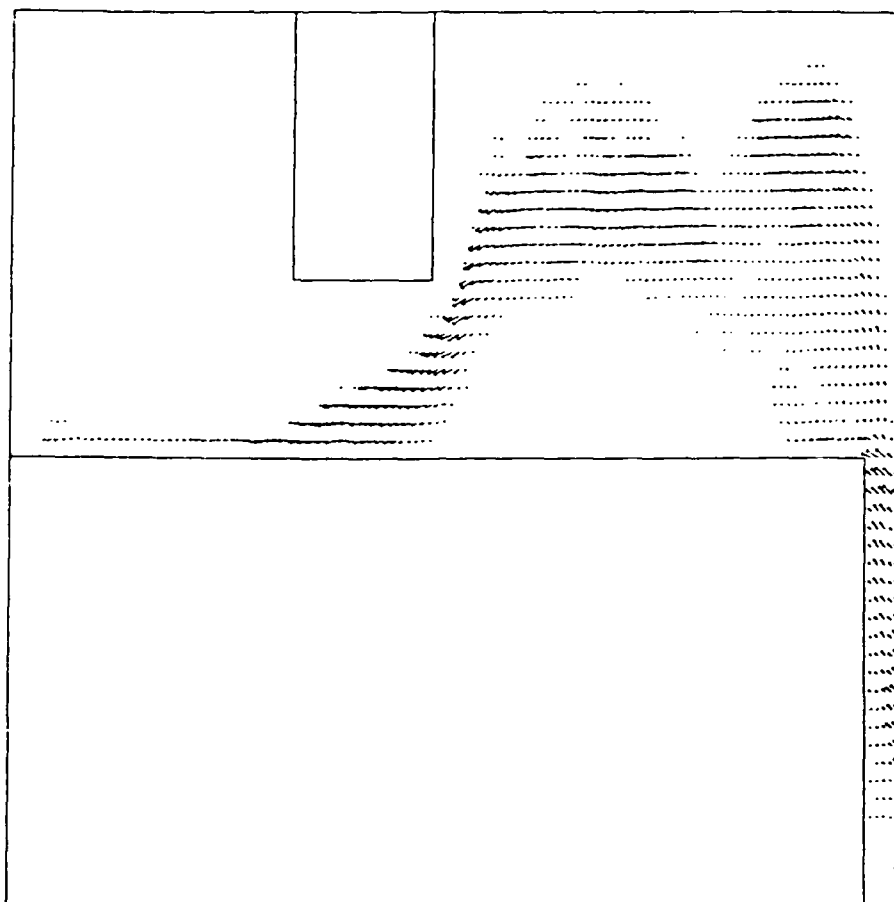


Figure 17. Example of Beam Launching.

The arrows on this plot indicate the direction and magnitude of the vacuum current flow.

leave the cathode.

To obtain a more quantitative idea of this, one may electrostatically determine the fields for the structure of interest. The geometry to be considered is given in figure 18. To simplify the mathematics and conserve much of the physics one can consider the region within the dashed lines in cartesian coordinates. Physically this is equivalent to letting r_a , r_c go to infinity while maintaining d and D . The expressions obtained from an analysis similar to the following, but done in cylindrical coordinates, are cumbersome.

In cartesian coordinates, the potential (φ) at $y = D$ is V_a , at $y = 0$ it is 0, and at infinity the potential is bounded. At $x = 0$, $0 \leq y \leq d$, $\varphi = V_a y/d$. By standard techniques it is found that the potential within the dashed region is:

$$\begin{aligned} \varphi(x, y) = & \frac{2V_a}{\pi} \left[\sum_{n=1}^{\infty} \frac{1}{n} \left[\frac{\sin \lambda_n d}{\lambda_n d} + (-1)^{n+1} \right] \sin(\lambda_n y) \exp(-\lambda_n x) \right. \\ & \left. + \int_0^{\infty} \left[\frac{\sin \beta x}{\beta} \right] \left[\frac{\sinh \beta y}{\sinh \beta D} \right] d\beta \right] \quad (131) \end{aligned}$$

where $\lambda_n = \frac{n\pi}{D}$. The negative of the gradient of (131) gives the electric field components:

$$\begin{aligned} E_x = & \frac{2V_a}{\pi} \left[\sum_{n=1}^{\infty} \frac{\pi}{D} \left[\frac{\sin \lambda_n d}{\lambda_n d} + (-1)^{n+1} \right] \sin(\lambda_n y) \exp(-\lambda_n x) \right. \\ & \left. - \int_0^{\infty} \cos \beta x \left[\frac{\sinh \beta y}{\sinh \beta r_a} \right] d\beta \right] \quad (132) \end{aligned}$$

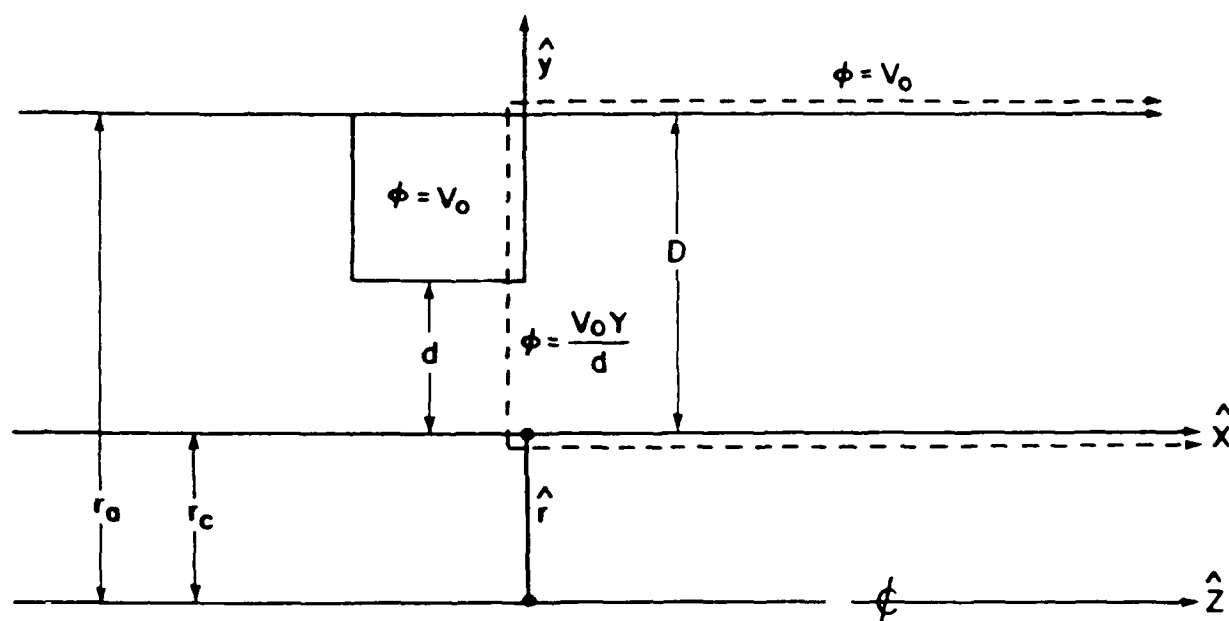


Figure 18. Geometry for Theoretical Analysis of Beam Launching.

$$E_y = -\frac{2V_a}{\pi} \left[\sum_{n=1}^{\infty} \frac{\pi}{D} \left[\frac{\sin \lambda_n d}{\lambda_n d} + (-1)^{n+1} \right] \cos(\lambda_n y) \exp(-\lambda_n x) + \int_0^{\infty} \sin \beta x \left[\frac{\cosh \beta y}{\sinh \beta r_a} \right] d\beta \right] \quad (133)$$

The magnetic induction can be approximated using Ampere's law — given the current through the load (I_a):

$$\vec{B} \cong -\frac{\mu_0 I_a}{w} \hat{z} \quad (134)$$

where w is the width of the system.

From (130) \vec{v}_e becomes:

$$\vec{v}_e = \left[\frac{E_x + \frac{r_l^2}{4} \left[\frac{\partial^2 E_x}{\partial y^2} - \frac{\partial^2 E_x}{\partial x^2} \right]}{B_z} \right] \hat{y} - \left[\frac{E_y + \frac{r_l^2}{4} \left[\frac{\partial^2 E_y}{\partial x^2} - \frac{\partial^2 E_y}{\partial y^2} \right]}{B_z} \right] \hat{x} \quad (135)$$

Since the finite Larmor radius effect is often a 2nd order effect, it is instructive to write out the drift velocity components neglecting the terms related to the finite radius effect. From (132)-(135):

$$v_x = \frac{2V_a}{\pi B_z} \left[\sum_{n=1}^{\infty} \frac{\pi}{D} \left[\frac{\sin \lambda_n d}{\lambda_n d} + (-1)^{n+1} \right] \cos(\lambda_n y) \exp(-\lambda_n x) + \int_0^{\infty} \sin \beta x \left[\frac{\cosh \beta y}{\sinh \beta r_a} \right] d\beta \right] \quad (136)$$

$$v_y = \frac{2V_a}{\pi B_z} \left[\sum_{n=1}^{\infty} \frac{\pi}{D} \left[\frac{\sin \lambda_n d}{\lambda_n d} + (-1)^{n+1} \right] \sin(\lambda_n y) \exp(-\lambda_n x) \right]$$

$$- \int_0^\infty \cos \beta x \left[\frac{\sinh \beta y}{\sinh \beta r_a} \right] d\beta \quad (137)$$

In the limit $x \rightarrow \infty$, (136) and (137) go to:

$$v_x = \frac{V_a}{B_z D} = \left| \frac{E_y}{B_z} \right| \quad (138)$$

$$v_y = 0 \quad (139)$$

This is as expected. Far away from the PEOS perturbation, the electrons $\vec{E} \times \vec{B}$ drift only in the \hat{x} direction (figure 18).

However, close to the perturbation, there is a sizable \hat{y} component of drift (see equation (137)). This \hat{y} component of drift has a maximum close to the perturbation edge. It decreases to zero at the anode and the cathode. It also decreases exponentially as one moves away from the perturbation in \hat{x} . Therefore, after the perturbation launches the beam, it has less and less effect on the receding electron flow. In addition, since the \hat{y} component of drift goes to zero at the cathode an initially wider space charge electron flow (not as well trapped) will be more severely effected (Note: $\hat{x} \rightarrow \hat{z}$, $\hat{y} \rightarrow \hat{r}$, $\hat{z} \rightarrow \hat{\theta}$ when approximating cylindrical geometries).

To more realistically see how this works, a MASK calculation is presented in which the $\vec{E} \times \vec{B}$ launching mechanism is studied for an insulated system with an ion emitting structure (similar to an opening PEOS). The study requires one to first estimate the average components of the \vec{E} and \vec{B} fields across the flow in the launching region. From figure 19, the average magnetic induction across and along the electron stream in the launch region is (the

launched electrons are within the dashed lines of figure 19):

$$\vec{B} \cong -1.8 \hat{\theta} \text{ (Tesla)}.$$

From figure 20, the average \hat{r} component of the electric field along the flow in the launch region is approximately:

$$E_r \cong -3.5 \times 10^8 \hat{r} \text{ (V/m)}.$$

From figure 21, the average \hat{z} component of the electric field is seen to be approximately:

$$E_z \cong 7.8 \times 10^7 \hat{z} \text{ (V/m)}$$

Equation (130) implies that the $\vec{E} \times \vec{B}$ components of drift velocity are:

$$v_r = \frac{E_z}{B_\theta} \cong 4.3 \times 10^7 \text{ (m/sec)}.$$

$$v_z = \frac{E_r}{B_\theta} \cong 1.9 \times 10^8 \text{ (m/sec)}.$$

From figures 22a and 22b it is clear that the launching of the beam occurs primarily between $z \cong .07$ and $z \cong .11$ ($\Delta z \cong .04$ Meters). Using the calculated velocities, it is possible to estimate the sheath displacement (Δs).

$$\Delta s = \frac{\Delta z}{v_z} v_r = .009 \text{ Meters}$$

This displacement is approximately equal to that predicted by MASK as shown in figure 22a,b. Since one can predict the sheath displacement by assuming an $\vec{E} \times \vec{B}$ drift, this implies the $\vec{E} \times \vec{B}$ drift is the primary launching mechanism. Other calculations were examined with and without ion emission from their respective structures. In every case the electron trajectories near the perturbation are consistent with an $\vec{E} \times \vec{B}$ launching mechanism.

AF-4212 746

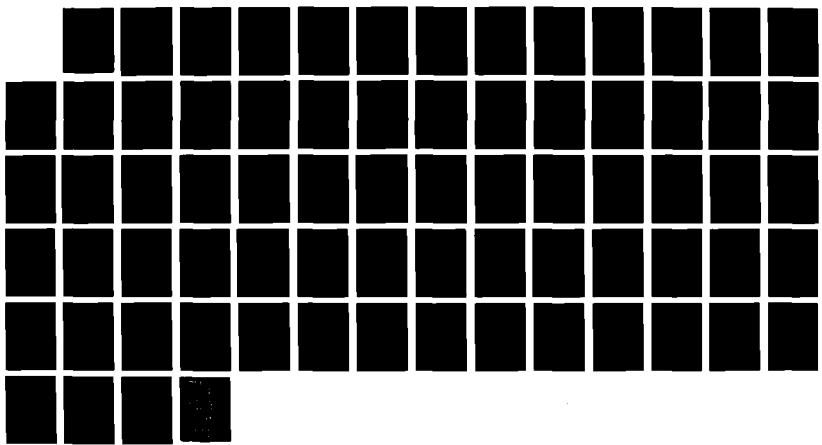
THEORETICALLY INDICATED ELECTRON FLOWS IN PULSED POWER
SYSTEMS(U) FRANK J SEILER RESEARCH LAB UNITED STATES
AIR FORCE ACADEMY CO R I LANCONNELL AUG 89

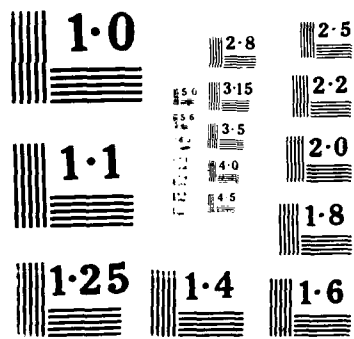
UNCLASSIFIED

FJSRL-TR-89-0008

F/G 20/3

NL





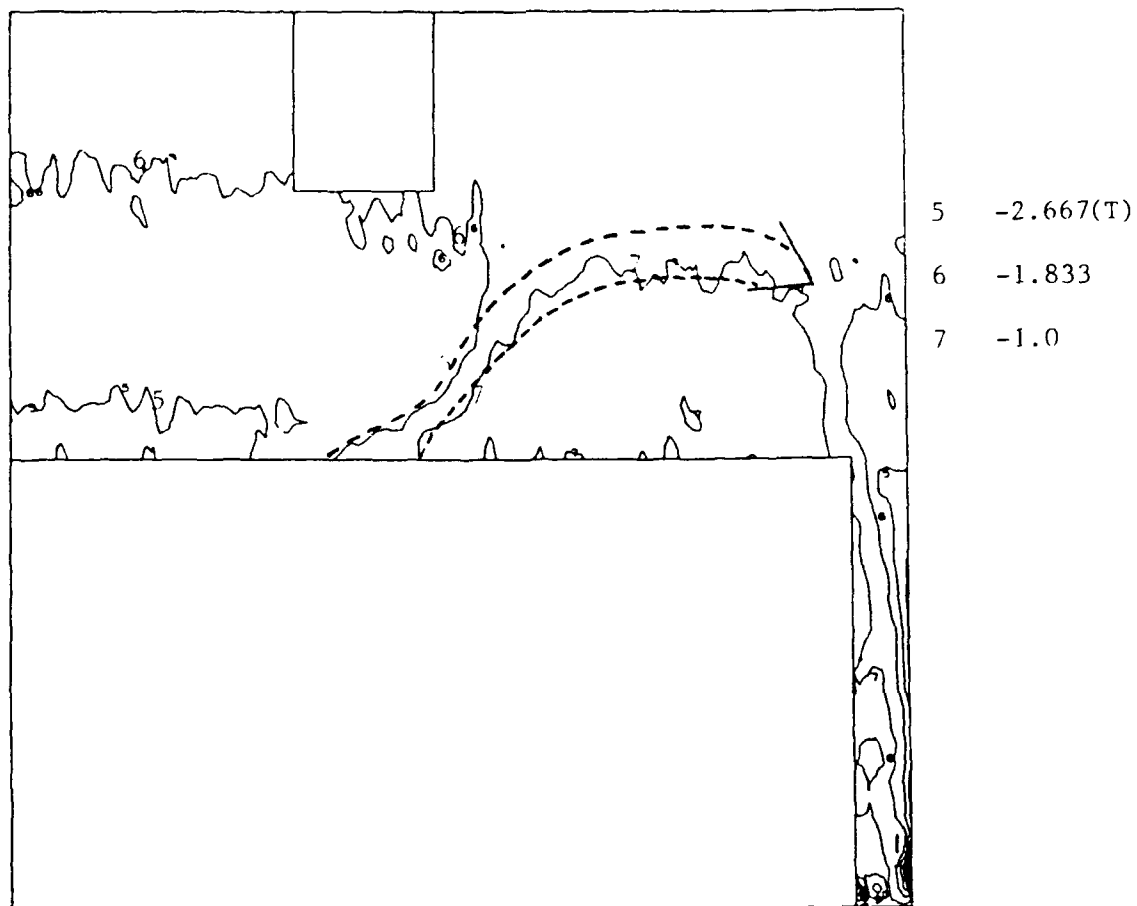


Figure 19. Magnetic Field Within the Launched Beam.

The average magnetic field on the electrons at the right edge of the PEOS is approximately given by contour level number 6. The electrons move between the dashed lines in the general direction of the arrow.

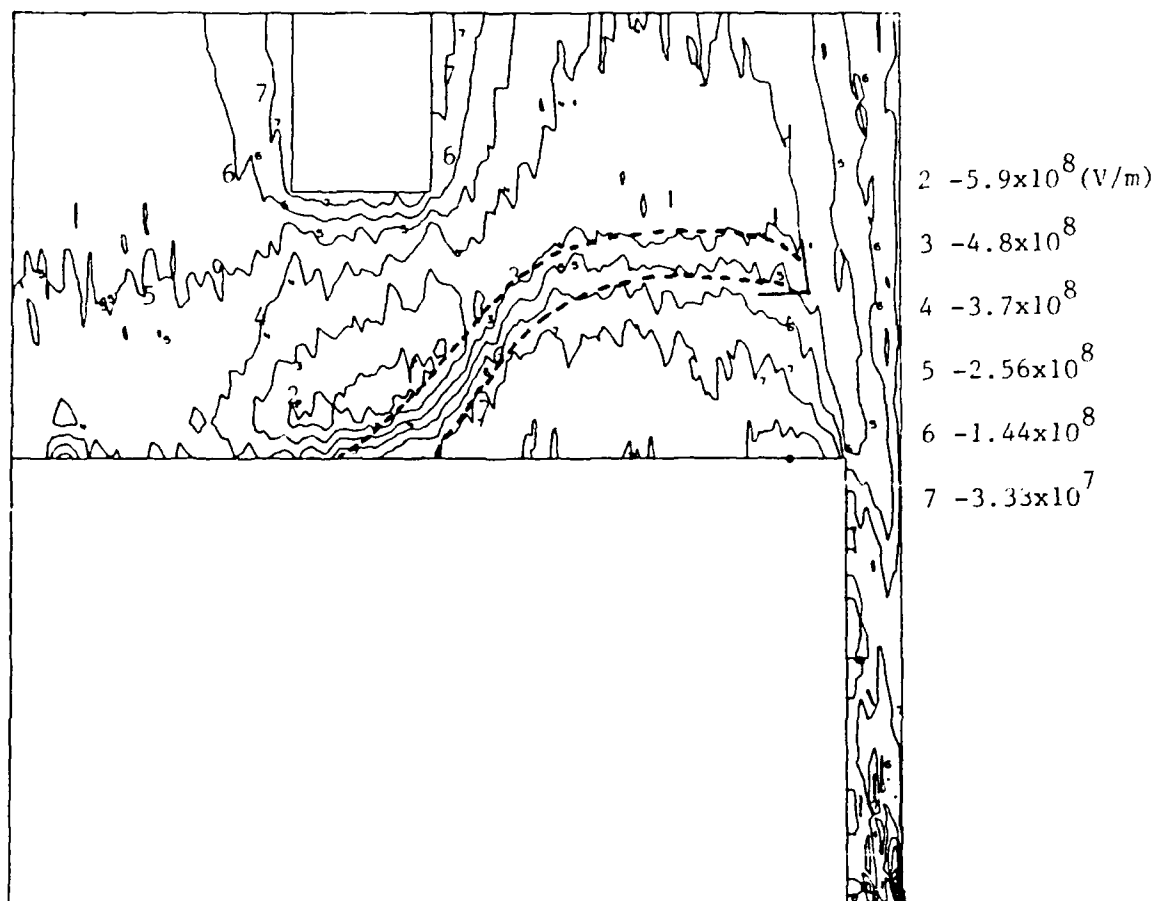


Figure 20. Electric Field (r) Within the Launched Beam.

The approximate r -component of the electric field acting on the launched electrons (between the dotted lines) is given by averaging contour levels 3, 4 and 5.

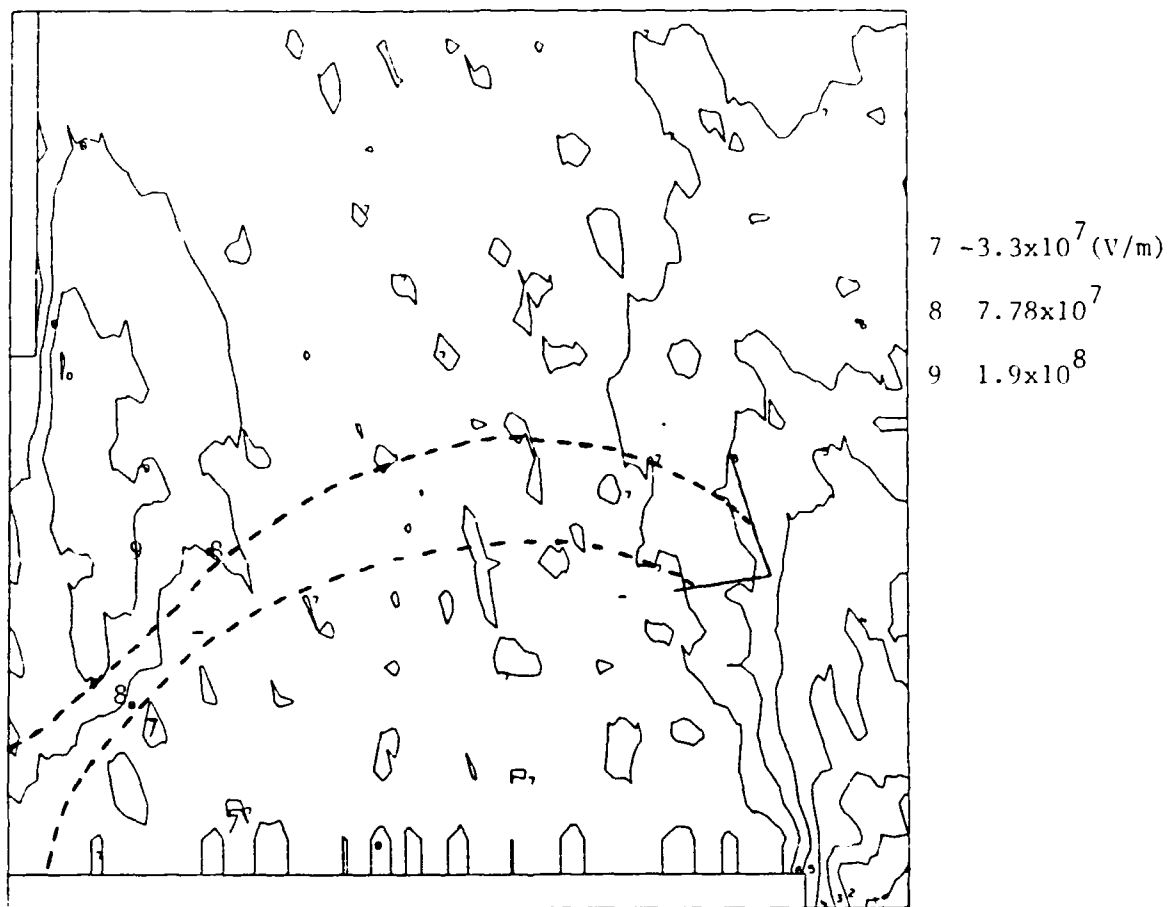
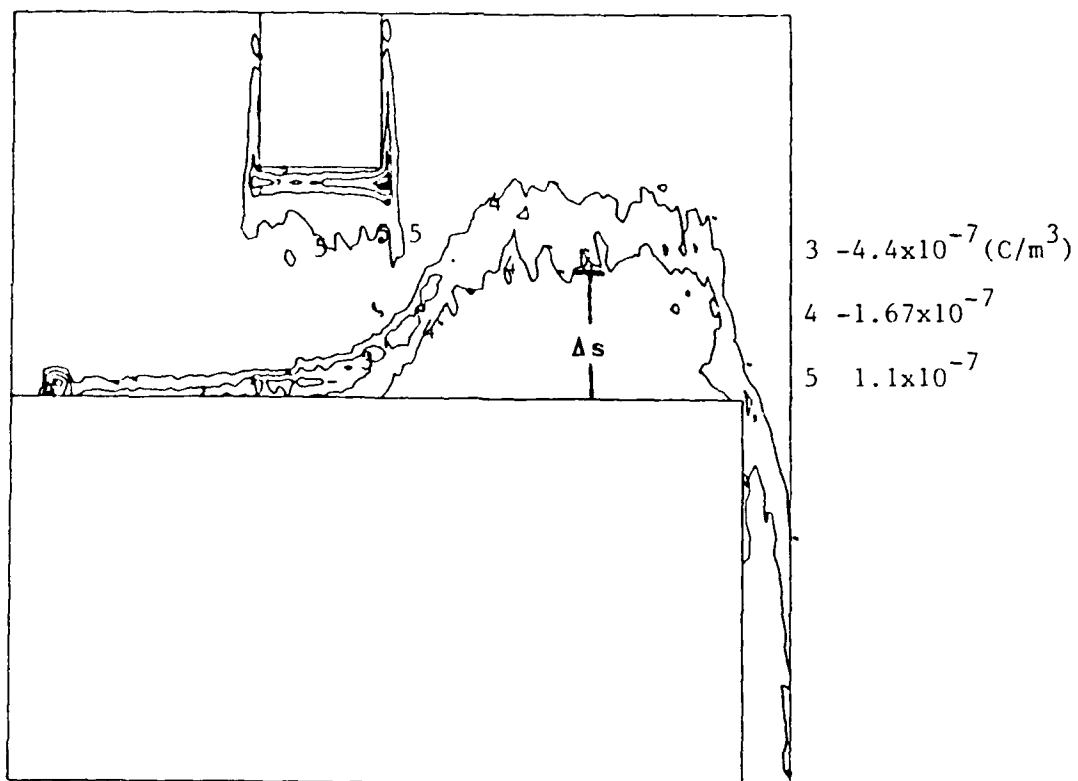
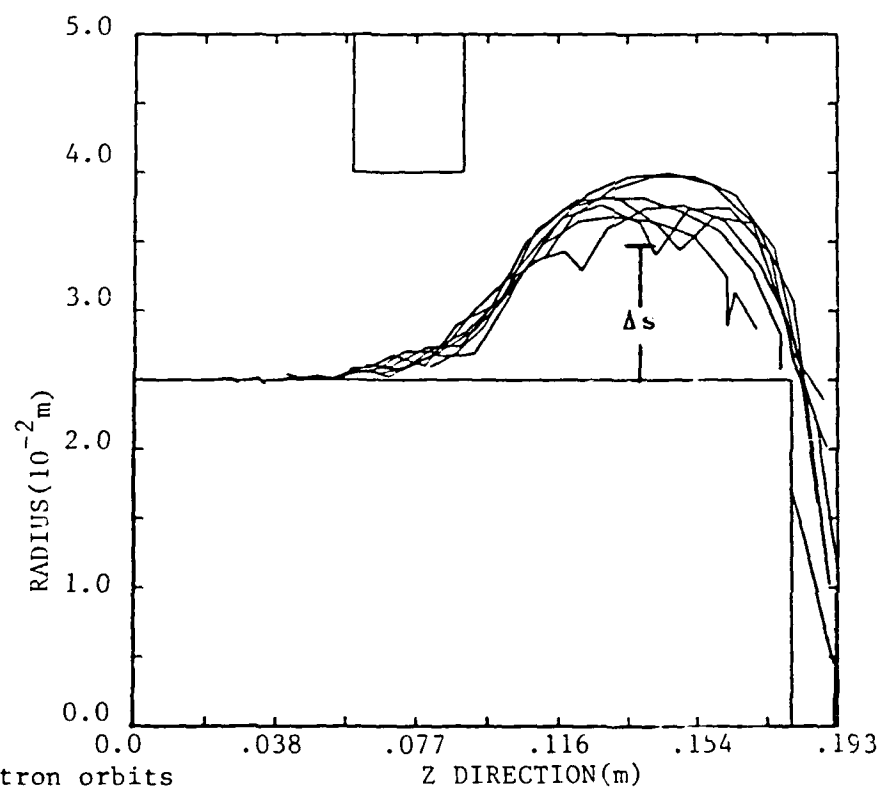


Figure 21. Electric Field(z) Within the Launched Beam.

The average z-component of the electric field in the launch region is given approximately by contour level number 8 (it bisects the electron flow). The electrons flow between the dashed lines in the direction indicated by the arrow.



a. Charge density.



b. Electron orbits

Figure 22. Charge Density and Electron Orbits for a Launched Beam.

4.2.2 Laminar Flows

If the impedance of the load relative to the impedance of the line as a function of voltage is within approximately 10% of the ratio give in figure 39, the launched electron beam will propagate in a laminar fashion (see Appendix C, Tables C4-C9). This of course applies only to the electron flow downstream of an abruptly varying structure as shown in figure 23. The flow referred to as being laminar here is not really laminar in that $\dot{r} \neq 0$. However, the electrons typically travel 10 or more Larmour radii in the \hat{z} direction per gyration. Since the excursion in \hat{r} is close to two Larmour radii per gyration the orbits are fairly laminar. In the following these semi-laminar orbits will be investigated for one MASK run (characteristic of many). Then using the general laminar flow theory, a flow solution is generated for laminar electron flows downstream of the PEOS. The laminar flows are of particular interest since it is often desirable to run systems with as large a load as possible and still maintain magnetic insulation (this puts one into the laminar regime).

The simulation to be considered is MASK run PN06 (see Appendix C, Table C5). The maximum potential difference between the anode and cathode is 2MV. There is no ion emission from the perturbation and the problem has been run to equilibrium. In figure 23, one can see the typical semi-laminar electron orbits under consideration (Note that if the r and z axis had the same scale the plot would appear

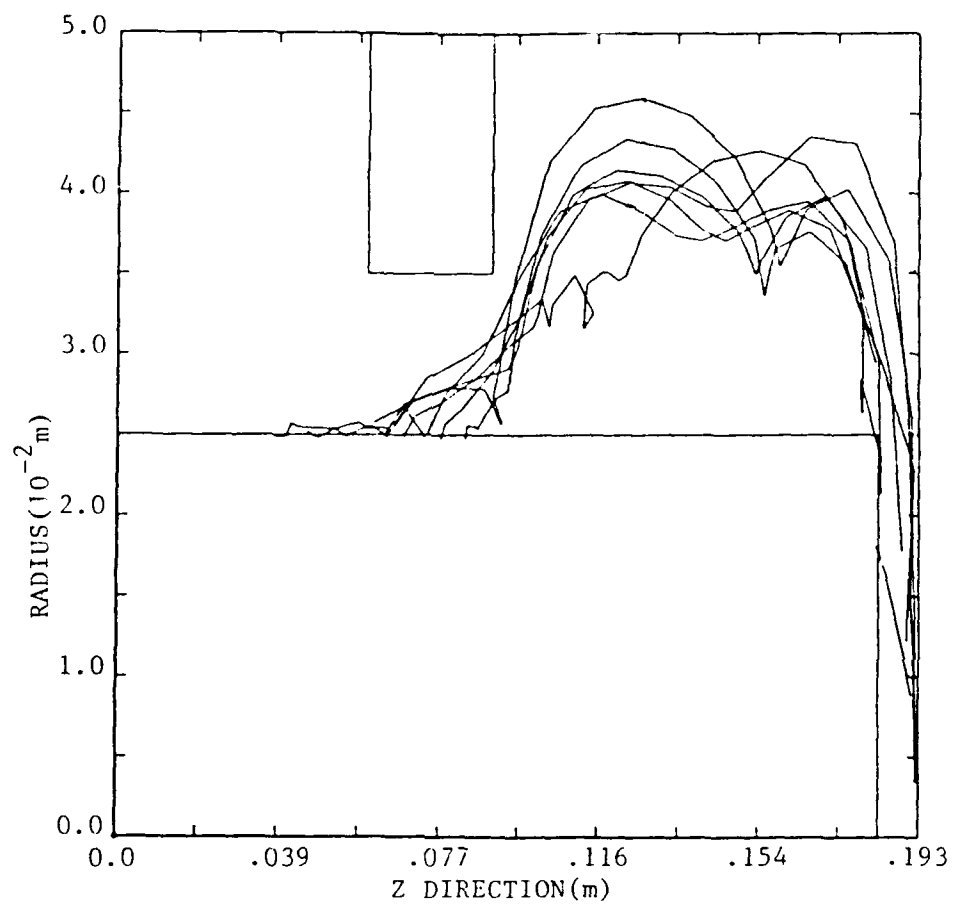


Figure 23. Laminar Electron Orbits for a Launched Beam.

4 times longer in the \hat{z} direction). From figure 23, it can be seen that the electrons move 5 to 6 times further in the \hat{z} direction than their excursions in the \hat{r} direction per gyration. The orbits are fairly laminar. This is due to the perturbation modifying the electron orbits and velocities such that the electric and magnetic field forces cancel:

$$E_r - v_z B_\theta = 0. \quad (140)$$

If $E_r < v_z B_\theta$ the electrons are accelerated towards the cathode; however, if $E_r > v_z B_\theta$ the electrons are accelerated towards the anode. If $E_r = v_z B_\theta$ the electrons move in perfectly laminar orbits. A relative measure of the laminar nature of the electron flows can be obtained by comparing the values of $E_r - v_z B_\theta$ at the turning point for different load impedances. The more laminar flows will have smaller absolute values for $E_r - v_z B_\theta$. This will be demonstrated by examining two MASK simulations.

The outer turning point for the electrons in MASK simulation PN06 is approximately given by a radius of .045 meters (r_m). From figures 24 and 25, $E_r(r_m) \cong -1.6 \times 10^8$ and $B_\theta(r_m) = -\mu_0(5.0 \times 10^5)$. From figure 26, $v_z(r_m) = \frac{P_1}{\gamma} \cong 2.8 \times 10^8$. This implies:

$$E_r - v_z B_\theta \cong 1.67 \times 10^7 \quad (141)$$

Multiplying this by the electron charge results in a negative \hat{r} directed force which causes the electrons to move towards the cathode. However, it is a relatively small force as can be seen in comparison to the next simulation.

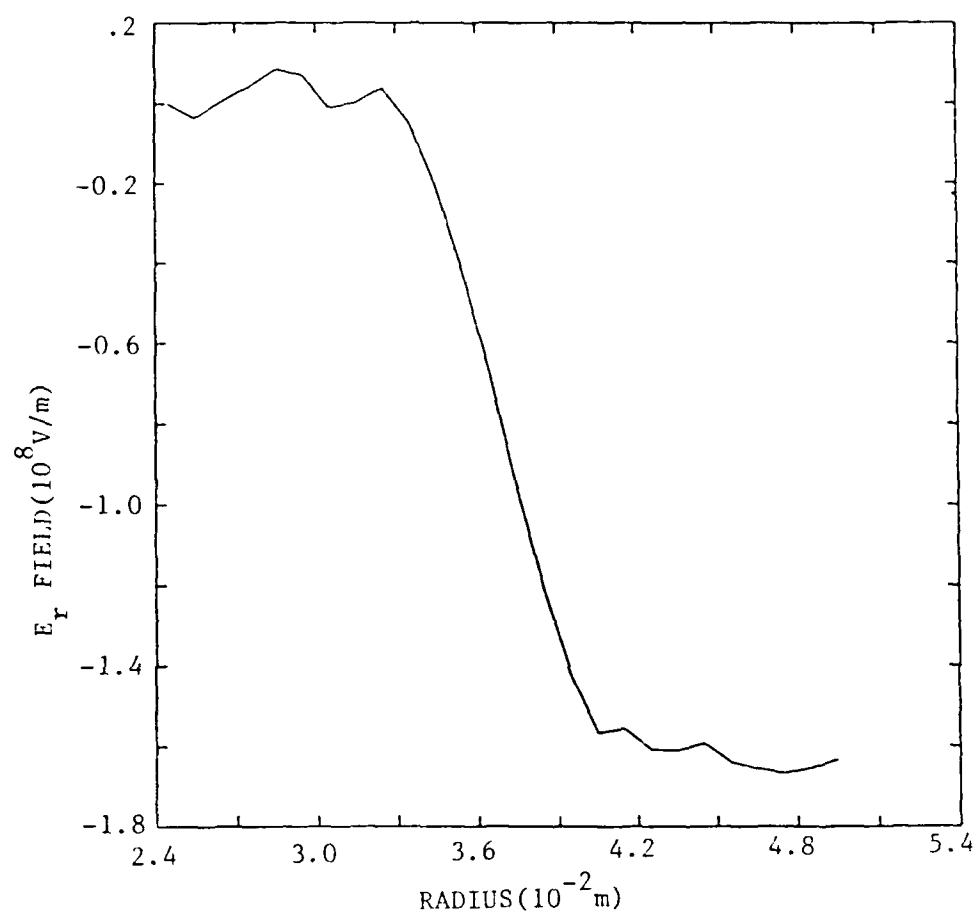


Figure 24. Electric Field (\hat{f}) Histogram for a Laminar Flow

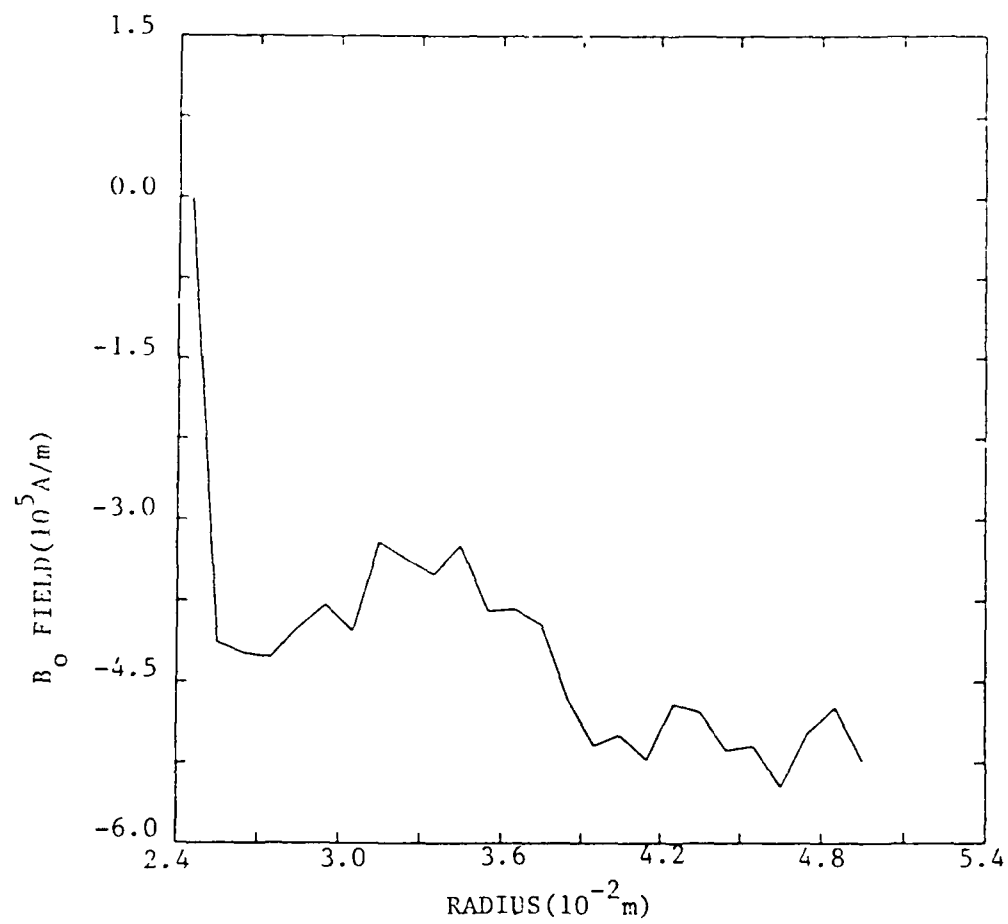


Figure 25. Magnetic Field (theta) Histogram for a Laminar Flow.

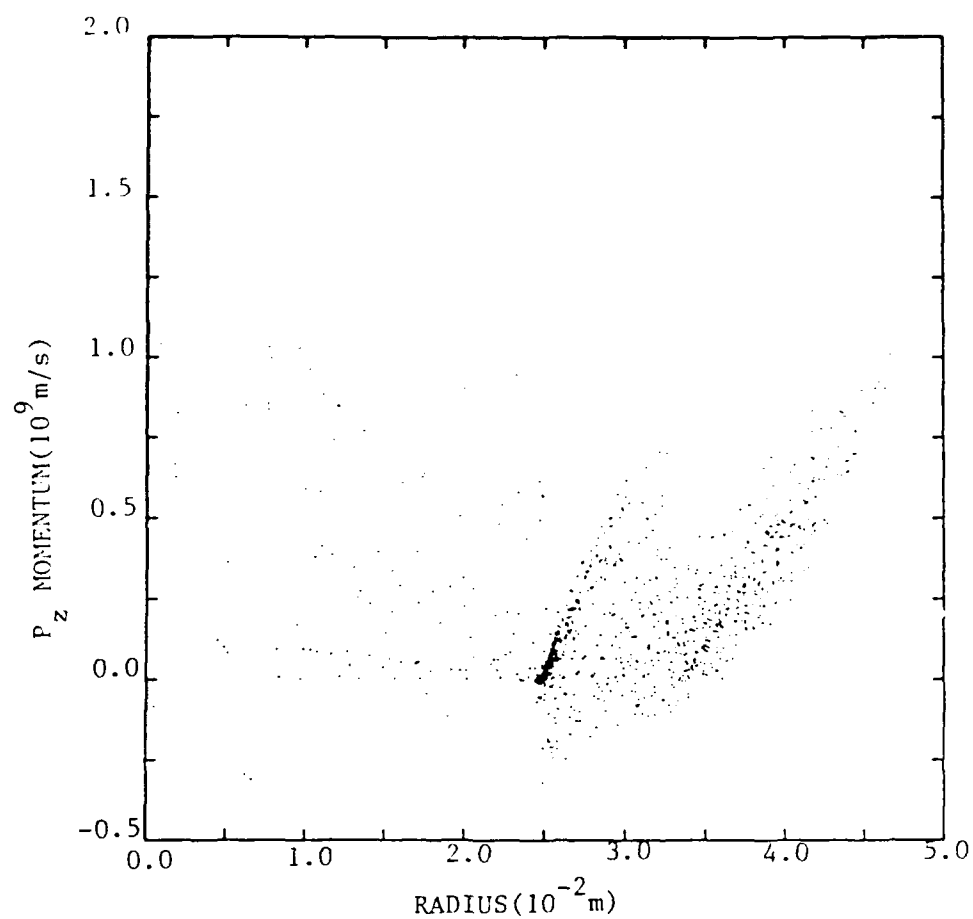


Figure 26. Momentum (\hat{z}) Particle Plot for a Laminar Flow.

Note: The "momentum" is given by $P_z = \gamma v_z(r)$. The mass is not included.

The next case is for simulation PN04 (Appendix C4). This case corresponds to simulation PN06 in everyway except that the load impedance is reduced which causes a more tightly trapped non-laminar electron flow downstream of the perturbation. The typical electron orbits for simulation PN04 are shown in figure 27. The outermost point for the electron orbits is $r_m = .045$ Meters. From figures 28 and 29 the fields are:

$$E_r(r_m) \cong -1.375 \times 10^8$$

$$B_\theta(r_m) \cong -.82$$

From figure 30, the \hat{z} component of velocity is $v_z = 2.87 \times 10^8$. So,

$$E_r - v_z B_\theta = +1. \times 10^8 \quad (142)$$

In comparing equation (141) and (142), the minus \hat{r} directed force of (142) is six times greater than that given in equation (141). Considering this result, it is not surprising that the electron flow downstream of the PEOS in simulation PN06 is laminar relative to PN04.

As mentioned previously, it is often desirable to power loads with the largest possible impedance, resulting in semi-laminar flows downstream of abrupt perturbations (i.e. PEOS). From a series of PEOS calculations (Tables C7-C9) it is found that the electron density profiles downstream of the perturbation are often approximately given as follows:

$$\left. \begin{array}{ll} \rho(r) = 0 & r_c \leq r \leq r_i \\ \rho(r) \cong \text{constant} & r_i \leq r \leq r_o \\ \rho(r) = 0 & r_o \leq r \leq r_a \end{array} \right\} \quad (143)$$

where r_c is the cathode radius, r_i is the inner radius of the launched beam, r_o is the outer radius of the beam and, r_a is the anode radius. Since the flow is primarily laminar the general theory of laminar flows (from Chapter 3) can be used to predict flow quantities of interest. Since the density is approximately constant across the flow, the constant density solution can be modified to give the downstream electron flow.

The laminar flow solution downstream of a PEOS is given in equations (143)-(162):

For $r_c \leq r \leq r_i$,

$$v_z(r) = \vec{j}(r) = \varphi(r) = \vec{E}(r) = f(r) = 0 \quad (144)$$

$$\vec{B}(r) = \frac{\mu_o I_c}{2\pi r} \hat{\theta} \quad (145)$$

$$A_z(r) = -\frac{\mu_o I_c}{2\pi} \ln(r/r_c) \hat{z} \quad (146)$$

For $r_i \leq r \leq r_o$ (see equations (105)-(114)):

$$f(r) = \frac{r^2 - r_i^2}{r_o^2 - r_i^2} \quad (147)$$

$$\begin{aligned} \vec{v}(r) = & -\frac{I_c}{\pi |\rho| (r^2 - r_i^2)} \left[\left[1 + \left[\frac{I_a^2 - I_c^2}{I_c^2} \right] f^2(r) \right]^{1/2} \right. \\ & \left. - \left[1 + \left[\frac{I_a^2 - I_c^2}{I_c^2} \right] f^2(r) \right]^{-1/2} \right] \hat{z} \quad (148) \end{aligned}$$

$$\vec{J}(r) = -|\rho|\vec{V}(r) \quad . \quad (149)$$

$$\varphi(r) = \frac{|\rho|}{4\epsilon_0} (r^2 - r_i^2 - 2r_i^2 \ln(r/r_i)) \quad . \quad (150)$$

$$\vec{E}(r) = - \frac{|\rho|(r^2 - r_i^2)}{2\epsilon_0 r} \hat{r} \quad . \quad (151)$$

$$A_z(r) = - \frac{\mu_0 I_c}{2\pi} K_1(r) \hat{z} \quad . \quad (152)$$

$$\vec{B}(r) = \frac{\mu_0 I_c}{2\pi r} \left[\left[\frac{I_a^2 - I_c^2}{I_c^2} \right] \left[\frac{r^2 - r_i^2}{r_o^2 - r_i^2} \right]^2 + 1 \right]^{1/2} \hat{\theta} \quad . \quad (153)$$

and

$$K_1(r) = \frac{1}{2} \left[(ax^2 + bx + c_1) + \frac{b}{2} \left[a^{-1/2} \ln(2a^{1/2}(ax^2 + bx + c_1)^{1/2} + 2ax + b) \right] - c_1^{1/2} \ln \left[\frac{2(c_1^{1/2}(ax^2 + bx + c_1)^{1/2} + bx + 2c_1)}{x} \right] \right] \frac{2r^2}{2r_i^2} \quad . \quad (154)$$

where $a = c_3/4$, $b = -c_3 r_i$, $c_1 = c_3 r_i^4 + 1$, and

$$c_3 = \frac{I_a^2 - I_c^2}{I_c^2} \frac{1}{(r_o^2 - r_i^2)^2} \quad .$$

For $r_o \leq r \leq r_a$ (see equations (115)-(120)):

$$\varphi(r) = \frac{|\rho|}{4\epsilon_0} (r_o^2 - r_i^2) (2 \ln(r/r_o) + 1) - 2r_i^2 \ln(r_o/r_i) \quad . \quad (155)$$

$$\vec{E}(r) = - \frac{|\rho|}{\epsilon_0 r} (r_o^2 - r_i^2) \hat{r} \quad . \quad (156)$$

$$\vec{A}(r) = \left[- \frac{\mu_0 I_c}{2\pi} \ln(r/r_o) + c_4 \right] \hat{z} \quad . \quad (157)$$

$$\vec{B}(r) = \frac{\mu_o I_a}{2\pi r} \hat{\theta} \quad (158)$$

and

$$\vec{v}(r) = \rho(r) = \vec{j}(r) = 0 \quad (159)$$

$$\text{where } c_4 = - \frac{\mu_o I_c}{2\pi} K_1(r) \Big|_{2r_i}^{2r_o} \quad (160)$$

The electron density is given by:

$$|\rho| = \frac{(I_a^2 - I_c^2)^{1/2}}{\pi c (r_o^2 - r_i^2)} \quad (161)$$

The radius to the outer edge of the beam is obtained iteratively from (equations (155) at the anode and (161)):

$$\left[\frac{r_o}{r_i} \right] \left[\frac{1}{1 - (r_i/r_o)^2} \right] = \frac{r_a}{r_c} \exp \left[.5 - \frac{2\pi\epsilon_o c V_a}{(I_a^2 - I_c^2)^{1/2}} \right] \quad (162)$$

One may obtain a detailed flow solution for the laminar flow downstream of the PEOS from these equations given the applied voltage across the diode (V_a), the anode (I_a) and cathode (I_c) currents, the anode (r_a) and cathode (r_c) radii and the inner radius (r_i) of the launched beam.

All these variables are easily obtained except the inner radius of the beam. The inner radius (r_i) depends on the size of the perturbation, diode voltage, anode and

cathode currents, and geometry. How these relate to the inner beam radius has not been quantitatively determined. One can estimate r_i based on the expected electric fields in the launch region as was done in section 4.2.1. The inner beam radius for the launched beam can be very roughly approximated by:

$$r_i = r_c + \frac{(r_a - r_p)}{2} \quad (163)$$

4.2.3 Non-Laminar Flows

It is important to stress that if the impedance of the load relative to the impedance of the line as a function of voltage is less than that which gives laminar flows (see section 4.2.2), the launched beam will form circulating rings of charge (figure 31a,b). These rings will $\vec{E} \times \vec{B}$ drift down the transmission line. The individual electron orbits are usually prolate and curtate (see figures 1 and 31b).

In highly trapped electron flows, the launched beam does not come close to satisfying (140). Since the electron beam curls up, it no longer can completely shield the cathode from electric fields. Therefore, between vortex rings (circulating electrons, $\vec{E} \times \vec{B}$ drifting together down the line) space charge limited electron emission occurs from the cathode. Underneath each vortex ring, there is no electron emission because of the rings shielding effect (see fig 33a). This phenomena is rather irregular and can be most easily predicted using a 2-dimensional electromagnetic code. The general theory of laminar flows can not be used in such a situation.

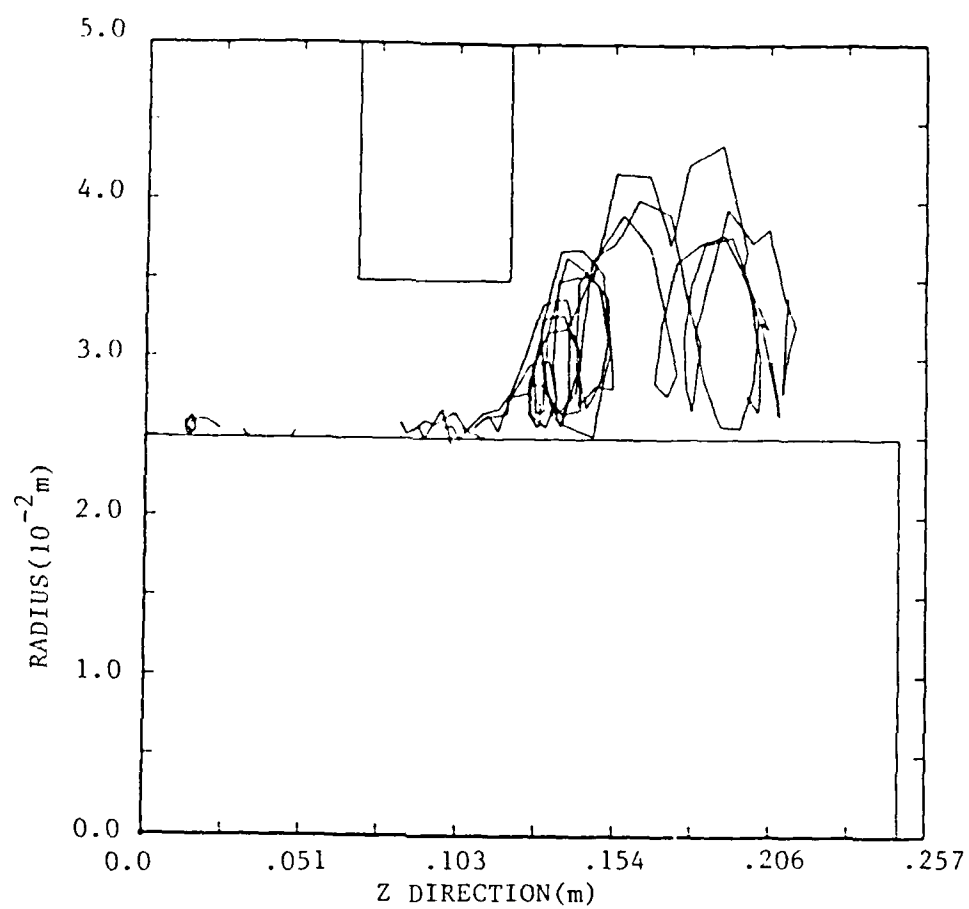


Figure 27. Non-Laminar Electron Orbits for a Launched Beam.

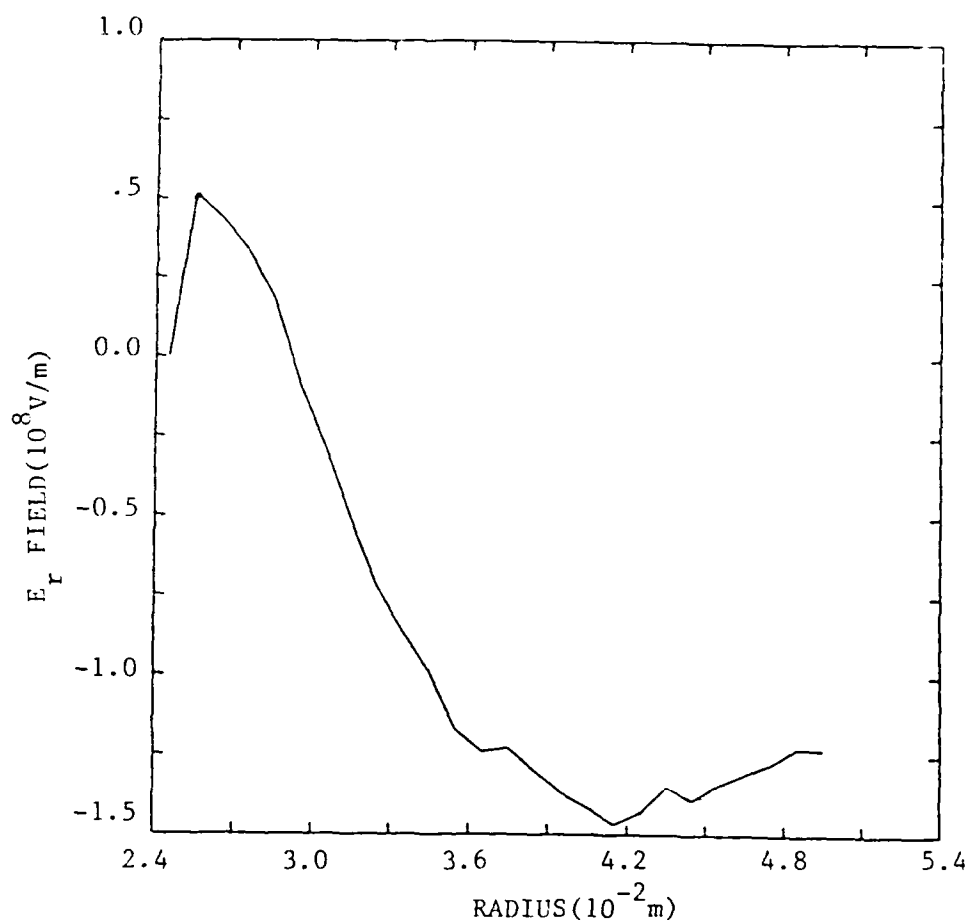


Figure 28. Electric Field (\hat{r}) Histogram for a Non-Laminar Flow.

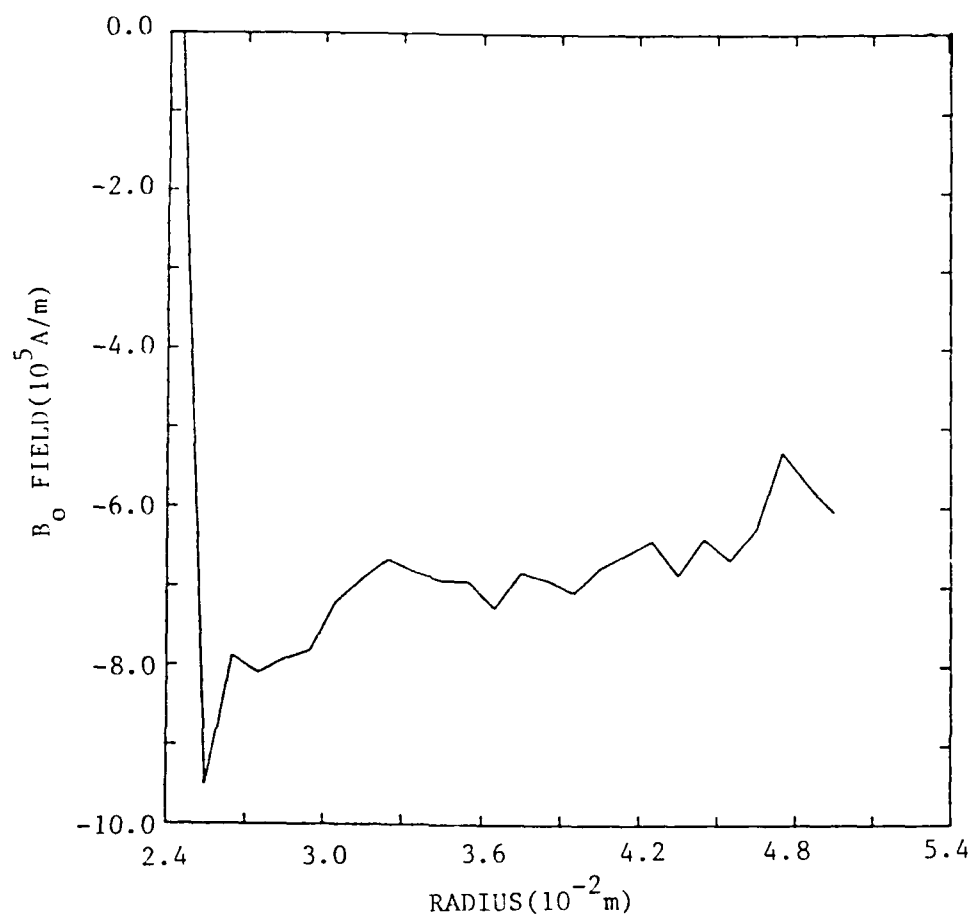


Figure 29. Magnetic Field (6) Histogram for a Non-Laminar Flow.

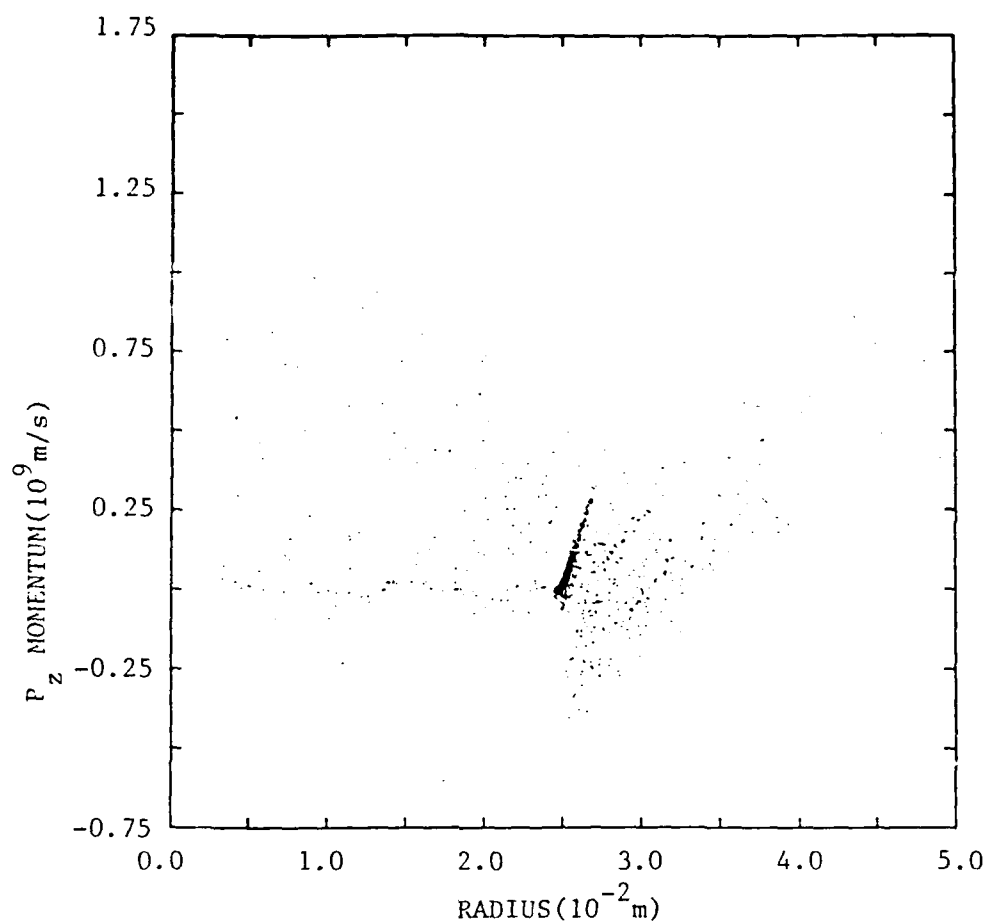
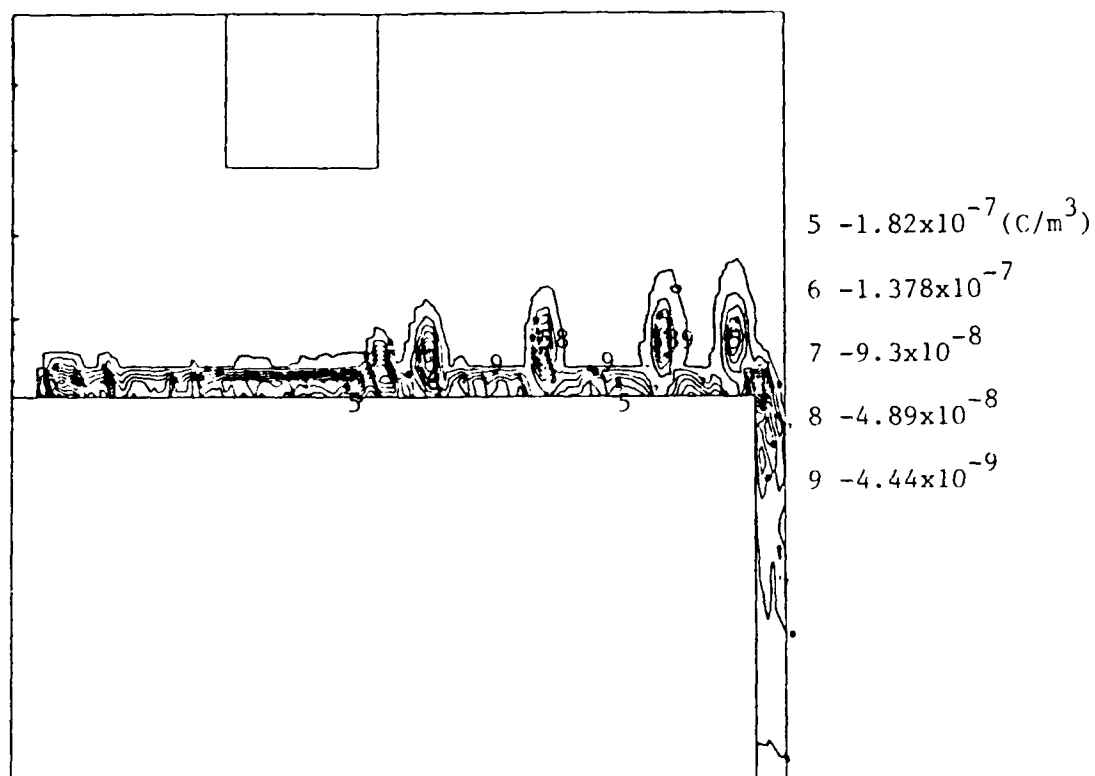
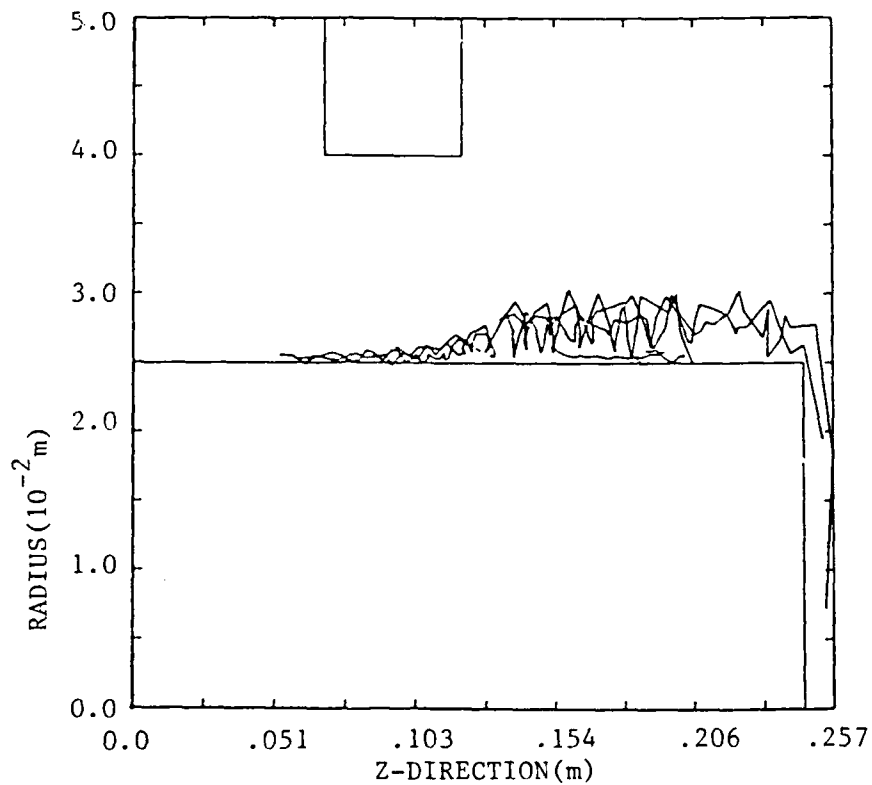


Figure 30. Momentum (\hat{z}) Particle Plot for a Non-Laminar Flow.

Note: $P_z = \gamma v_z(r)$; the mass has been factored out.



a. Charge density.



b. Electron orbits.

Figure 31. Charge Density and Electron Orbits for a Launched Tightly Trapped Beam.

CHAPTER 5

MAGNETIC INSULATION THRESHOLD

There are three types of magnetically insulated flow:

1) load-limited, 2) self-limited, and 3) constant-flux -limited flow (see figure 2). In load limited cylindrical MITLs (see figure 2), there is a maximum load impedance (as a function of voltage) above which magnetic insulation degenerates across the load. This results in current being excluded from the load as shown in figure 32. This loss of current is undesirable. To determine what the magnetic insulation threshold is (above which current is lost) for a variety of perturbed and unperturbed MITLs is the objective of this Chapter.

Now, it is interesting to note that a load limited MITL transitions to a self-limited MITL at the point current begins to be excluded from the load. This is fortunate because current flows in self-limited magnetically insulated lines have been treated theoretically in cylindrical coordinates by Wang and DiCapua [33] assuming a Brillouin flow field. Wang and DiCapua determine the minimum energy operating point of self-limited MITLs as a function of applied voltage. Realizing that the normalized energy of the Brillouin flow at the transition point (between load-limited and self-limited flows) is inversely proportional to the normalized load impedance allows one to invert Wang and DiCapuas' results to obtain figure 33. So,

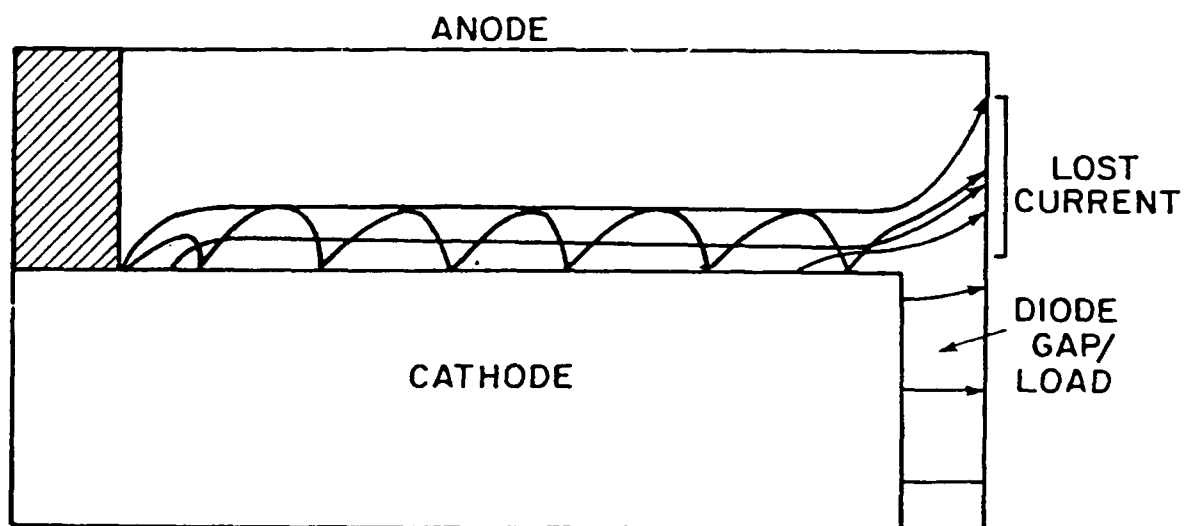


Figure 32. Current Loss Due to Magnetic Insulation Deterioration.

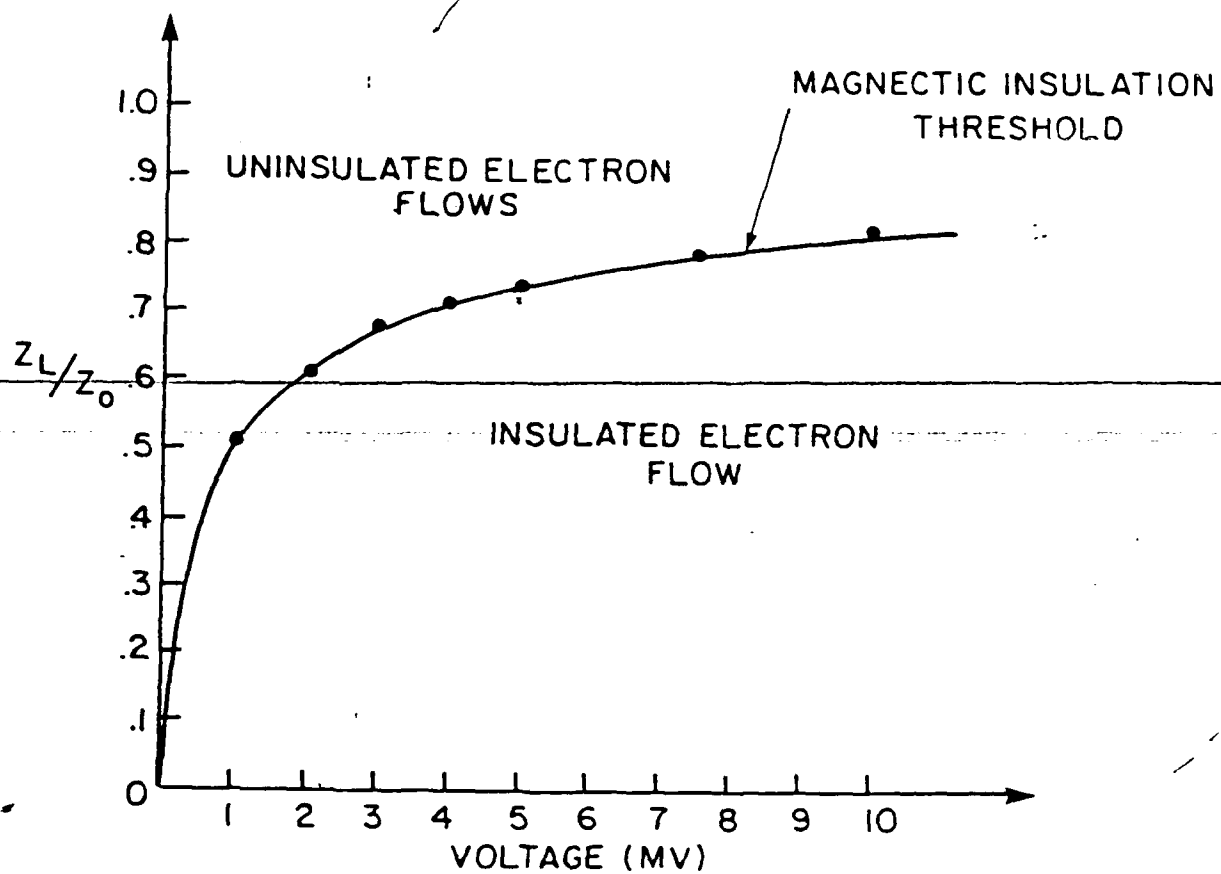


Figure 33. Magnetic Insulation Threshold for Brillouin Flows.

This is an inversion of Wang and DiCapuas' minimum energy operating point verses voltage graph (33).

instead of an energy verses voltage plot, a normalized load impedance(z_1/z_0) verses applied voltage plot is obtained, where z_1 and z_0 are the load and line impedances respectively. In this work, such a plot is referred to as the magnetic insulation threshold of the system..

In the following, it becomes apparent that all load limited lines with trapped flows operate below the z_1/z_0 magnetic insulation threshold curve. MITLs operating above the curve shown in figure 33 experience current loss (as shown in figure 32). Thus, figure 33 becomes a guide to the magnetic insulation threshold for infinitely long (no significant end effects observed in the flow) cylindrical MITLs with no perturbations. This curve is justified by detailed MASK calculations in this chapter. In addition, curves similar to that of figure 33 are computationally generated in which the magnetically insulated threshold for finite systems with structures (some structures simulate an opening PEOS) are presented. Some of these magnetic insulation threshold curves are justified by using them to successfully predict experimental results from a Gamble II PEOS experiment.

5.1 Slightly Perturbed Flow

In this portion of the magnetic insulation threshold study, data was pulled from approximately forty MASK simulations (Appendix C, Tables C1-C3) of finite MITLs (see figure 3a). This data is plotted and discussed in the following.

The simulations typically require about 4 nanoseconds

of physical time for the MITL to come to equilibrium. All the values in Tables C1-C3 correspond to the equilibrium condition. Longer MITLs would require more time to come to equilibrium as discussed in section 4.2 and indicated on figure 16.

The threshold for complete magnetic insulation is best represented by a z_l/z_o vs voltage graph, where z_l is the load impedance and z_o is the transmission line vacuum impedance. The voltage is that applied across the transmission line. A typical data point for such a graph is obtained by doing 3 or 4 short MASK calculations in which the diode gap (figure 3a) is increased while maintaining a constant voltage difference across the line. When the current begins to be excluded from the load (figure 32), magnetic insulation of the load deteriorates.

Determining when this begins is easily done if one plots z_l/z_o vs the diode gap spacing (d_g). This results in a line of constant positive slope as long as the flow is trapped. However, when d_g becomes so large that current begins to be excluded from the load, the slope of z_l/z_o vs d_g goes to zero (where z_l is defined to be V_a/I_a). An example of this type of graph is given in figure 34. The data points come from simulations M407-M424 of Table C1. The point at which the slope of the line goes to zero (in figure 34) corresponds to the magnetic insulation threshold for the given conditions. The slope goes to zero because when the load impedance exceeds the self-limited impedance

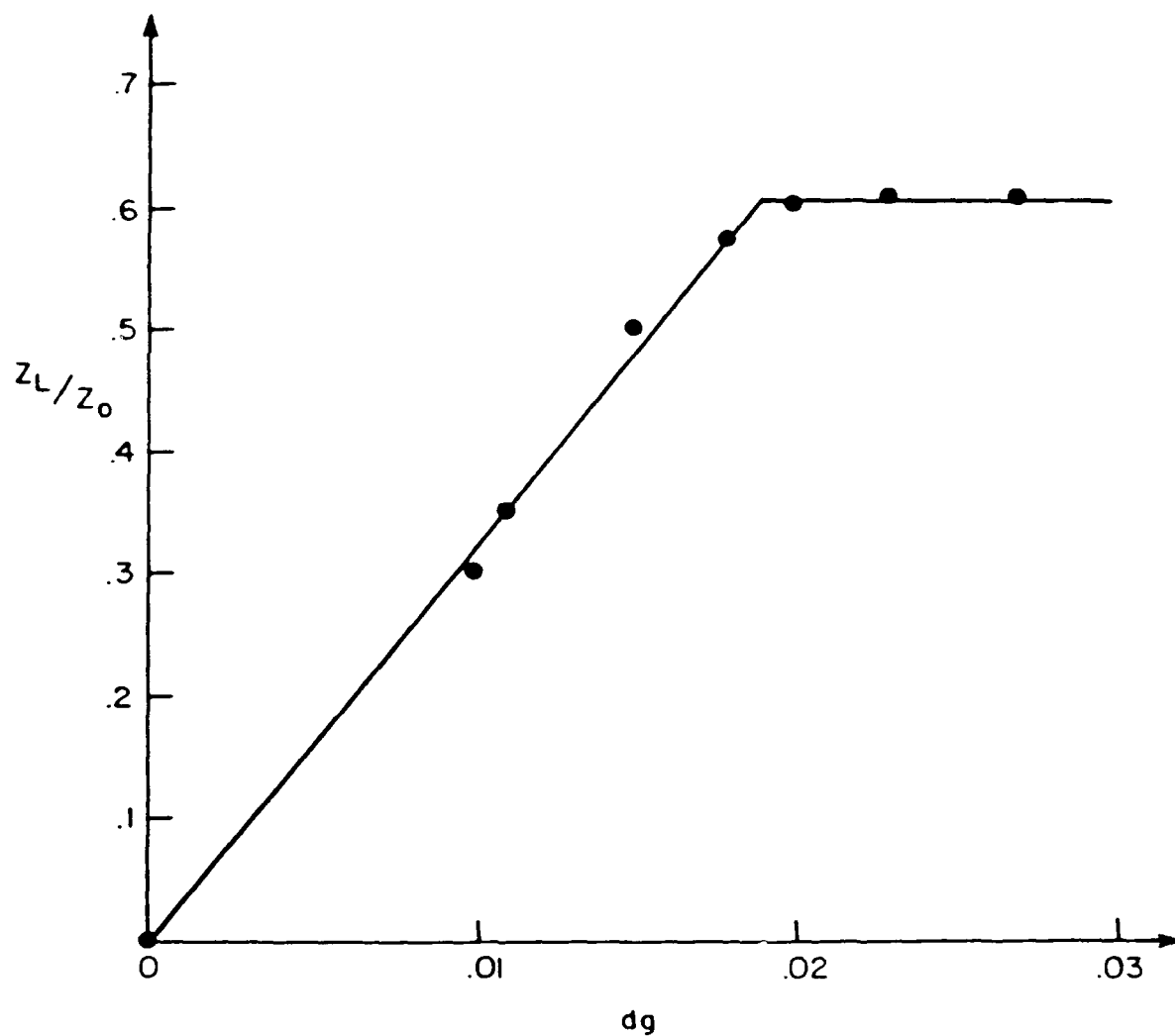


Figure 34. Normalized Load Impedance Vs. Diode Gap Spacing.

The point at which the slope of the line goes to zero corresponds to the magnetic insulation threshold. This is for the case of $V_0 = 2 \times 10^6$ volts, $r_a = .05$, $r_c = .025$ meters.

of the line, the current flowing through the line begins to short across the line. This means that as one continues to increase the diode gap spacing more and more current is excluded from the load. However, the current flowing in the system (including the short) is given by the self-limited impedance of the line — which is a constant.

After plotting the data in Tables C1-C3, figure 35 results. It should be noted that each point on this graph is found by the technique illustrated in figure 34 and discussed above. Figure 35 gives the magnetic insulation threshold in terms of z_1/z_0 vs voltage plots. The upper line corresponds to coaxial MITLs with no perturbations. It indicates that transmission lines operated below the line lose no current out of the load. The triangled dashed line corresponds to MITLs run with space charge limited ion emission from the anode. Such lines must be run at a lower load impedance, as compared to the ideal case, for magnetic insulation to be effective.

It is also clear in figure 35 that varying the anode/cathode radii had an insignificant effect on the magnetic insulation curves. This is consistent with the flow theory of Wang [33] mentioned earlier. In addition, the Brillouin flow self-limited impedance curves are slightly higher than the calculational curves; but, very close to them. Since all orbits are possible in the MASK calculations and the flows are predominantly non-Brillouin (as demonstrated in Chapter 2), it is surprising to see how

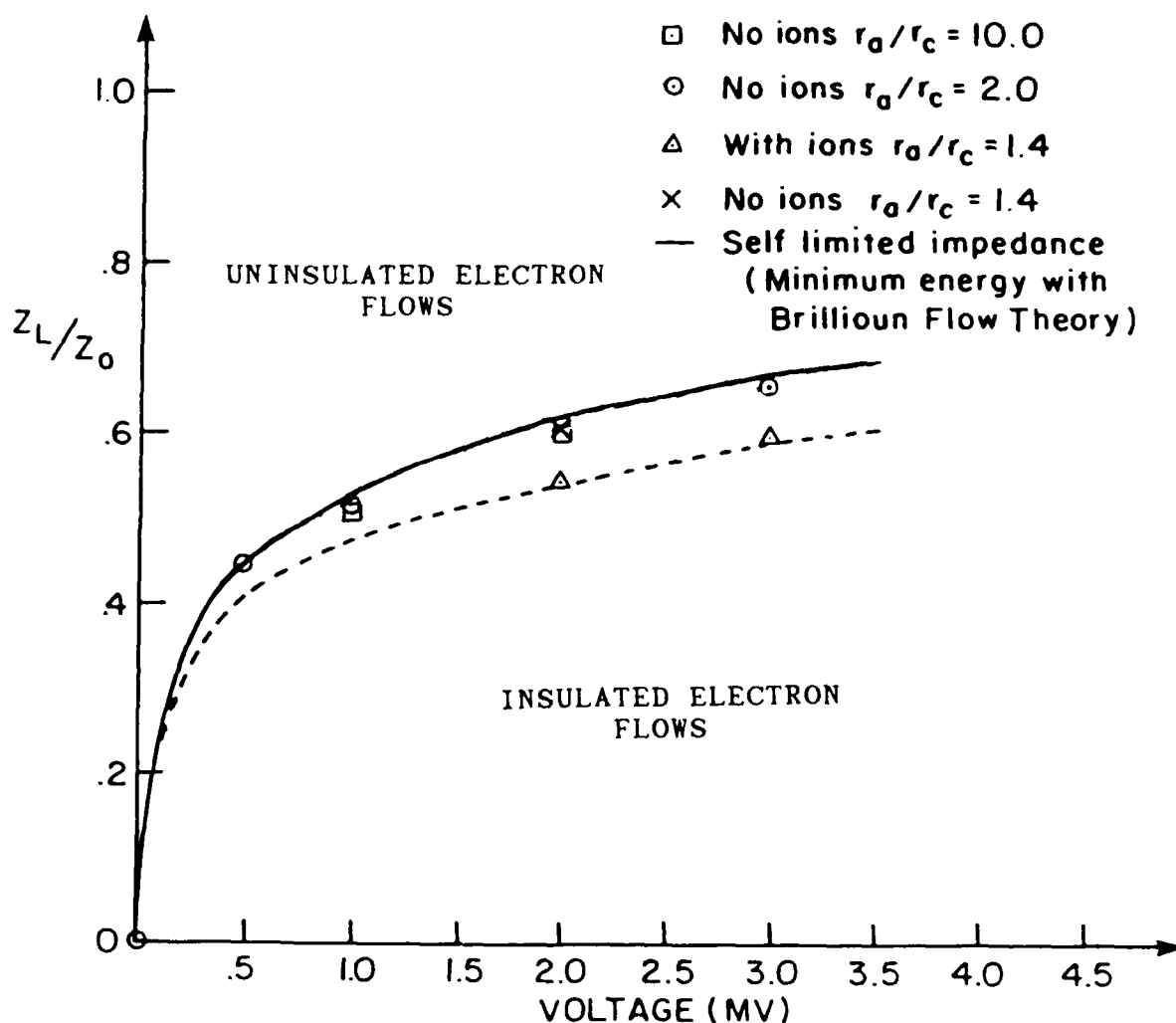


Figure 35. Magnetic Insulation Thresholds for Systems Without Perturbing Structures.

Cylindrical transmission lines with insignificant ion emission off the anode lose no current through the load if operated below the solid line. MITLs with space charge limited ion flow off the anode lose no current if operated under the dotted line.

well the Brillouin minimum energy theory comes to predicting the magnetic insulation threshold found in the calculational study for non-perturbed MITLs. The magnetic insulation thresholds for systems with structures, with and without ion emission are presented in the following section.

5.2 Disrupted Flows

The data for the following study comes from approximately sixty MASK simulations (Appendix C, Tables C4-C9). The MASK mesh for these simulations is given in figure 3b. All the calculations were run to equilibrium. Part of these runs (Tables C4-C6) were done with a large conducting structure in the mesh that did not emit ions. The remainder of the runs (Tables C7-C9) had ion emission from the structure and represented PEOSs in various stages of opening. As a result, the magnetic insulation thresholds that are obtained apply to extremely perturbed systems.

In these simulations the axial extent and location of the perturbation has a small effect on the magnetic insulation properties of the system. The vacuum impedance of the line in the switch (perturbation) region is the most important factor governing insulation. In fact, the vacuum impedance through the switch governs the insulation of the system in a very similar fashion as the vacuum impedance of the MITL in the last section. Because of this, the magnetic insulation threshold is most appropriately represented with a z_1/z_p vs voltage plot, where z_p is the vacuum line impedance under the structure ($60 \ln(r_p/r_c)$).

Once again, the transition from trapped to untrapped

flow can be seen in the z_1/z_p vs d_g plots. A representative z_1/z_p vs d_g plot is given in figure 36 for a non-ion emitting structure. Figure 37, is a compilation of z_1/z_p vs voltage data. The top line, connecting diamonds and squares, corresponds to the magnetic insulation threshold for non-ion emitting structures.

The more interesting and crucial set of runs for understanding a PEOS are represented by the triangles, circles and crosses connected by the dashed line. In these runs, the PEOS structure is a space charge limited ion emitter. If the pulsed power system is run with a load and at a voltage corresponding to the region below the dashed line all current passes through the load. If the load and voltages are such that the system operates above the dashed line, the system will not be fully magnetically insulated and current will be lost. In the next section, functions are generated that fit the data. These functions are then used in section 5.4 to model a Gamble II experiment.

5.3 Fits to Magnetic Insulation Data

It is desirable to have a continuous function that fits the data linked by the dashed line of figure 37. To do this, it is necessary in this study to fit the data for the magnetic insulation of a transmission line with no perturbation (see figure 35). This is because more data points are available for the unperturbed case. Since the graphs have essentially the same form, the unperturbed case can be used to give an estimate of the perturbed case in the

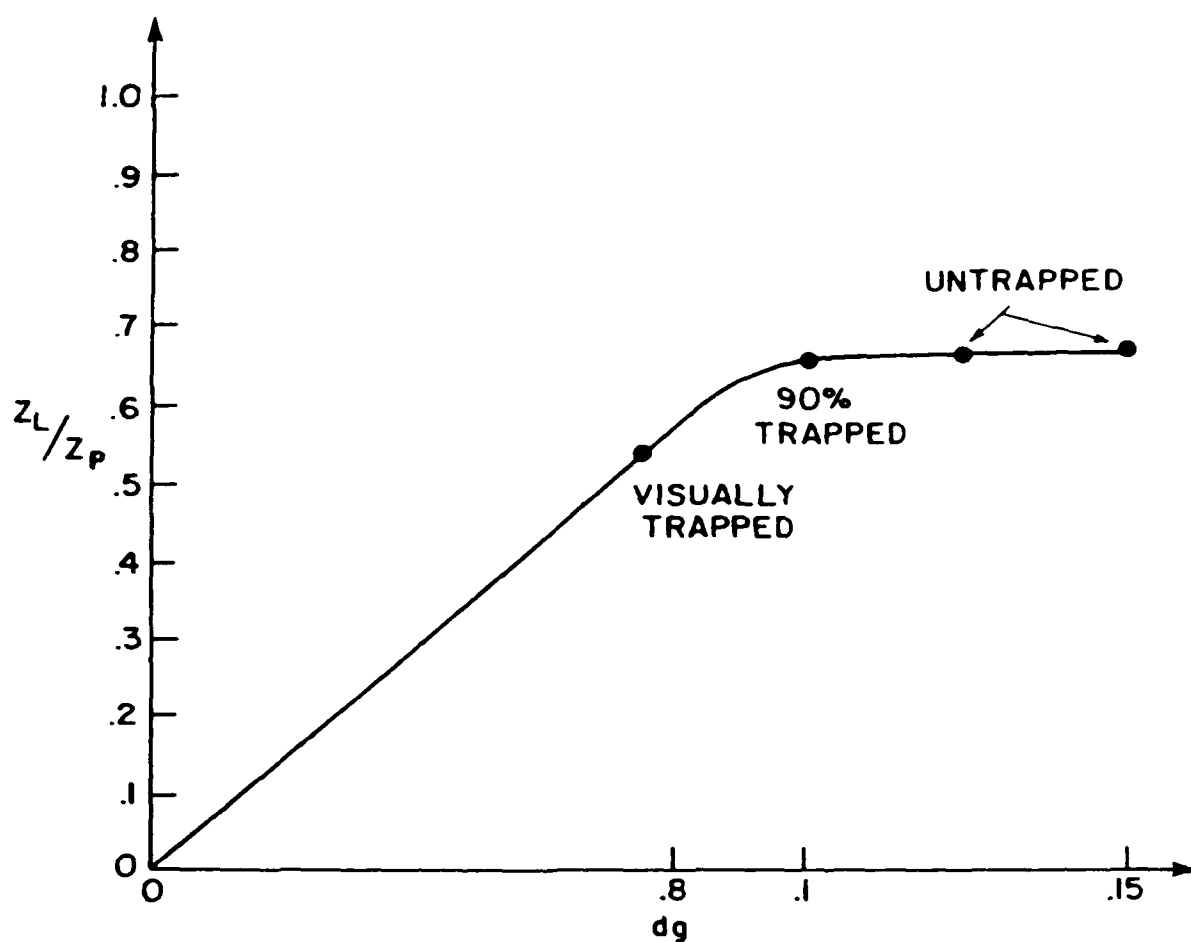


Figure 36. Normalized Load Impedance Verses Diode Gap Spacing with a Perturbing Structure.

The voltage across the diode is 2MV.

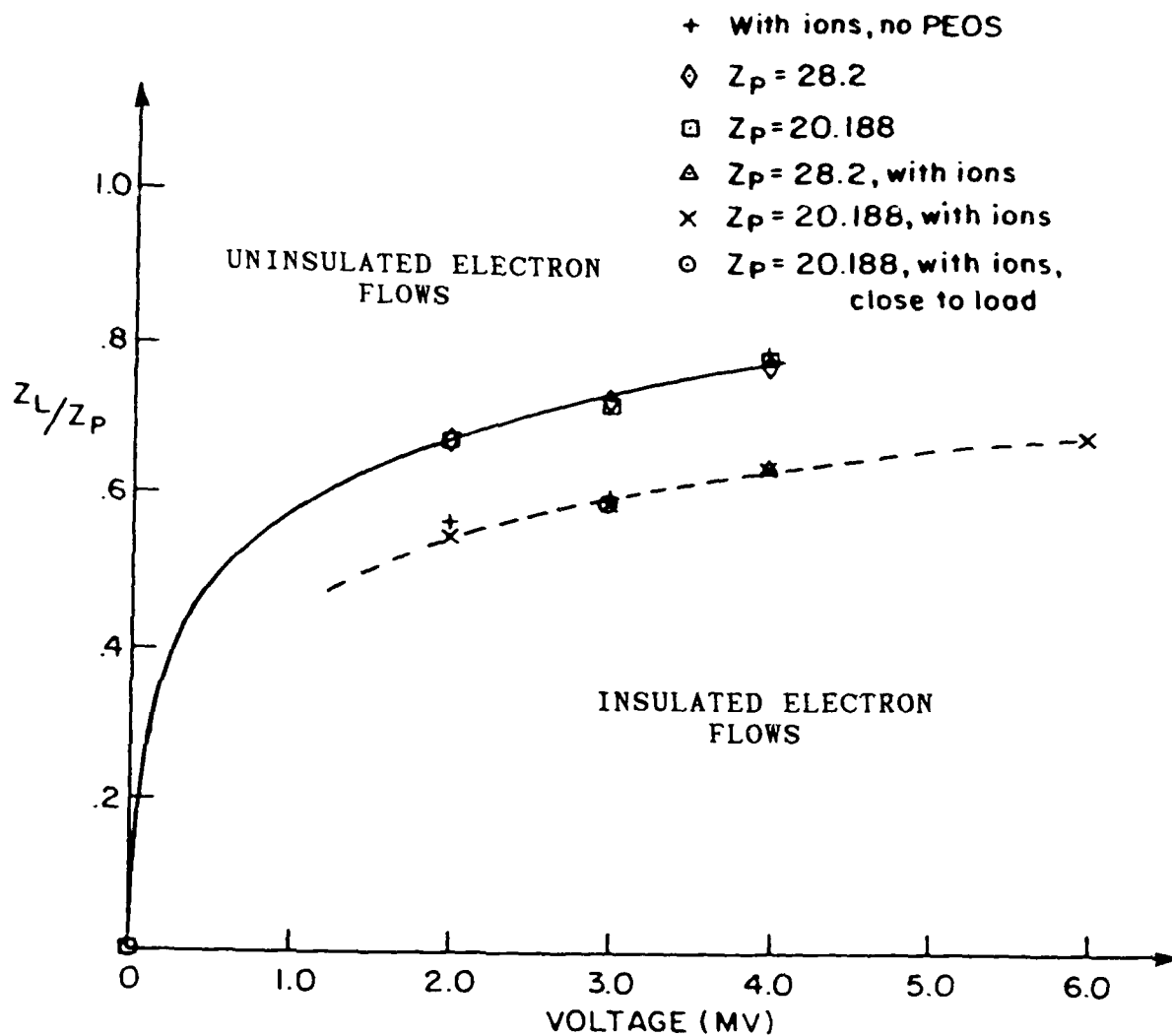


Figure 37. Magnetic Insulation Threshold Data for Systems with Perturbing Structures.

The dashed line corresponds to the magnetic insulation threshold for a PEOS. The solid line corresponds to a MITL with a disruptive structure.

low voltage region. The equations governing the fits are:

$$1) \ z_1/z_p = .51975 \ V \left[.15 + .2 \left[\frac{1 + .51 \ln(1. + 1.9567V)}{1 + 1.9567V} \right] \right] \quad (164)$$

$$2) \ z_1/z_p = .4675 \ V \left[.172 + .2 \left[\frac{1 + .371 \ln(1. + 1.9567V)}{1 + 1.9567V} \right] \right] \quad (165)$$

where equation (164) gives the magnetic insulation threshold for simple MITLs and equation (165) gives the threshold for MITLs with a PEOS. The voltage difference (V) across the anode/cathode gap is in megavolts. These formula match the simulation data to within a percent. They are accurate to within 2% up to 10 megavolts. Extrapolating out to 10 megavolts is made possible by noting the similarities between the theoretical predictions of Wang [33] and the MASK simulations of this study. It should be a simple matter to modify the above relations to give the insulation threshold out to over a 100 megavolts using the same procedure. The magnetic insulation threshold for unperturbed MITLs, as given by equation (164), is shown in figure 38.

The magnetic insulation threshold for a system with a PEOS (from equation (165)) is shown in figure 39. Also, in figure 39, is a plot of the insulation threshold estimate found and used at the Naval Research Laboratory. Figure 40 shows the corresponding critical currents for magnetic insulation for the two cases. From figures 39 and 40, the

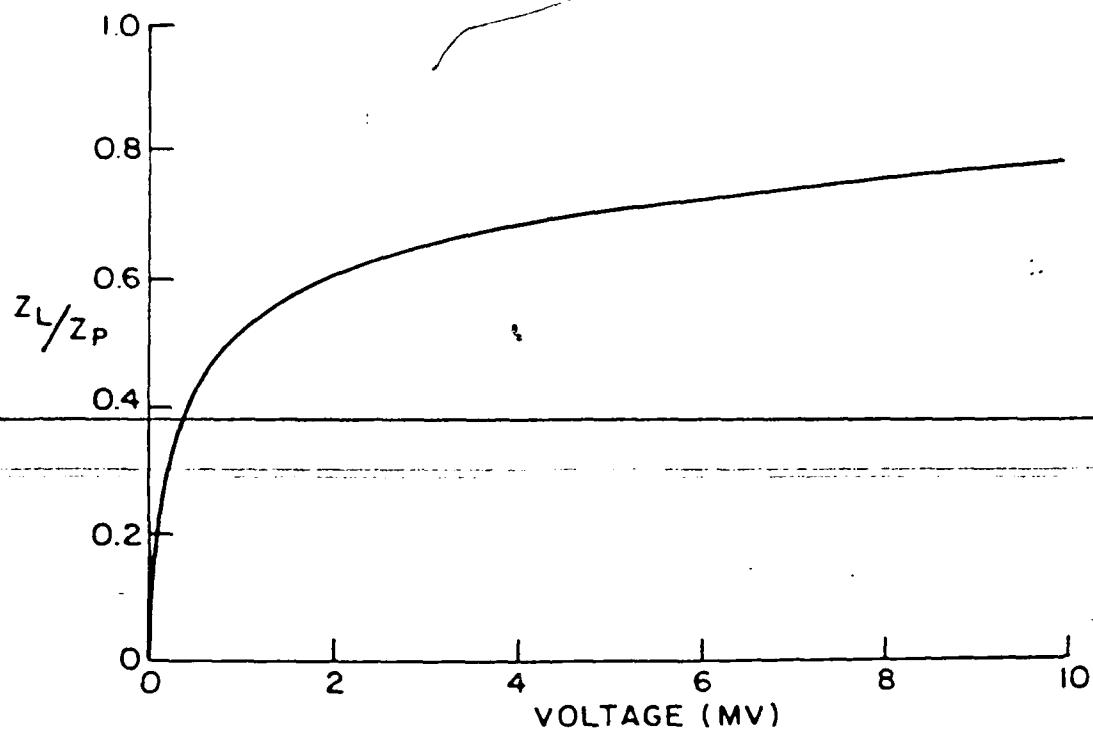


Figure 38. Fit to Data Corresponding to Figure 35.

This fit is for the cases run with no structures and no ion emission.

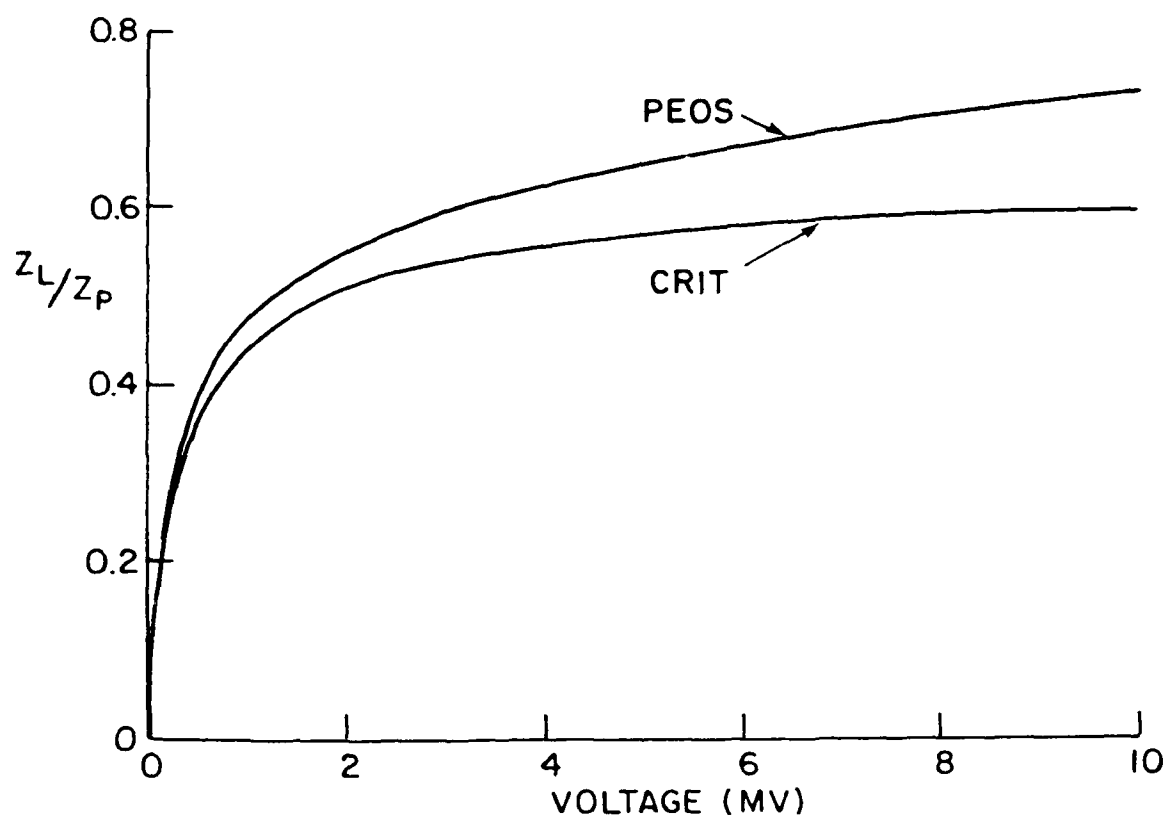


Figure 39. Fit to Computational Data (PEOS, Figure 37) Compared to NRL's Previous Estimate (CRIT) of the Magnetic Insulation Threshold.

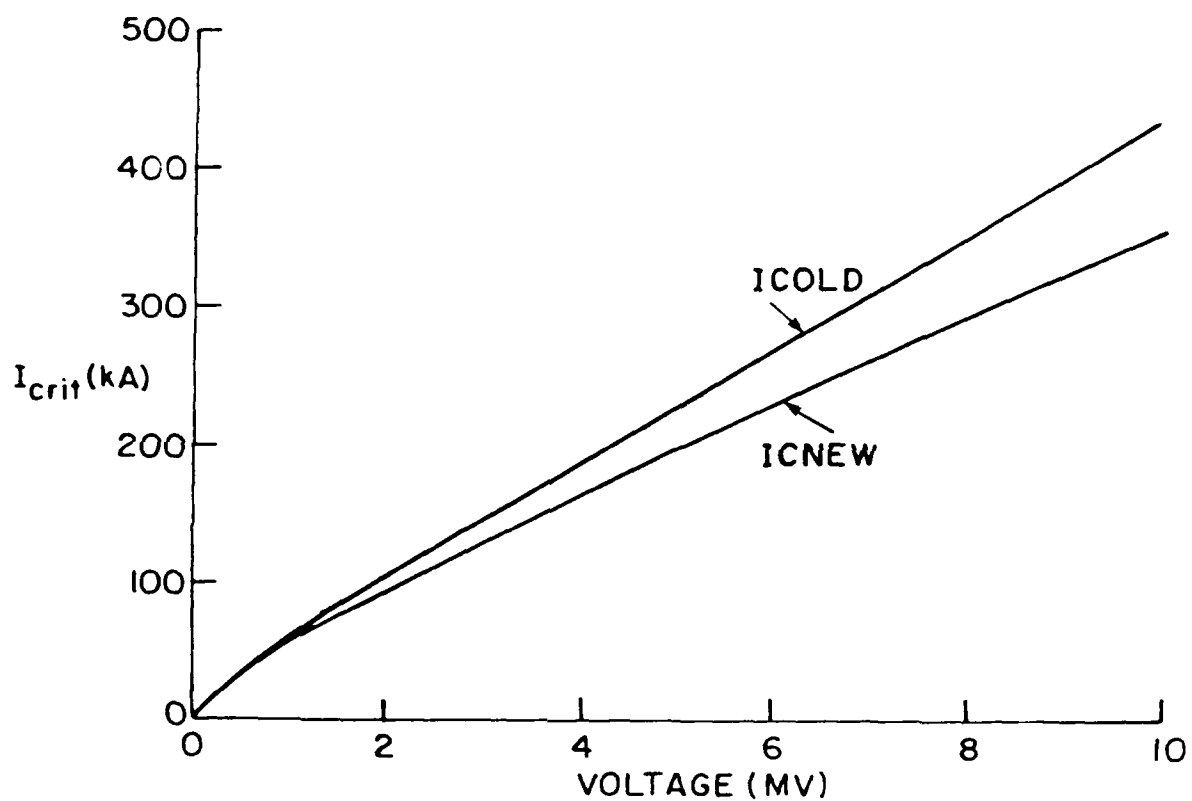


Figure 40. Fit to Computational Data (ICNEW) Compared to NRL's Previous Estimate (ICOLD) of the Magnetic Insulation Threshold.

NRL estimate is seen to be very close to that obtained in this work up to about 3 megavolts. For the entire voltage range, the current required for magnetic insulation is greater in the NRL theory. This may not be bad in practical applications because of $\hat{\theta}$ dependent asymmetries that would degrade the magnetic insulation. To insure insulation, larger values of the critical current would be required. In the next section, equation (165) is used to theoretically model the magnetic insulation and opening of a PEOS.

5.4 Model Gamble II Experiment

In section 5.3, the threshold for the magnetic insulation of a system with a PEOS is given (in figure 39). To verify that this result is consistent with experiment, the insulation curve of figure 39 (equation (165)) is used in conjunction with the transmission line code BERTHA to model a Gamble II PEOS experiment. The experimental and theoretical generator and load currents are compared along with voltages and total power output. Since these quantities are closely tied to the magnetic insulation phenomena, a close match between the theory and experiment will justify equation (165).

The experimental set up is shown in figure 41 [31]. The anode is at a radius of .05 meters. The cathode radius is .025 meters. The PEOS plasma is produced by 3 flashboard plasma sources. The plasma fills a .1 meter long region of the cathode/anode gap. The diode is located .05 meters downstream of the PEOS plasma. The plasma source fires 2

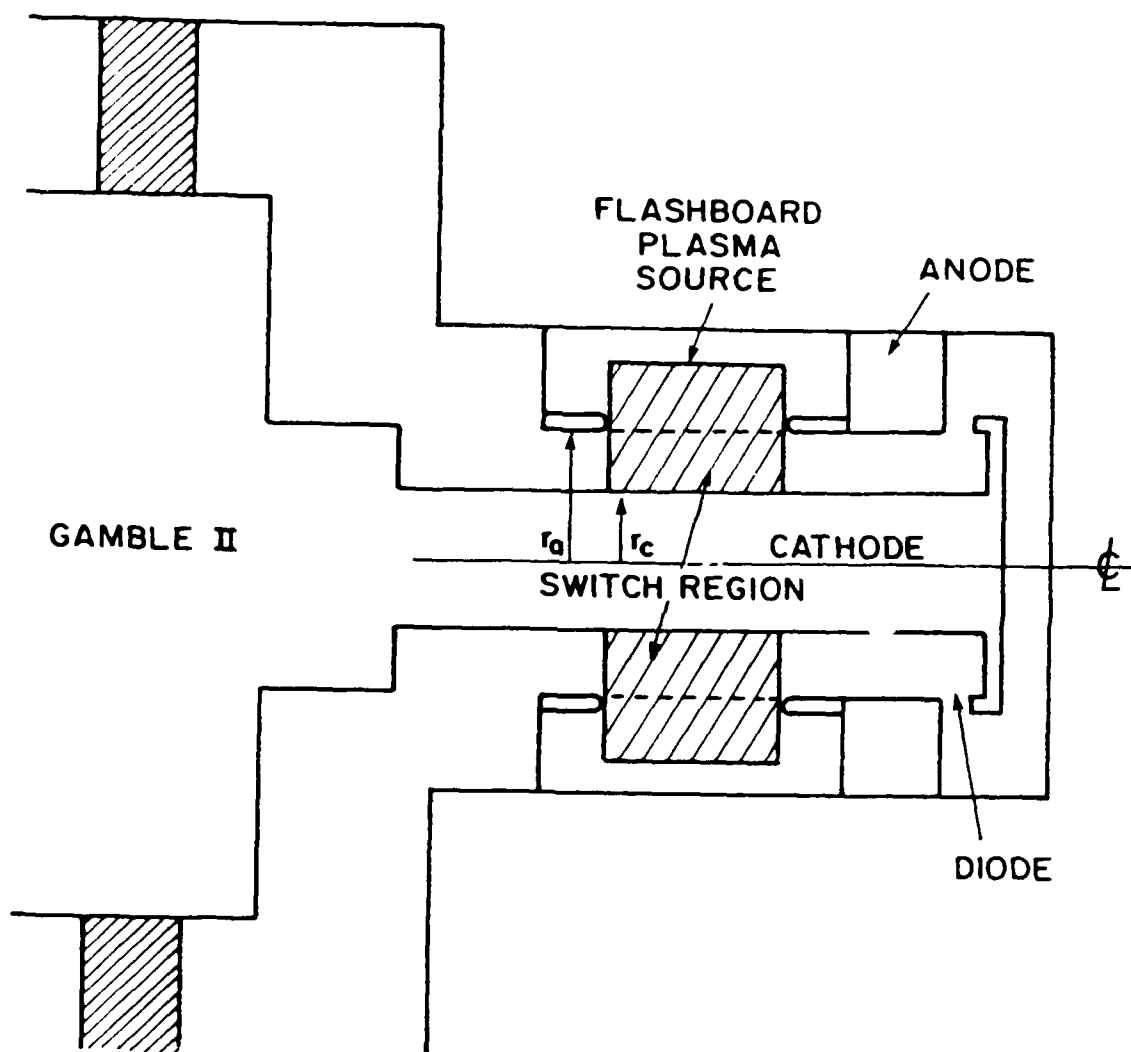


Figure 41. Experimental Setup for PEOS Shot 3426.

microseconds before the Gamble II pulse arrives at the switch. This is to allow for a complete plasma prefill [31]. The data for an opening PEOS (figure 15) corresponding to shot 3426 [31] is compared to the theoretical BERTHA predictions using the new insulation relation (see figure 39). From figure 42, it is clear that the theory is doing a good job of predicting the experimental results. The plasma parameters that give the properties of the injected plasma correspond to those of the experiment. However, it is impossible to measure the quantities precisely. As a result there is latitude for adjusting them to improve the theoretical prediction given in figure 42. The theoretical predictions here are similar to those obtained by Ottinger et. al. in previous studies. This can be understood by examining figure 39 and noting how close the NRL and this works insulation thresholds are in the 0 to 4 megavolt regime — where this experiment was carried out.

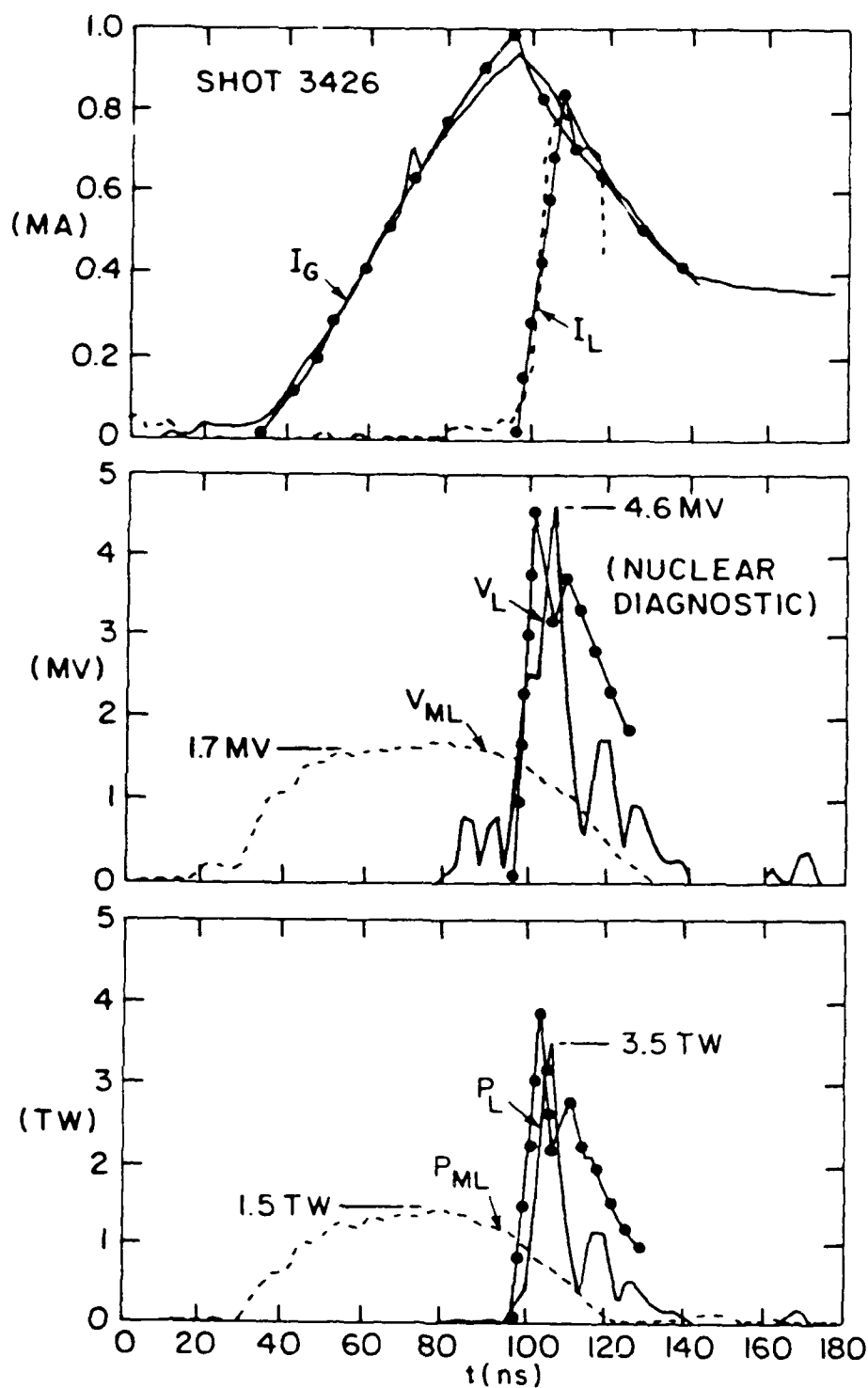


Figure 42. Comparison of Theory (—●—) to Experiment for Shot 3426.

I_G and I_L are the currents out of the generator and through the load. V_L is the voltage across the load. P_L is the power through the load.

CHAPTER 6

CONCLUSIONS

In Chapters 1 and 2 the need for and the basic theory governing magnetic insulation in coaxial cylindrical pulsed power systems are introduced. Some theoretical work previously done in cartesian coordinates is extended to cylindrical coordinates. In comparing the resulting theory to MASK simulations it is found that the cylindrical MITL electron flow is laminar in nature, but has a non-Brillouin flow structure.

This motivates the derivation of a general relativistic laminar MITL flow theory in Chapter 3 of which the Brillouin flow theory is a special case. The new theory is used to perform an independent derivation of the Brillouin flow theory. It is subsequently used to generate self-consistent MITL flow solutions for flows with constant electron density profiles. Such non-Brillouin laminar flows are found to have much in common with several short MITL MASK simulations. In addition, it is found using the general theory that for all laminar flows (Brillouin or not) the relativistic factor for the electrons at the sheath edge is given by: $\gamma_m = I_a/I_c$.

In Chapter 4, the electron flow downstream of abruptly varying structures (some simulating an opening PEOS) is analyzed. It is noted that such structures often launch a beam of magnetically insulated electrons by means of an $\vec{E} \times \vec{B}$

drift. Then the regime in which laminar flows downstream of the PEOS occur is pointed out. A set of equations, obtained via the laminar flow theory of Chapter 3, is presented. These equations give the fields and properties of the launched laminar flow.

In Chapter 5, the magnetic insulation thresholds for coaxial cylindrical MITLs are given for MITLs with and without disruptive structures, and with and without ion emission. One structure of particular interest simulates a PEOS. Variations on this structure lead to the magnetic insulation threshold for a system with a PEOS. The magnetic insulation threshold is checked for the PEOS by using it in a transmission line code to predict results from a Gamble II experiment. The theoretical results compare well with experimental results. This corroborates the computationally determined magnetic insulation threshold for the PEOS.

In short, this work presents a new and general theory governing laminar flows in cylindrical coordinates. This theory includes the Brillouin flow theory as a special case (corresponding to no perturbations); however, the general theory can generate self consistent MITL flow solutions for perturbed systems. This work also sets forth, for the first time, the magnetic insulation thresholds for MITLs with and without obstructions and with and without ion emission. In addition, the magnetic insulation threshold for an opening PEOS is given. These thresholds are given simply in terms of the anode and cathode currents, geometry, load impedance,

vacuum line and structure impedance, as well as the applied voltage.

This research can be expanded and applied to various additional areas. For instance, the techniques used to obtain the general theory of laminar flows in cylindrical coordinates could be used to extend the theory to other coordinate systems. One could also use the general theory to obtain the magnetic insulation threshold for a variety of non-Brillouin flows. The general theory could also be used to generate laminar MITL flows for pulsed power systems with obstructions and impedance mismatches. In addition, the magnetic insulation threshold curves given in Chapter 5 could be used to design a variety of pulsed power systems.

APPENDIX A

ALTERNATIVE CYLINDRICAL TRANSMISSION LINE THEORY DERIVATION

In Appendix A, portions of the cartesian theory of Mendel, as presented in reference [10], are extended to cylindrical coordinates. In this derivation, the function $F(P_{cz}, W)$ needed in equation (39) arises naturally. This alternative derivation of equations (43) and (44) in the text is included in order to add additional insights to the theory.

This derivation differs from that in the text in that no Jacobian of transformation is explicitly performed. Since equations (18)-(21), and (24)-(35) still apply as shown in the text they will not be repeated here. What is needed are the electron density and the current distributions defined in terms of the canonical momentum and total energy.

The electron density with canonical momentum between P_{cz} and $P_{cz} + dP_{cz}$ and energy between W and $W + dW$ at r is (from conservation of charge):

$$\frac{dn(P_{cz}, W)}{dP_{cz} dW} = \frac{2 |j(P_{cz}, W)|}{er\dot{r}} \quad (A1)$$

where $|j(P_{cz}, W)|$ is the one way current density. The factor of 2 comes from realizing that for every charge entering a unit volume from the top there is one also entering from the bottom. \dot{r} is a function of P_{cz} and W and is given by (see equation (25)):

$$\dot{r}^2 = v^2 - \dot{z}^2 = v^2 - (c/\gamma)^2 (P_{cz} + \alpha)^2$$

Substituting in equation (35) and eliminating v^2 with equation (3) gives:

$$\dot{r} = \frac{c}{\gamma} ((W + \phi)^2 - 1 - (P_{cz} + \alpha)^2)^{1/2} \quad (A2)$$

Substituting (A2) into (A1) implies:

$$dn(P_{cz}, W) = \frac{2 |j(P_{cz}, W)| (\phi + W) dP_{cz} dW}{ecr ((\phi + W)^2 - 1 - (P_{cz} + \alpha)^2)^{1/2}} \quad (A3)$$

The current density is (A3) times $\dot{z}(r)$. If one defines $\dot{z}(r)$ in terms of the total energy and canonical momentum (from equation (25)) the current density is given by:

$$dj(P_{cz}, W) = \frac{2(P_{cz} + \alpha) |j(P_{cz}, W)| dP_{cz} dW}{r ((\phi + W)^2 - 1 - (P_{cz} + \alpha)^2)^{1/2}} \quad (A4)$$

Now, from Poisson's equation, equation (A3) and writing everything dimensionlessly gives:

$$\nabla_r^2 \phi = \frac{2e\mu_0}{mc} \iint \frac{|j(P_{cz}, W)| (\phi + W) dP_{cz} dW}{r ((\phi + W)^2 - 1 - (P_{cz} + \alpha)^2)^{1/2}} \quad (A5)$$

From Ampere's law, the restrictions on the electron flow given in section 2.1, equation (A4), and writing the result in dimensionless form gives:

$$\nabla_r^2 \alpha = \frac{2e\mu_0}{mc} \iint \frac{|j(P_{cz}, W)| (P_{cz} + \alpha) dP_{cz} dW}{r ((\phi + W)^2 - 1 - (P_{cz} + \alpha)^2)^{1/2}} \quad (A6)$$

Now, from (A5) and (A6) the electron distribution function is defined to be:

$$F(P_{cz}, W) \equiv \frac{2e\mu_0}{mc} |j(P_{cz}, W)| \quad (A7)$$

One should also note that in equations (A5) and (A6) that the integrals are performed in the canonical momentum and energy phase space. The variable r is independent of this space and can be pulled out of the integrals. So from equations (A5)-(A7) and the definition given in equation (40) one easily obtains:

$$\nabla_r^2 \phi = \frac{1}{r} \frac{\partial G(\phi, \alpha)}{\partial \phi} \quad (A8)$$

$$\nabla_r^2 \alpha = - \frac{1}{r} \frac{\partial G(\phi, \alpha)}{\partial \alpha} \quad (A9)$$

These are the same as equations (41) and (42) which immediately imply equations (43) and (44).

APPENDIX B

RELATION BETWEEN THE DENSITY AND VELOCITY PROFILES

In Appendix B, a simple yet surprising relation is found between the density and velocity profiles for laminar flows. This relation allows one to obtain a complete self-consistent laminar MITL flow solution given only the density profile, or magnetic field profile, or canonical momentum and total energy profile, etc. In other words, a complete flow solution is possible given a very modest amount of information about the flow.

Deriving the relation between the density and velocity profiles begins by integrating equation (43) of the text from the cathode to some r less than or equal to the sheath radius (r_m). The result is:

$$r(\phi'^2 - \alpha'^2) - r_c(\phi_c'^2 - \alpha_c'^2) = 2G - \int_{r_c}^r (\phi'^2 - \alpha'^2) dr \quad (B1)$$

where the subscript c refers to the cathode. This convention will be used in the following. The subscripts a and m will refer to the anode and sheath edge radius respectively. One should also note that $G = 0$ for laminar flows (equation (40)) because:

$$\dot{r} = \frac{c((\phi+W)^2 - 1 - (P_{cz} + \alpha)^2)^{1/2}}{\tau} = 0 \quad (B2)$$

Dimensionalizing (B1) implies:

$$E^2(r) = c^2(B^2(r) - \frac{r_c}{r} B_c^2) + \frac{c^2}{r} \int_{r_c}^r B^2(r_1) - \frac{E^2(r_1)}{c^2} dr_1 \quad (B3)$$

$$\frac{r-r_c}{r} (c^2 B^2(r) - E^2(r))$$

where the bar signifies an average over r . It is necessary to write $B(r)$ and $E(r)$ in the following form using Ampere's and Gauss's laws:

$$B(r) = \frac{\mu_o q_i(r) \overline{v_i(r)}}{2\pi r dz} + \frac{\mu_o I_c}{2\pi r}$$

$$= \frac{\mu_o}{2\pi r} (I_a - I_c) f(r) g(r) + \frac{\mu_o I_c}{2\pi r} \quad (B4)$$

$$E(r) = \frac{q_i(r)}{\epsilon_o 2\pi r dz} = \frac{(I_a - I_c) f(r)}{\epsilon_o 2\pi r \overline{v_d}}$$

$$= \frac{f(r)}{\epsilon_o r} \int_{r_c}^{r_m} \rho(r) r dr \quad (B5)$$

where r_c and r_m are the cathode and sheath radii respectively. $\rho(r)$ is the density profile. I_a and I_c are the anode and cathode currents respectively. $\overline{v_d}$ is the average drift velocity and equals:

$$\overline{v_d} = \frac{I_a - I_c}{\int_{r_c}^{r_m} \rho(r) 2\pi r dr} \quad (B6)$$

$$\frac{q_i(r)}{dz} = \frac{\text{enclosed charge}}{\text{unit length}} = \frac{(I_a - I_c)f(r)}{\bar{v}_d} \quad (B7)$$

$$\begin{aligned} v_i(r) &= \text{average velocity of charge with radius less} \\ &\quad \text{or equal to } r \\ &= \bar{v}_d g(r) \end{aligned} \quad (B8)$$

$$f(r) = \frac{\bar{v}_d}{I_a - I_c} \int_{r_c}^r \rho(r) 2\pi r dr = \frac{\int_{r_c}^r \rho(r) r dr}{\int_{r_c}^{r_m} \rho(r) r dr} \quad (B9)$$

$$g(r) = \frac{1}{I_a - I_c} \frac{\int_{r_c}^r \rho(r) v(r) 2\pi r dr}{f(r)} \quad (B10)$$

Now, substituting (B4) and (B5) into (B3) yields:

$$\begin{aligned} E^2(r) &= c^2(B^2 - \frac{r_c}{r} B_c^2) + \frac{1}{4\pi^2 r (\epsilon_0 c)^2} \left[\right. \\ &\quad \left. \int_{r_c}^r \frac{I_c^2 + 2(I_a - I_c)I_c f g - (c\epsilon_0 2\pi)^2 E^2(r) r^2 f^2 + (I_a - I_c)(f g)^2 dr}{r^2} \right] \end{aligned} \quad (B11)$$

For simplicity in the following analysis, this is evaluated between the cathode (r_c) and the sheath edge radii (r_m). It becomes after algebra (with space charge limited flow):

$$E(r_m) = \frac{c\mu_0}{2\pi r_m} (I_a^2 - I_c^2)^{1/2} \left[\frac{1 + r_m (kC_m + lD_m)}{1 + r_m A_m} \right] \quad (B12)$$

where

$$k \equiv \frac{I_a - I_c}{I_a + I_c} \quad , \quad (B13)$$

$$l \equiv \frac{2I_c}{I_a + I_c} \quad , \quad (B14)$$

$$A_m \equiv \int_{r_c}^{r_m} \frac{f^2(r)}{r^2} dr \quad , \quad (B15)$$

$$D_m \equiv \int_{r_c}^{r_m} \frac{f(r)g(r)}{r^2} dr \quad , \quad (B16)$$

$$C_m \equiv \int_{r_c}^{r_m} \frac{(f(r)g(r))^2}{r^2} dr \quad , \quad (B17)$$

Now for laminar flows, from equation (50) and the fact that P_m of equation (50) equals zero, one obtains an additional relation for the electric field at the sheath edge:

$$E(r_m) = \frac{c\mu_0}{2\pi r_m} (I_a^2 - I_c^2) \quad . \quad (B18)$$

Setting equation (B18) equal to equation (B12) and differentiating with respect to the sheath edge radius (r_m) implies after algebra that:

$$f(r_m) = \frac{l g(r_m)}{1 - kg^2(r_m)} \quad . \quad (B19)$$

From the derivation it would seem this relation is only valid at the sheath edge. Nevertheless, in the following it will be shown to be valid not only at the sheath edge, but at the cathode and across the entire electron sheath. Once this relation is shown to be true across the electron sheath it will be used to relate the density and velocity profiles.

First, it is shown that (B19) holds at the sheath edge. At the sheath edge (r_m), $f(r_m) = 1 = g(r_m)$ from equations (B9) and (B10). Substituting $g(r_m) = 1$ into equation (B19) yields:

$$f(r_m) = \frac{2I_c}{I_a - I_c} \frac{1}{\left[1 - \left[\frac{I_a - I_c}{I_a + I_c}\right]\right]} = 1 \quad .$$

as expected.

At $r = r_c$, $g(r_c) = 0$. Substituting $g(r_c) = 0$ into equation (B19) yields $f(r_c) = 0$. At r_c , $f(r_c)$ does indeed equal zero as can be seen in equation (B9).

Now it is necessary to show that for laminar flows (B19) is true in the region $r_c < r < r_m$. For laminar flows:

$$\vec{E} = -\vec{v} \times \vec{B} = -v(r)B(r) \hat{r} \quad . \quad (B20)$$

Substituting (B4) and (B5) into (B20) implies:

$$f(r) = \frac{I_c v(r) \overline{v_d}}{(I_a - I_c) c^2 \left[1 - \frac{v(r)g(r) \overline{v_d}}{c^2}\right]} \quad . \quad (B21)$$

where $\overline{v_d}$ is given in this case by equation (52). The velocity $v(r)$ can be obtained from equation (B10) assuming (B19) is true across the flow:

$$f(r) = \frac{1}{1 - kg^2(r)} \frac{g(r)}{g(r)} \quad . \quad (B22)$$

Now (B22) allows one to write

$$g(r) = -\frac{1}{2f(r)k} + \left[\left[\frac{1}{2f(r)k} \right]^2 + \frac{1}{k} \right]^{1/2} \quad (B23)$$

The derivative of (B10) gives:

$$v(r) = \frac{(g'(r)f(r) + g(r)f'(r))(I_a - I_c)}{2\pi r \rho(r)} \quad (B24)$$

where

$$f'(r) = \frac{\rho(r) r}{\int_{r_c}^{r_m} \rho(r) r dr}$$

$$g'(r) = \frac{1}{2kf^2(r)} \left[1 - \frac{1}{2kf(r) \left(\left(\frac{1}{2f(r)k} \right)^2 + \frac{1}{k} \right)} \right]$$

Therefore,

$$v(r) = \frac{I_c}{2\pi \int_{r_c}^r \rho(r) r dr} \left[\left[1 + \frac{(I_a^2 - I_c^2)f^2(r)}{I_c^2} \right]^{1/2} - \left[1 + \frac{(I_a^2 - I_c^2)f^2(r)}{I_c^2} \right]^{-1/2} \right] \quad (B25)$$

Now for laminar flows, equation (B21) must be satisfied. If it is satisfied by the $g(r)$ and $v(r)$ obtained from assuming (B22) valid across the flow, then the assumption of (B22) is justified. So, substituting (B23), (B25), and (52) into (B21) yields:

$$f(r) = \frac{I_c^2}{(I_a^2 - I_c^2)f(r)} \left[\left[1 + \left[\frac{I_a^2 - I_c^2}{I_c^2} \right] f^2(r) \right]^{1/2} - \left[1 + \left[\frac{I_a^2 - I_c^2}{I_c^2} \right] f^2(r) \right]^{-1/2} \right] \\ \frac{\left[1 - \frac{I_c}{f(r)(I_a + I_c)} \left[\left[\left[\frac{1}{2f(r)k} \right]^2 + \frac{1}{k} \right]^{1/2} - \frac{1}{2f(r)k} \right] \times \right.}{\left. \left[\left[1 + \left[\frac{I_a^2 - I_c^2}{I_c^2} \right] f^2(r) \right]^{1/2} - \left[1 + \left[\frac{I_a^2 - I_c^2}{I_c^2} \right] f^2(r) \right]^{-1/2} \right]} \right] \quad (B26)$$

Given an anode and cathode current, and $f(r)$ on the right hand side (RHS) of (B26), the calculated $f(r)$ on the left hand side (LHS) of the equation must equal the $f(r)$ substituted into the right if (B22) is to be justified. This is done for three different currents and two different $f(r)$ s in Table B1. Equation (B26) not only holds for the cases given in Table B1, it holds in general. This justifies equation (B22) across the flow. Therefore,

$$f(r) = \frac{1}{1 - kg^2(r)} \frac{g(r)}{g(r)} \quad , \quad r_c \leq r \leq r_m \quad (B27)$$

Equation (B27) is used in the text to determine a velocity profile given a density profile.

$f(r)$ RHS	I_a	I_c	$g(r)$	Num.	Den.	$f(r)$ LHS
.5	I_a	$.9I_a$.5202592	.4859543	.9719087	.5
.5	I_a	$.5I_a$.6457513	.3779645	.755929	.5
.25	I_a	$.3I_a$.4756728	.1956984	.7827937	.25

Table B1. Verification of equation (B26). This is done for three different anode/cathode current ratios and two different $f(r)$ values.

APPENDIX C

MAGNETIC INSULATION THRESHOLD DATA

Tables C1 thru C9 comprise a record of pertinent magnetic insulation data for 100 MASK simulations. The simulations were run for coaxial cylindrical MITL geometries, with and without structures, and with and without ion emission off the structures. The ion emitting structures were used to duplicate PEOSs in different stages of opening. Diagrams of the two fundamental computational meshes used in this study are given in figures 3a and 3b. The mesh parameters in 3a and 3b are varied to obtain an understanding of the relation between the applied voltage, geometry and magnetic insulation. Tables C1-C3 correspond to figure 3a and Tables C4-C9 correspond to figure 3b. The data from these tables is used to generate the magnetic insulation threshold curves for figures 35 and 37 in Chapter 5.

Simulation	V_a	d_g	I_a	I_c	$\frac{z_1}{z_0}$
M407-M412	2×10^6	.01	-1.56×10^5	-1.5×10^5	.31
M414	"	.015	-9.6×10^4	-8.1×10^4	.5
M416	"	.032	-7.92×10^4	-4.72×10^4	.61
M417, M419	"	.023	-7.872×10^4	-4.27×10^4	.61
M418, M420	"	.018	-8.46×10^4	-6.5×10^4	.568
M421	"	.016	-9.3×10^3	—	.52
M423	"	.011	-1.324×10^5	—	.363
M424	"	.02	-7.97×10^4	—	.603
M426	$.5 \times 10^6$.015	-2.753×10^4	-1.79×10^4	.437
M427	"	.011	-2.784×10^4	-1.87×10^4	.431
M435	1×10^6	.016	-4.65×10^4	-2.672×10^4	.517
M436	"	.018	-4.613×10^4	-2.463×10^4	.521
M437	"	.014	-4.846×10^4	-2.707×10^4	.496
M438	"	.012	-5.169×10^4	—	.465
M440	3×10^6	.022	-1.118×10^5	-4.446×10^4	.645
M441	"	.024	-1.095×10^5	-4.188×10^4	.659
M442	"	.020	-1.154×10^5	-7.901×10^3	.625
M443	"	.028	-1.093×10^5	-4.163×10^4	.660

Table C1 Simulation data for the determination of the magnetic insulation threshold ($r_a = .05$, $r_c = .025$). This study was done without ion emission off the anode.

Simulation	V_a	d_g	I_a	I_c	$\frac{z_1}{z_0}$
M450	2×10^6	.056	-2.509×10^4	-1.203×10^4	.577
M451	"	.030	-2.481×10^4	-1.136×10^4	.5835
M452	"	.012	-2.623×10^4	-2.1×10^4	.552
M453	"	.020	-2.44×10^4	-1.11×10^4	.593
M456	"	.018	-2.45×10^4	—	.591
M457	1×10^6	.022	-1.44×10^4	-1.44×10^4	.501
M458	"	.006	-1.77×10^4	-1.77×10^4	.408
M459	"	.016	-1.43×10^4	-1.43×10^4	.505

Table C2. Simulation data for the determination of the magnetic insulation threshold ($r_a = .05$, $r_c = .005$). This study is without ion emission off the anode.

Simulation	V_a	d_g	I_a	I_c	$\frac{z_1}{z_0}$
MN01	2×10^6	.01	-1.779×10^5	-1.365×10^5	.557
MN04	"	.018	-1.646×10^5	-7.37×10^4	.602
MN05	"	.014	-1.642×10^5	-7.305×10^4	.6033
MI30	2×10^6	.014	-1.804×10^5	—	.549
MI31	"	.024	-1.737×10^5	—	.5703
MI33	"	.018	-1.798×10^5	—	.551
MI35	3×10^6	.024	-2.518×10^5	—	.59
MI36	"	.018	-2.491×10^5	—	.5965
MI38	"	.014	-2.674×10^5	—	.55

Table C3. Simulation data for the determination of the magnetic insulation threshold ($r_a = .035$, $r_c = .025$). The "MN" calculations were done without ion emission and the "MI" simulations were done with ion emission off the anode.

Simulation	V_a	d_g	I_a	$\frac{z_l}{z_p}$	Flow
PN05	2×10^6	.0075	-1.834×10^5	.54	vortex
PN04	"	.008	-1.898×10^5	.52	vortex
PN06	"	.009	-1.509×10^5	.656	laminar
PN07	"	.012	-1.473×10^5	.672	laminar
PN08	"	.015	-1.469×10^5	.674	laminar
PN09	"	.0105	-1.488×10^5	.666	laminar
PN10	3×10^6	.0105	-2.025×10^5	.734	laminar
PN11	"	.012	-2.023×10^5	.735	laminar
PN12	"	.0075	-2.63×10^5	.565	vortex
PN13	"	.021	-2.093×10^5	.71	laminar
PN14	4×10^6	.012	-2.569×10^5	.7713	laminar
PN15	"	.0195	-2.633×10^5	.7525	laminar
PN16	"	.009	-2.858×10^5	.6933	vortex

Table C4. Simulation data for the determination of the magnetic insulation threshold for systems with a non-ion emitting structure($r_c = .025$, $r_a = .05$, $r_p = .035$, $D = .192$, $D_p = .06$, $\Delta z = .03$).

Simulation	V_a	d_g	I_a	$\frac{z_1}{z_p}$	flow
PN12	4×10^6	.0075	-3.615×10^5	.548	vortex
PN18	"	.012	-2.573×10^5	.7701	laminar
PN19	"	.0195	-2.639×10^5	.7501	"
PN21	3×10^6	.009	-2.074×10^5	.717	laminar
PN22	"	.0105	-2.023×10^5	.735	"
PN23	"	.0135	-2.06×10^5	.7214	"
PN24	2×10^6	.0105	-1.476×10^5	.671	laminar
PN25	"	.009	-1.491×10^5	.665	"
PN26	"	.0075	-1.829×10^5	.542	vortex
PN27	6×10^6	.0106	-3.56×10^5	.835	laminar
PN28	"	.015	-3.623×10^5	.82	"
PN29	"	.0225	-3.774×10^5	.788	"

Table C5. Simulation data for the determination of the magnetic insulation threshold for systems with a non-ion emitting structure ($r_c = .025$, $r_a = .05$, $r_p = .035$, $D_p = .105$, $D = .192$, $\Delta z = .03$).

Simulation	V_a	d_g	I_a	$\frac{z_l}{z_p}$	Flow
P001	2×10^6	.01	-1.533×10^5	.463	vortex
M482	"	.016	-1.067×10^5	.665	laminar
M483	"	.02	-1.071×10^5	.662	"
Where $r_p = .04$, $D_p = .07$, $D = .256$, $\Delta z = .05$.					
PN31	4×10^6	.018	-1.83×10^5	.7751	laminar
PN32	"	.012	-2.492×10^5	.569	vortex
PN33	"	.024	-1.846×10^5	.768	laminar
Where $r_p = .04$, $D_p = .06$, $D = .192$, $\Delta z = .03$.					
PN35	4×10^6	.018	-1.753×10^5	.647	vortex
PN36	"	.012	-2.525×10^5	.449	vortex
PN37	"	.024	-1.469×10^5	.772	laminar
PN38	"	.030	-1.48×10^5	.766	"
Where $r_p = .045$, $D_p = .06$, $D = .192$, $\Delta z = .03$.					

Table C6. Simulation data for the determination of the magnetic insulation threshold for systems with a non-ion emitting structure ($r_c = .025$, $r_a = .05$).

Simulation	V_a	d_g	I_a	$\frac{z_l}{z_p}$	Flow
PI03	2×10^6	.0075	-1.868×10^5	.53	laminar
PI04	"	.009	-1.844×10^5	.5372	"
PI05	"	.0105	-1.84×10^5	.538	"
PI06	"	.0135	-1.72×10^5	.575	"
PI08	3×10^6	.0075	-2.664×10^5	.558	laminar
PI09	"	.009	-2.53×10^5	.587	"
PI10	"	.0105	-2.503×10^5	.594	"
PI13	4×10^6	.0075	-3.492×10^5	.567	vortex
PI14	"	.009	-3.222×10^5	.615	laminar
PI15	"	.0105	-3.165×10^5	.626	"
PI16	"	.012	-3.148×10^5	.629	"

Table C7. Magnetic insulation threshold data for an ion emitting PEOS like structure ($r_c = .025$, $r_a = .05$, $r_p = .035$, $D_p = .06$, $D = .192$, and $\Delta z = .03$).

Simulation	V_a	d_g	I_a	$\frac{z_l}{z_p}$	Flow
PI17	3×10^6	.0075	-2.567×10^5	.58	laminar
PI18	"	.009	-2.498×10^5	.595	"
PI19	"	.0105	-2.491×10^5	.5966	"
PI21	4×10^6	.009	-3.165×10^5	.626	laminar
PI22	"	.012	-3.151×10^5	.629	"
PI23	"	.0135	-3.13×10^5	.633	"
PI26	6×10^6	.012	-4.376×10^5	.679	laminar
PI27	"	.009	-4.454×10^5	.667	"

Table C8. Magnetic insulation threshold data for an ion emitting PEOS like structure ($r_c = .025$, $r_a = .05$, $r_p = .035$, $D_p = .09$, $D = .192$, and $\Delta z = .03$).

Simulation	V_a	d_g	I_a	$\frac{z_l}{z_p}$	flow
PI29	4×10^6	.021	-2.247×10^5	.631	laminar
PI30	"	.015	-2.244×10^5	.632	"
PI31	"	.012	-2.244×10^5	.632	"
PI34	6×10^6	.012	-3.145×10^5	.677	laminar
PI36	"	.027	-3.128×10^5	.68	"

Table C9. Magnetic insulation threshold data for an ion emitting PEOS like structure ($r_c = .025$, $r_a = .05$, $r_p = .035$, $D_p = .09$, $D = .192$, $\Delta z = .03$, $r_p = .04$).

REFERENCES

1. M.S. Di Capua, "Magnetic Insulation", IEEE Transactions on Plasma Science 11(3), 205(1983).
2. C.W. Mendel, Jr., D.B. Seidel, and S. A. Slutz, "A General Theory of Magnetically Insulated Electron Flow", Phys. Fluids 26(12), 3628(1983).
3. J.M. Creedon, "Magnetic Cutoff in High-Current Diodes", Journal of Applied Physics 48(3), 1070(1977).
4. G. Cooperstein, et. al., Proc. Fifth Int Conf. of High-Power Part. Beams (San Francisco, Ca), B3(1983).
5. A.W. Hull, Phys. Rev. 18, 31(1921).
6. R.V. Lovelace and E. Ott, "Theory of Magnetic Insulation", Phys. of Fluids 17(6), 1263(1974).
7. A. Ron, A. A. Mondelli, and N. Rostoker, "Equilibria for Magnetic Insulation", IEEE Trans. Plasma Science, PS-1, 85(1973).
8. J. M. Creedon, "Relativistic Brillouin flow in the High v/γ Diode", Journal of Applied Phys 46(7), 2946(1975).
9. M. Y. Wang, "Generalize Relativistic Brillouin Theory", Appl. Phys. Lett., 33(4), 284(1978).
10. C. W. Mendel, Jr., "Planar One-Dimensional Magnetically Insulated Electron Flow for Arbitrary Canonical Momentum Distribution", Journal Appl. Phys. 50(6), 3830(1979).
11. M. P. Desjarlais and R. N. Sudan, "Electron Diffusion and Leakage Currents in Magnetically Insulated Diodes",

- Phys. Fluids 30(5), 1536(1987).
12. P. A. Miller and C. W. Mendel, Jr., "Analytic Model of Applied-B Ion Diode Impedance Behaviour", J. Appl. Phys. 61(2), 529(1987).
 13. R. C. Davidson, "Kinetic Stability Theorem for Relativistic Non-Neutral Electron Flow in a Planar Diode with Applied Magnetic Field", Phys. Fluids 28(1), 377(1985).
 14. C.W. Mendel, Jr., D. B. Seidel, and S. E. Rosenthal, "A Simple Theory of Magnetic Insulation from Basic Physical Considerations", Laser and Particle Beams 1(3), 311(1983).
 15. M.P. Desjarlais and R. N. Sudan, " A Thermal Distribution Function for Relativistic Magnetically Insulated Electron Flows", Phys. Fluids 29(5), 1746(1986).
 16. J. P. Van Devender, "Long Self-Magnetically Insulated Power Transport Experiments", J. Appl. Phys. 50(6), 3923(1979).
 17. J. P. Van Devender, J. P. Quintenz, R J. Leeper, D. J. Johnson, and J. T. Crow, "Self-Magnetically Insulated Ion Diode", J. Appl. Phys. 52(1), 4(1981).
 18. R. Kraft and M. W. McGeoch, "Experimental Study of Magnetic Insulation", Phys. Fluids 30(4), 1189(1987).
 19. E. I. Baranchikov, A. V. Gordeev, V. D. Korolev, and V. P. Smirnov, "Magnetic Self-Insulation of Electron Beams in Vacuum Lines", Sov. Phys. JETP 48(6),

1058(1978).

20. S. Shope, J. W. Poukey, K. D. Bergeron, D. H. M^cDaniel, A. J. Toepfer, and J. P. Van Devender, "Self-Magnetic Insulation in Vacuum for Coaxial Geometry", J. Appl. Phys. 49(7), 3675(1978).
21. S. Humphries, Jr., R. N. Sudan, and L. Wiley, "Extraction and Focusing of Intense Ion Beams from a Magnetically Insulated Diode", J. Appl. Phys. 47(6), 2382(1976).
22. Y. Maron, "Local Electron Flow to the Anode in Magnetically Insulated Diode", Phys. Fluids 27(1), 285(1984).
23. I. D. Smith, P. Champney, and J. M. Creedon, "Magnetic Insulation", Proceedings International Pulsed Power Conference, Lubbock, Texas, IIc8-1(1976).
24. K. D. Bergeron and J. W. Poukey, "Relativistic Space - Charge Flow in a Magnetic Field", Applied Physics Letters 27(2), 58(1975).
25. J. A. Swegle, "Nonexistence of Quasilaminar Equilibria in Cylindrical Magnetically Insulated Lines", Phys. Fluids 25(7), 1282(1982).
26. E. N. Abdullin, et. al., "High Current Plasma Filled Diode as Current Breaker", Sov. J. Plasma Phys. 11, 66(1985).
27. B. V. Weber, et. al. "Plasma Erosion Opening Switch Research and Applications", Proc. Sixth Int. Conf. on High Power Particle Beams, Kobe, Japan, 851(1986).

28. A. T. Drobot, Bull. Am. Phys. Soc. 29, 1379(1984).
29. D. D. Hinshelwood, "BERTHA — A Versatile Transmission Line and Circuit Code", NRL Memorandum Report 5185, Nov 1983.
30. C. K. Birdsall and A. B. Langdon, Plasma Physics Via Computer Simulations, M^cGraw Hill, Inc., 355(1985).
31. J. M. Neri, J. R. Boller, P. F. Ottinger, B. V. Weber and F. C. Young, "High Voltage, High Power Operation of the Plasma Erosion Opening Switch", NRL Memorandum Report 5948, April, 1987.
32. C. W. Mendel, Jr., J. A. Swegle, and D. B. Seidel, "Stability of Magnetically Insulated Electron Flow", Phys. Rev. A 32(2), 1091(1985).
33. M. Y. Wang and M. S. Di Capua, "Operating Point of Long Magnetically Insulated Vacuum Transmission Lines", J. Appl. Phys. 51(11), 5610(1980).
34. B. V. Weber, Naval Research Lab., Washington, D.C., Private Communications (1987).
35. S. Miyamoto, N. Yugami, H. Fujita, T. Ozaki, K. Imasaki, S. Nakai, and C. Yamanaka, "Performance of Plasma Erosion Opening Switches in High Voltage Pulsed Power Compression," Jpn. J. Appl. Phys. 25, 1108(1986).
36. H. Bluhm, K. Bohnel, R. Genuario, P. Hoppe, H. U. Karow, W. Ratjczak, and D. Rusch, "Plasma Opening Switch Experiments at the Pulsed Power Generators Pollux and Kalif, "Proc. Sixth Int. Conf. on High Power Particle Beams", Kobe, Japan, 855(1986).

37. C. W. Mendel, Jr., and Steven A Goldstein, "A Fast-opening Switch for Use in REB Diode Experiments", J. Appl. Phys. 48, 1004(1977).
38. R. Stringfield, R. Schneider, R. D. Genuario, I. Roth, K. Childers, C. Stalling and D. Dakin, "Plasma Erosion Switches with Imploding Plasma Loads on Multiterawatt Pulsed Power Generators", J. Appl. Phys. 52, 1278(1981).
39. R. A. Meger and F. C. Young, "Pinched-Beam Ion-Diode Scaling on the Aurora Pulser", J. Appl. Phys. 53, 8543(1982).
40. R. A. Meger, R. J. Comisso, G. Cooperstein and Shyke A. Goldstein, "Vacuum Inductive Store/Pulse Compression Experiments on a High Power Accelerator Using Plasma Opening Switches", Appl. Phys. Lett 42, 943(1983).
41. R.W. Stinnett, et. al., "Plasma Opening Switch Performance on Supermite and PBFAII", IEEE Int. Conf. on Plasma Science, Saskatoon, 24(1986).
42. B. V. Weber, et. al., "Plasma Erosion Opening Switch Research and Applications", Proc. Sixth Int. Conf. on High Power Particle Beams, Kobe, Japan, 851(1986).
43. D. D. Hinshelwood, et. al., "Long Conduction Time Plasma Erosion Opening Switch Experiments", Appl. Phys Lett. 49, 1635(1986).
44. S. J. Stephanakis, et. al., "Effect of Pulse Compression on Ion Beams from Pinch Reflex Diodes", Bull. APS 28, 1055(1983).

45. D. D. Hinshelwood, et. al., "Repetitively Pulsed Operation of the Plasma Erosion Opening Switch", IEEE Int. Conf. on Plasmas Science, Arlington, Va., 50(1987).
46. B.V. Weber, et. al., "Plasma Erosion Opening Switch Research at NRL", (1987 to be published).
47. R. Mason, J. M. Wallace, K. Lee, "Implicit Two-Fluid Simulation of Electron Transport in a Plasma Erosion Opening Switch", Proc. 2nd Int. Topical Symp. on ICF by High-Power Particle Beams, Nagaoka, Japan, 320(1986).
48. J. M. Grossman, P. F. Ottinger, J. M. Neri, and A. T. Drobot, Phys. Fluids 29, 2724(1986).
49. E. M. Waisman, P. G. Steen, D. E. Parks, and A. Wilson, Appl. Phys. Lett. 46, 1045(1985).
50. D. Mosher, P. F. Ottinger and J. M. Grossman, Bull. Am. Phys. Soc. 30, 1447(1985).
51. B. V. Weber, R. J. Comisso, R. A. Meger, J. M. Neri, W. F. Oliphant and P. F. Ottinger, "Current Distribution in a Plasma Erosion Opening Switch", Appl. Phys. Lett. 45, 1043(1984).
52. J. M. Grossman, et. al., Bull. APS 31, 1444(1986).
53. S. S. Payne, T. W. Hussey, R. W. Stinnett and N. F. Roderick, Bull. Am. Phys. Soc. 31, 1399(1986).
54. R. J. Mason, IEEE Int Conf. on Plasma Science, Arlington, Va., 51(1987).
55. R. Kulsrud, P. F. Ottinger and J. M. Grossman, "Analysis of Anomalous Resistivity During the Conduction Phase of

the Plasma Erosion Opening Switch", Naval Research Laboratory, to be published.

56. P. F. Ottinger, S. A. Goldstein, and R. A. Meger, "Theoretical Modeling of the Plasma Erosion Opening Switch for Inductive Storage Applications", J. Appl. Phys. 56(3), 774(1984).
57. Shyke A. Goldstein and R. Lee, "Ion-Induced Pinch and the Enhancement of Ion Current by Pinched Electron Flow in Relativistic Diodes", Phys. Rev. Lett. 35, 1079(1975).
58. R. J. Barker and Shyke A. Goldstein, "Computational Studies of a Radial Pinch-Reflex Diode", Bull. Am. Phys. Soc. 26, 921(1981).
59. John Swegle and Edward Ott, "Instability of the Brillouin-Flow Equilibrium in Magnetically Insulated Structures", Phys. Rev. Letts., 46(14), 929(1981).
60. John Swegle and Edward Ott, "Linear Waves and Instabilities on Magnetically Insulated Gaps", Phys. Fluids 24(10), 1821(1981).
61. John Swegle, "Stability of Relativistic Laminar Flow Equilibria for Electrons Drifting in Crossed Fields", Phys. Fluids 26(6), 1670(1983).
62. C. L. Chang, I. M. Antonsen, Jr., E. Ott, and A. T. Drobot, "Instabilities in Magnetically Insulated Gaps With Resistive Electrode Plasmas", Phys. Fluids 27(10), 2545(1984).
63. M. P. Desjarlais and R. N. Sudan, "Stochastic Electron

Motion in Magnetically Insulated Diodes", Phys. Fluids
29(4), 1245(1986).

64. J. Neri, Naval Research Laboratory, Washington, D.C.,
Private Communications (1987).